Mechanics of Materials 189 (2024) 104891

Contents lists available at ScienceDirect

Mechanics of Materials

journal homepage: www.elsevier.com/locate/mecmat

Research paper

Modeling strain-induced martensitic transformation in austenitic stainless steels subjected to cryogenic temperatures using incremental mean-field homogenization schemes

P. Fernández-Pisón [a,b,*], A.R. Vishnu [a], G. Vadillo [a], J.A. Rodríguez-Martínez [a]

[a] Department of Continuum Mechanics and Structural Analysis, University Carlos III of Madrid, 28911 Leganés, Madrid, Spain
[b] EN Department, CERN, 1211 Genève, Switzerland

ARTICLE INFO

Keywords:
Homogenization
Multiscale modeling
Phase transformation
Cryogenic temperatures
Finite element analysis

ABSTRACT

Austenitic stainless steels are commonly used as structural materials in high-field superconducting magnet systems because they retain high strength, ductility, and toughness at very low temperatures, and they are paramagnetic or antiferromagnetic under the Néel temperature in their fully austenitic state. However, they are susceptible to strain-induced martensitic transformation, especially at cryogenic temperatures, which modifies the material properties, induces volume changes and additional strain hardening, and leads to ferromagnetic behavior. Thus, accurate predictions of the structural performance of these materials at very low temperatures are of great interest for the conception and design of these cryo-magnetic systems. In this paper, we propose an adequate constitutive model for the evolving bi-phase material—austenite and martensite—based on a Hill-type incremental formulation. Two different versions of the model are proposed based on the linear mean-field homogenization scheme: Mori-Tanaka and Self-Consistent. Moreover, a rate-independent nonlinear mixed kinematic-isotropic hardening law is used for each phase, and the martensitic transformation is described by the nonlinear kinetic law proposed by Olson and Cohen (1975). The constitutive model is implemented in ABAQUS/Standard through a UMAT user subroutine, for which a return mapping algorithm based on the implicit backward Euler integration scheme is used and a closed-form expression of the consistent Jacobian tensor is provided. The Mori-Tanaka and Self-Consistent approaches are evaluated in terms of their ability to describe the mechanical behavior of the bi-phase aggregate by comparing the predictions of the homogenization schemes with unit-cell finite element calculations with an explicit description of the martensite inclusions and the austenite matrix. The comparison is carried out for different stress states with controlled triaxiality and Lode parameter under monotonic and cycling loading, paying special attention to the evolution of the mechanical fields in each phase. The unit-cell calculations are performed for both constant and evolving martensite volume fractions. In addition, numerical simulations of tensile tests on samples subjected to different initial temperatures are carried out for the transforming bi-phase material and the results are compared to experimental data for AISI 304L and AISI 316LN steels.

1. Introduction

Due to the high strength, ductility, and toughness that austenitic stainless steels exhibit at low temperatures, they are the predominant structural material used for cryogenic applications. Since they are paramagnetic or antiferromagnetic under the Néel temperature in their fully austenitic state, high-field superconducting magnet systems are one of their main application fields of interest (Sgobba, 2006; Barabash et al., 2007). The austenitic steel collars of the standard Dipole magnet for the LHC at CERN, as well as those for the LHC's more recent upgrade (the High Luminosity LHC), and the jacket of the ITER Cable-in-Conduit Conductors, are some examples of structural components made of austenitic stainless steel (Bertinelli et al., 2006; Bordini et al., 2019; Devred et al., 2014).

Nevertheless, austenitic stainless steels are particularly prone to strain-induced martensitic transformation at cryogenic temperatures (Angel, 1954). The initially undeformed γ-austenite (face-centered cubic) may be transformed into either ϵ-martensite (hexagonal close-packed) or α'-martensite (body-centered tetragonal) when submitted

* Corresponding author now at: Mines Paris, PSL Research University, Centre des Matériaux, CNRS UMR 7633, Paris, France.
E-mail address: pilar.fernandez@minesparis.psl.eu (P. Fernández-Pisón).

https://doi.org/10.1016/j.mechmat.2023.104891
Received 30 June 2023; Received in revised form 4 December 2023; Accepted 7 December 2023
Available online 9 December 2023

to plastic deformation. However, since the α'-martensitic transformation is generally much more extensive than the transformation of ϵ-martensite (Mangonon and Thomas, 1970; Seetharaman, 1984; De et al., 2004), the partially transformed material can be reasonably considered bi-phasic: α'-martensite sites dispersed in the γ-austenite matrix. The γ-α' transformation may lead to a considerable evolution of material properties (e.g., strong hardening) and to ferromagnetic behavior of the bi-phase material, which is problematic for the above-mentioned application (i.e., for superconducting magnet systems). Moreover, the transformation rate increases with decreasing temperature, so a nearly fully or fully transformed α'-martensitic material may be obtained at low temperatures and high levels of deformation (Fernández-Pisón et al., 2021). For these reasons, it is necessary to formulate a specific constitutive model for cryogenic applications that covers the entire transformation range and resolves the inherent complexity of the evolving microstructure of austenitic steels.

There are only a few elastoplastic constitutive models in the open literature that have been expressly developed to describe the mechanical behavior of austenitic steels at cryogenic temperatures. The majority of these works simply modify the explicit functions of common plasticity models so they can adequately predict macroscopically the additional strain hardening produced by the martensitic transformation at cryogenic temperatures, as in Lee et al. (2009), Ding et al. (2019) and Homayounfard and Ganjiani (2022). More detailed approaches considering the evolving microstructure using homogenization techniques for bi-phase materials are the Mori-Tanaka-based model proposed by Garion and Skoczeń (2002) and the Voigt-like formulation used by Kothari et al. (2019). The model proposed by Garion and Skoczeń (2002) is widely used in the literature, as demonstrated by Sitko et al. (2010), Ortwein et al. (2014), Kazemi et al. (2019) and Schmidt et al. (2022), among others (some of these works additionally include specific features to account for microdamage and/or discontinuous plastic flow).

The original model proposed by Garion and Skoczeń (2002) was developed at CERN for the LHC thin-walled corrugated shells (called bellows) made of AISI 316L. Since these bellows undergo cycles of expansion and compression at cryogenic temperatures, a distinctive feature of this constitutive framework was to include a mixed kinematic-isotropic hardening for the bi-phase material valid at low temperatures. The authors considered the austenite as elasto-plastic and the martensite as elastic, and they accounted for two contributions to the strain hardening of the bi-phase material: the strain hardening of the austenite phase and the evolution of the composite's tangent stiffness. The austenite was assumed to have a linear kinematic hardening, with the hardening coefficient increasing linearly with the martensite volume fraction. The bi-phase material's tangent stiffness tensor was computed via mean-field homogenization using a Hill-type incremental approach (Hill, 1965a) and the Mori-Tanaka scheme (Mori and Tanaka, 1973; Benveniste, 1987). A new formulation was employed to reduce all anisotropic tangent stiffness operators to isotropic forms. The main simplifying assumptions of the model of Garion and Skoczeń (2002) were to consider that the strain increment of the bi-phase material was the same as that of the austenite matrix and that this strain increment was only due to the plastic strains. Moreover, the model introduced a simplified (but non-differentiable) kinetic law of martensitic transformation based on a linearization of the law proposed by Olson and Cohen (1975). The constitutive framework of Garion and Skoczeń (2002) is attractive because of its simplicity, but convergence between the experimental results and model predictions is limited to strain values not exceeding 0.2.

In this paper, we take the formulation of Garion and Skoczeń (2002) as the starting point to develop an improved constitutive model that is suitable for predicting the mechanical behavior of austenitic stainless steels at large strains and cryogenic temperatures for any volume fraction of transformed martensite. Unlike the model of Garion and Skoczeń (2002), the constitutive framework proposed in this work is based on a pure mean-field homogenization procedure: the hardening of the bi-phase material is not directly provided, but the effective material behavior is entirely determined by homogenization and the constitutive behavior of the individual phases. Both individual phases, austenite and martensite, are considered elastoplastic. A rate-independent nonlinear mixed kinematic-isotropic hardening model is used for each of the phases: the kinematic contribution follows a two-term Chaboche's law (Chaboche et al., 1979; Lemaitre and Chaboche, 1994), and the isotropic contribution uses the superposition of two exponential laws. The model adopts a Hill-type incremental formulation (Hill, 1965a). Anisotropic algorithmic tangent operators are used everywhere except in the Eshelby's tensor (Eshelby, 1957), which is computed with the isotropic form introduced by Bornert et al. (2001a,b). This specific selection of tangent stiffness operators and Eshelby's tensor is the suggested combination of Pierard and Doghri (2006) for general loading conditions. In particular, Bornert's isotropization method has been selected over the spectral decomposition method (Ponte-Castañeda, 1996; Chaboche and Kanouté, 2003) since the latter may lead to inaccurate results for non-proportional loadings and does not provide an isotropic operator for a Chaboche nonlinear kinematic hardening model (Doghri and Ouaar, 2003). Additionally, two different versions of the model are proposed based on the linear homogenization approach: one using a Mori-Tanaka scheme (Mori and Tanaka, 1973; Benveniste, 1987) and another using a Self-Consistent scheme (Hill, 1965b). The Mori-Tanaka scheme is simpler, but its validity is questioned when the matrix-particle microtopology is lost for a high volume fraction of martensite, whereas the Self-Consistent implicit scheme has no limitation on the volume fraction of transformed martensite (Böhm, 1998; Chatzigeorgiou et al., 2018). Based on the linear homogenization approach, the strain and stress fields in each individual phase are provided, which are generally different for the two phases and for the bi-phase material. Moreover, the phase transformation is described by the nonlinear kinetic law proposed by Olson and Cohen (1975). Furthermore, the constitutive model is implemented in ABAQUS/Standard through a UMAT user subroutine that uses a return mapping algorithm based on the implicit backward Euler integration scheme and provides a closed-form expression of the consistent Jacobian tensor. The material parameters for the description of the mechanical behavior of the individual phases and of the kinetics of the martensitic transformation are identified using the tensile experimental data for AISI 304L and AISI 316LN presented in Fernández-Pisón et al. (2021). Unit-cell finite element calculations with an explicit description of the martensite inclusions and the austenite matrix are carried out for different stress states with controlled triaxiality and Lode parameter under monotonic and cycling loading. Note that, since the pioneering work of Needleman (1972), finite element unit-cell computations have been extensively used to provide fundamental understanding of the mechanical response of composite aggregates (Christman et al., 1989; Shen et al., 1994; Sørensen et al., 1995; Needleman et al., 2010). The unit-cell simulations presented in this paper are performed for both constant and evolving martensite volume fractions. The comparison with the predictions of the homogenization schemes allows us to evaluate the Mori-Tanaka and Self-Consistent approaches with regard to their ability to describe the mechanical behavior of the bi-phase material. Additionally, numerical simulations of tensile tests on samples subjected to different initial temperatures are carried out to demonstrate the capability of the developed constitutive model to predict cryogenic martensitic transformation in austenitic stainless steels.

2. Constitutive framework

Two different mean-field homogenization schemes have been used to model the mechanical behavior and martensitic transformation of austenitic stainless steels subjected to cryogenic temperatures: Mori-Tanaka and Self-Consistent schemes. Section 2.1 includes the constitutive description of the individual phases; Section 2.2 presents the

kinetic law used to model the martensitic transformation; and a detailed account of the bi-phase material and the homogenization procedure can be found in Section 2.3. The γ-austenite plays the role of the matrix, while the α'-martensite takes the form of inclusions embedded in the austenite matrix. Following Stringfellow et al. (1992), Papatriantafillou (2005) and Msolli et al. (2016), among others, the martensite is represented by spherical inclusions isotropically dispersed in the material. Moreover, perfect bonding between the two constituents is assumed, as for all mean-field approaches (Böhm, 1998).

2.1. Individual phases

The constitutive description is taken to be the same for both γ-austenite and α'-martensite (hereinafter simply referred to as austenite and martensite), so that the different mechanical behavior of the phases comes from the different values of the material parameters (see Tables 1 and 2 in Section 4).

The total rate of deformation tensor $\boldsymbol{d}$ is decomposed into elastic $\boldsymbol{d}^e$ and plastic $\boldsymbol{d}^p$ components:

$$\boldsymbol{d} = \boldsymbol{d}^e + \boldsymbol{d}^p \tag{1}$$

where the elastic part of the rate of deformation tensor is related to the rate of stress by the incremental Hooke's law:

$$\dot{\boldsymbol{\sigma}}^{\nabla} = \boldsymbol{L}^e : \boldsymbol{d}^e = \boldsymbol{L}^e : (\boldsymbol{d} - \boldsymbol{d}^p) \tag{2}$$

where $(\dot{\bullet})^{\nabla}$ denotes an objective time derivative (Zaremba–Jaumann rate as in ABAQUS/Standard) of the Cauchy stress tensor $\boldsymbol{\sigma}$, and $\boldsymbol{L}^e$ is the isotropic elastic stiffness tensor:

$$\boldsymbol{L}^e = 3\kappa \boldsymbol{I}_{vol} + 2\mu \boldsymbol{I}_{dev} \tag{3}$$

with $\boldsymbol{I}_{vol} = \frac{1}{3}\mathbf{1} \otimes \mathbf{1}$ and $\boldsymbol{I}_{dev} = \boldsymbol{I} - \boldsymbol{I}_{vol}$ being the fourth-order volumetric and deviatoric projection tensors, respectively, where $\mathbf{1}$ is the second-order identity tensor and $\boldsymbol{I}$ is the fourth-order symmetric identity tensor. Moreover, $\kappa = \dfrac{E}{3(1-2\nu)}$ and $\mu = \dfrac{E}{2(1+\nu)}$ are the elastic bulk and shear moduli, respectively, where E is the Young's modulus and ν is the Poisson's ratio.

The plastic part of the rate of deformation tensor is given by the associated flow rule:

$$\boldsymbol{d}^p = \dot{\lambda} \frac{\partial F}{\partial \boldsymbol{\sigma}} \tag{4}$$

with $\dot{\lambda}$ being the rate of the plastic multiplier, where $(\dot{\bullet})$ denotes differentiation with respect to time, and F is the von Mises yield function:

$$F(\boldsymbol{\sigma}, \boldsymbol{X}, \bar{\varepsilon}^p) = \sqrt{\frac{3}{2}(\boldsymbol{s} - \boldsymbol{X}) : (\boldsymbol{s} - \boldsymbol{X})} - \left(\sigma^{y0} + R(\bar{\varepsilon}^p)\right) \leq 0 \tag{5}$$

where $\boldsymbol{s} = \boldsymbol{\sigma} - \sigma_h \mathbf{1}$ is the deviatoric part of the Cauchy stress tensor and $\sigma_h = \frac{1}{3}\boldsymbol{\sigma} : \mathbf{1}$ is the hydrostatic stress. Moreover, $\boldsymbol{X}$ is the backstress tensor for the kinematic hardening, σ^{y0} is the initial yield stress, R is the isotropic hardening function, and $\bar{\varepsilon}^p = \displaystyle\int_0^t \dot{\bar{\varepsilon}}^p(\tau) d\tau$ is the accumulated plastic strain, where $\dot{\bar{\varepsilon}}^p = \sqrt{\frac{2}{3}\boldsymbol{d}^p : \boldsymbol{d}^p}$ is the accumulated plastic strain rate (which corresponds to the rate of the plastic multiplier for von Mises plasticity).

A rate-independent nonlinear mixed kinematic-isotropic hardening model is assumed. The kinematic contribution is implemented using Chaboche's law (Chaboche et al., 1979; Lemaitre and Chaboche, 1994), in which the backstress tensor is defined with two separate equations of the form proposed by Armstrong and Frederick (Armstrong et al., 1966):

$$\boldsymbol{X} = \sum_{j=1}^{2} \boldsymbol{X}_j, \qquad \dot{\boldsymbol{X}}_j^{\nabla} = \beta \frac{2}{3} h_j \boldsymbol{d}^p - \psi_j \dot{\bar{\varepsilon}}^p \boldsymbol{X}_j \tag{6}$$

The isotropic hardening is modeled by the superposition of equivalent exponential hardening laws, so that the mixed hardening model provides the same response for monotonic proportional loading independently of the contributions from kinematic and isotropic hardening:

$$R = \sum_{j=1}^{2} R_j, \qquad R_j = (1-\beta)\frac{h_j}{\psi_j}\left(1 - e^{-\psi_j \bar{\varepsilon}^p}\right) \tag{7}$$

where h_j and ψ_j are the material parameters responsible for strain hardening and dynamic recovery, respectively. The contribution of kinematic and isotropic hardening to the mixed model is controlled by the Bauschinger parameter β, which implies a purely kinematic model if $\beta = 1$, a purely isotropic model if $\beta = 0$, and a mixed model if $0 < \beta < 1$. Note that the hardening of each individual phase (austenite and martensite) is assumed to solely depend on its own plastic strain. The consideration that the martensite phase inherits the strain-hardened dislocation structure of its parent austenite (Kula and Azrin, 1978) is not made in this paper. The reader is referred to the work of Cherkaoui et al. (1998), which provides a multiscale approach to account for this feature.

Moreover, following a Hill-type incremental formulation, the relationship between the rate of the stress tensor and the total rate of deformation is:

$$\dot{\boldsymbol{\sigma}}^{\nabla} = \boldsymbol{L}^{tan} : \boldsymbol{d} \tag{8}$$

where $\boldsymbol{L}^{tan}$ is the so-called reference modulus (see Section 6.1 in Doghri and Ouaar (2003)). In this work, the reference modulus is taken as the instantaneous algorithmic tangent operator (see Eq. (A.42) in Appendix A.1). The reader is referred to the works of Doghri and Ouaar (2003) and Pierard and Doghri (2006) to obtain insights into the differences between various reference moduli and their implications on homogenization methods.

2.2. Kinetics of martensitic transformation

The evolution of the martensite volume fraction $f_{\alpha'}$ is modeled with the sigmoidal-type kinetic relationship proposed by Olson and Cohen (1975):

$$f_{\alpha'} = 1 - e^{-\xi\left(1 - e^{-\zeta \bar{\varepsilon}_{\gamma}^p}\right)^{4.5}} \tag{9}$$

where $\bar{\varepsilon}_{\gamma}^p$ is the accumulated plastic strain in the austenite, and the parameters ζ and ξ represent the rate of shear-band formation and the probability that a shear-band intersection will result in the nucleation of martensite, respectively. The austenite volume fraction is readily computed as $f_{\gamma} = 1 - f_{\alpha'}$. It is important to note that the original kinetic relation of Olson and Cohen (1975), Eq. (9), is only valid under isothermal conditions. Moreover, it does not account for stress state and strain rate sensitivities of the martensitic transformation process, nor for a rate of change of the probability of martensite nucleation. However, especially for cryogenic temperatures, this kinetic law is very attractive due to the small number of parameters that need to be identified and to the relatively simple mechanical tests that are needed for their identification (note that tests at cryogenic temperatures are highly time- and resource-consuming). Indeed, although the original cryogenic model of Garion and Skoczeń (2002) was developed for cyclic loading, it uses a linearization of the Olson and Cohen (1975) kinetic relation. The simplified kinetic relation of Garion and Skoczeń (2002) has not been used in this work because it leads to an unrealistic non-differentiable stress–strain curve when the martensite content limit is reached.

2.3. Bi-phase material (homogenization)

The constitutive equations for the bi-phase material and the homogenization procedure are presented next, using the incremental tangent linearization method (also called Hill-type incremental formulation (Hill, 1965a)) adapted to the case of interest for which the volume fraction of the individual phases evolves. In what follows,

subscripts γ and α' are used to refer to austenite and martensite phases, respectively. Moreover, the subscripts $\gamma+\alpha'$ and HM denote the bi-phase material and the homogenized fields derived from the homogenization average theorems, respectively.

The total rate of deformation tensor of the bi-phase material $\boldsymbol{d}_{\gamma+\alpha'}$ is decomposed into elastoplastic $\boldsymbol{d}_{HM}$ and transformation $\boldsymbol{d}_{TR}$ components:

$$\boldsymbol{d}_{\gamma+\alpha'} = \boldsymbol{d}_{HM} + \boldsymbol{d}_{TR} \tag{10}$$

where the elastoplastic component corresponds to the homogenized strain rate field (recall that the total rate of deformation in the individual phases is composed of the corresponding elastic and plastic components, as shown in Eq. (1)). The transformation component is an additional inelastic term associated with the phase transformation, so it does not directly contribute to the strain-hardening of the individual phases (Stringfellow et al., 1992). This term is typically decomposed into volumetric and deviatoric parts, $\boldsymbol{d}_{TR(vol)}$ and $\boldsymbol{d}_{TR(dev)}$, respectively. The volumetric term is related to the volume change and the deviatoric term to the shape change, both resulting from the transformation process. Following Garion and Skoczeń (2002) and Homayounfard and Ganjiani (2022), among others, we only consider here the volumetric part:

$$\boldsymbol{d}_{TR} = \boldsymbol{d}_{TR(vol)} = \frac{1}{3}\dot{f}_{\alpha'}\Delta v\mathbf{1} \tag{11}$$

where $\Delta v = 0.05$ is the relative volume change during the phase transformation (Garion et al., 2006).

The rate of the stress tensor of the bi-phase material corresponds to the homogenized stress rate field:

$$\dot{\boldsymbol{\sigma}}^{\nabla}_{\gamma+\alpha'} = \dot{\boldsymbol{\sigma}}^{\nabla}_{HM} \tag{12}$$

The homogenized strain and stress fields are determined using the strain and stress average theorems: $\boldsymbol{\epsilon}_{HM} = (1-f_{\alpha'})\boldsymbol{\epsilon}_{\gamma} + f_{\alpha'}\boldsymbol{\epsilon}_{\alpha'}$ and $\boldsymbol{\sigma}_{HM} = (1-f_{\alpha'})\boldsymbol{\sigma}_{\gamma} + f_{\alpha'}\boldsymbol{\sigma}_{\alpha'}$, respectively (see Eq. (2.5) in Böhm (1998)). In this work, the definition of the strain tensor $\boldsymbol{\epsilon}$ provided by ABAQUS/Standard is adopted, $\dot{\boldsymbol{\epsilon}}^{\nabla} = \boldsymbol{d}$, see Nguyen and Waas (2016). The aforementioned average theorems lead to the following homogenized strain rate and stress rate fields:

$$\boldsymbol{d}_{HM} = \boldsymbol{d}_{HM(noTR)} + \boldsymbol{d}_{HM(TR)} \tag{13}$$

$$\dot{\boldsymbol{\sigma}}^{\nabla}_{HM} = \dot{\boldsymbol{\sigma}}^{\nabla}_{HM(noTR)} + \dot{\boldsymbol{\sigma}}^{\nabla}_{HM(TR)} \tag{14}$$

where the term denoted by the subscript $HM(noTR)$ considers a constant volume fraction of the phases and the term denoted by the subscript $HM(TR)$ accounts for the rate of martensite volume fraction:

$$\boldsymbol{d}_{HM(noTR)} = (1-f_{\alpha'})\boldsymbol{d}_{\gamma} + f_{\alpha'}\boldsymbol{d}_{\alpha'}, \qquad \boldsymbol{d}_{HM(TR)} = \dot{f}_{\alpha'}\left(\boldsymbol{\epsilon}_{\alpha'} - \boldsymbol{\epsilon}_{\gamma}\right) \tag{15}$$

$$\dot{\boldsymbol{\sigma}}^{\nabla}_{HM(noTR)} = (1-f_{\alpha'})\dot{\boldsymbol{\sigma}}^{\nabla}_{\gamma} + f_{\alpha'}\dot{\boldsymbol{\sigma}}^{\nabla}_{\alpha'}, \qquad \dot{\boldsymbol{\sigma}}^{\nabla}_{HM(TR)} = \dot{f}_{\alpha'}\left(\boldsymbol{\sigma}_{\alpha'} - \boldsymbol{\sigma}_{\gamma}\right) \tag{16}$$

The deformation rate in each individual phase (see Section 2.1) is related to the total deformation rate in the bi-phase material as follows:

$$\boldsymbol{d}_{p} = \boldsymbol{A}^{tan}_{p} : \boldsymbol{d}_{\gamma+\alpha'} \tag{17}$$

where the subscript p refers to either the austenite or the martensite phase ($p=\gamma$ or $p=\alpha'$, respectively), and $\boldsymbol{A}^{tan}_{p}$ is the instantaneous strain concentration tensor. This fourth-order tensor is given by:

$$\boldsymbol{A}^{tan}_{p} = \boldsymbol{A}^{tan}_{p(noTR)} : \left(\boldsymbol{I} + \left(\left(\boldsymbol{\epsilon}_{\alpha'} - \boldsymbol{\epsilon}_{\gamma}\right) + \frac{1}{3}\Delta v\mathbf{1}\right)\otimes\boldsymbol{\phi}\right)^{-1} \tag{18}$$

with $\boldsymbol{A}^{tan}_{p(noTR)}$ being the instantaneous strain concentration tensor for the auxiliary problem that considers a constant volume fraction of the phases:

$$\boldsymbol{d}_{p} = \boldsymbol{A}^{tan}_{p(noTR)} : \boldsymbol{d}_{HM(noTR)} \tag{19}$$

where the explicit form of $\boldsymbol{A}^{tan}_{p(noTR)}$ depends on the selected homogenization scheme (the expressions corresponding to the Mori-Tanaka and Self-Consistent approaches are provided later). The second factor in Eq. (18) results from the relationship between the total deformation rate in the bi-phase material $\boldsymbol{d}_{\gamma+\alpha'}$ and the term of the homogenized strain rate field that considers a constant volume fraction of the phases $\boldsymbol{d}_{HM(noTR)}$ (see Eqs. (A.78) in Appendix A), where the second-order tensor $\boldsymbol{\phi}$ is defined such that $\dot{f}_{\alpha'} = \boldsymbol{\phi} : \boldsymbol{d}_{HM(noTR)}$.

Mean-field homogenization schemes differ from each other by the selection of the concentration tensors. Namely, Mori-Tanaka and Self-Consistent schemes' strain concentration tensors rely on the dilute concentration tensor, which is the practical outcome of Eshelby's equivalent inclusion theory (Eshelby, 1957). This fourth-order tensor provides a relationship between the homogeneous uniform strain in an inclusion and the far-field strain in the parent medium in which the inclusion is embedded. Following the incremental tangent linearization method, the instantaneous dilute concentration tensor is given by:

$$\boldsymbol{d}_{i} = \boldsymbol{A}^{tan}_{dil(i,0)} : \boldsymbol{d}_{0}, \qquad \boldsymbol{A}^{tan}_{dil(i,0)} = \left(\boldsymbol{I} + \boldsymbol{S}^{tan\text{-}iso}_{0,spher} : \left(\boldsymbol{L}^{tan}_{0}\right)^{-1} : \left(\boldsymbol{L}^{tan}_{i} - \boldsymbol{L}^{tan}_{0}\right)\right)^{-1} \tag{20}$$

where the subscripts i and 0 refer to the inclusion and the parent medium, respectively, and $\boldsymbol{S}^{tan\text{-}iso}_{0,spher}$ is the fourth-order instantaneous Eshelby's tensor, which depends on the material properties of the parent medium and on the shape and orientation of the inclusion. The general expression of the Eshelby's tensor is rather complex (see, for example, equation (2.22) in Böhm (1998)), so in this paper we use the closed-form expression for spherical inclusions in an isotropic parent medium:

$$\boldsymbol{S}^{tan\text{-}iso}_{0,spher} = \frac{1}{3}\frac{1+\nu^{tan}_{0}}{1-\nu^{tan}_{0}}\boldsymbol{I}_{vol} + \frac{2}{15}\frac{4-5\nu^{tan}_{0}}{1-\nu^{tan}_{0}}\boldsymbol{I}_{dev} \tag{21}$$

where $\nu^{tan}_{0} = \frac{3\kappa^{tan}_{0} - 2\mu^{tan}_{0}}{2\left(3\kappa^{tan}_{0} + \mu^{tan}_{0}\right)}$ is the tangent Poisson's ratio and κ^{tan}_{0} and μ^{tan}_{0} are the tangent bulk and tangent shear moduli of the isotropic parent medium, respectively. Because the algorithmic tangent operator of the parent medium (austenite or homogenized material depending on the homogenization scheme) is anisotropic in general, the isotropic estimate proposed by Bornert et al. (2001a,b) is used (as denoted by the superscript *tan-iso* in Eshelby's tensor), resulting in $\kappa^{tan}_{0} = \frac{1}{3}\boldsymbol{I}_{vol} :: \boldsymbol{L}^{tan}_{0}$ and $\mu^{tan}_{0} = \frac{1}{10}\boldsymbol{I}_{dev} :: \boldsymbol{L}^{tan}_{0}$. Recall that the isotropic estimates are only used to compute the Eshelby's tensor, while anisotropic algorithmic tangent operators are used everywhere else.

The instantaneous strain concentration tensors of the Mori-Tanaka and Self-Consistent schemes are presented next, using the incremental tangent linearization method for the auxiliary problem that considers a constant volume fraction of the phases:

- **Mori-Tanaka scheme**. This explicit approach assumes the matrix-type phase (austenite) as the parent medium in which the particle-type phase (martensite) is embedded. According to Eshelby's theory, the two phases are related by: $\boldsymbol{d}_{\alpha'} = \boldsymbol{A}^{tan}_{dil(\alpha',\gamma)} : \boldsymbol{d}_{\gamma}$ (see the equivalence with Eq. $(20)_1$). Using the previous equation and the rate form of the strain average theorem given by Eq. $(15)_1$, the instantaneous strain concentration tensor for each phase, austenite and martensite, is given by:

$$\begin{aligned} &\boldsymbol{d}_{\gamma} = \boldsymbol{A}^{tan}_{\gamma(noTR)} : \boldsymbol{d}_{HM(noTR)}, \\ &\boldsymbol{A}^{tan}_{\gamma(noTR)} = \left(\left(1-f_{\alpha'}\right)\boldsymbol{I} + f_{\alpha'}\boldsymbol{A}^{tan}_{dil(\alpha',\gamma)}\right)^{-1} \end{aligned} \tag{22}$$

$$\begin{aligned} &\boldsymbol{d}_{\alpha'} = \boldsymbol{A}^{tan}_{\alpha'(noTR)} : \boldsymbol{d}_{HM(noTR)}, \\ &\boldsymbol{A}^{tan}_{\alpha'(noTR)} = \boldsymbol{A}^{tan}_{dil(\alpha',\gamma)} : \left(\left(1-f_{\alpha'}\right)\boldsymbol{I} + f_{\alpha'}\boldsymbol{A}^{tan}_{dil(\alpha',\gamma)}\right)^{-1} \end{aligned} \tag{23}$$

- **Self-Consistent scheme**. This implicit approach assumes the homogenized material as the parent medium in which each individual phase is treated as embedded. According to Eshelby's theory, for each phase (austenite and martensite), the instantaneous

strain concentration tensor corresponds to the instantaneous dilute concentration tensor (see the equivalence with Eq. $(20)_1$):

$$\boldsymbol{d}_{\gamma} = \boldsymbol{A}^{tan}_{\gamma(noTR)} : \boldsymbol{d}_{HM(noTR)}, \qquad \boldsymbol{A}^{tan}_{\gamma(noTR)} = \boldsymbol{A}^{tan}_{dil(\gamma,HM(noTR))} \tag{24}$$

$$\boldsymbol{d}_{\alpha'} = \boldsymbol{A}^{tan}_{\alpha'(noTR)} : \boldsymbol{d}_{HM(noTR)}, \qquad \boldsymbol{A}^{tan}_{\alpha'(noTR)} = \boldsymbol{A}^{tan}_{dil(\alpha',HM(noTR))} \tag{25}$$

where the instantaneous strain concentration tensor for each phase is dependent on the tensor $\boldsymbol{L}^{tan}_{HM(noTR)}$ (see Eq. $(20)_2$), which relates the homogenized strain rate and stress rate fields $\mathring{\boldsymbol{\sigma}}^{\nabla}_{HM(noTR)} = \boldsymbol{L}^{tan}_{HM(noTR)} : \boldsymbol{d}_{HM(noTR)}$ and is itself a function of the instantaneous strain concentration tensors, as shown by the following expression (valid for any mean-field homogenization approach):

$$\boldsymbol{L}^{tan}_{HM(noTR)} = (1 - f_{\alpha'})\boldsymbol{L}^{tan}_{\gamma} : \boldsymbol{A}^{tan}_{\gamma(noTR)} + f_{\alpha'}\boldsymbol{L}^{tan}_{\alpha'} : \boldsymbol{A}^{tan}_{\alpha'(noTR)} \tag{26}$$

which is derived from the rate form of the stress average theorem (Eq. $(16)_1$), in which the rate of the stress tensor in each phase is expressed as a function of the corresponding rate of deformation (Eq. (8)), and the latter is related to the homogenized strain rate field by the corresponding instantaneous strain concentration tensors (Eq. (19)).

3. Numerical implementation

The constitutive model has been implemented at integration point level within the finite element solver ABAQUS/ Standard using a UMAT user material subroutine. The UMAT code is included as *Supplementary Material*. Note that the subroutine is specifically designed to handle the kinetics of martensitic transformation provided by Olson and Cohen (1975). Recall that the rate of change of the probability of martensite nucleation, as well as the stress state and strain rate sensitivity of the martensitic transformation, are not considered in this isothermal kinetic relation (Section 2.2).

A sketch of the implementation procedure is shown in Fig. 1. At each time step, the total strain increment of the bi-phase material, $\Delta\boldsymbol{\epsilon}^{(n+1)}_{\gamma+\alpha'}$, together with the mechanical fields of the previous step, $\boldsymbol{\epsilon}^{(n)}_{\gamma+\alpha'}$ and $\boldsymbol{\sigma}^{(n)}_{\gamma+\alpha'}$, are provided by ABAQUS to update the stress components, $\boldsymbol{\sigma}^{(n+1)}_{\gamma+\alpha'}$, and to provide the Jacobian tensor ($DDSDDE$ as denoted in ABAQUS). State variables of the problem (SDV as denoted in ABAQUS) are the two terms of the isotropic hardening function in the two phases: R_{1_γ}, R_{2_γ}, $R_{1_{\alpha'}}$, and $R_{2_{\alpha'}}$; the accumulated plastic strain in the two phases: $\bar{\epsilon}^{p}_{\gamma}$ and $\bar{\epsilon}^{p}_{\alpha'}$; the volume fraction of martensite: $f_{\alpha'}$; the back stresses in the two phases: $\boldsymbol{X}_{1_\gamma}$, $\boldsymbol{X}_{2_\gamma}$, $\boldsymbol{X}_{1_{\alpha'}}$, and $\boldsymbol{X}_{2_{\alpha'}}$; the mechanical fields in the two phases: $\boldsymbol{\epsilon}_{\gamma}$, $\boldsymbol{\sigma}_{\gamma}$, $\boldsymbol{\epsilon}_{\alpha'}$, and $\boldsymbol{\sigma}_{\alpha'}$; the plastic strain in the two phases: $\boldsymbol{\epsilon}^{p}_{\gamma}$ and $\boldsymbol{\epsilon}^{p}_{\alpha'}$; and the algorithmic tangent operators for the two phases: $\boldsymbol{L}^{tan}_{\gamma}$ and $\boldsymbol{L}^{tan}_{\alpha'}$. The update of the internal tensorial variables at each time step during a finite strain analysis takes into account the incremental rotation of the material basis system. Thus, the second-order tensorial internal variables are rotated to the current configuration using the predefined ABAQUS function $ROTSIG$, which performs the following calculation: $\Delta\mathfrak{R}^{(n+1)}_{(n)}(\bullet)^{(n)}\Delta\mathfrak{R}^{(n+1)^{\mathrm{T}}}_{(n)}$, where $\Delta\mathfrak{R}^{(n+1)}_{(n)} = \mathfrak{R}^{(n+1)}\mathfrak{R}^{(n)^{\mathrm{T}}}$ is the incremental rotation ($DROT$ as denoted in ABAQUS). The objective increments are hence expressed as $\Delta(\bullet)^{(n+1)} = (\bullet)^{(n+1)} - \Delta\mathfrak{R}^{(n+1)}_{(n)}(\bullet)^{(n)}\Delta\mathfrak{R}^{(n+1)^{\mathrm{T}}}_{(n)}$. For the fourth-order tensorial internal variables, $\boldsymbol{L}^{tan}_{\gamma}$ and $\boldsymbol{L}^{tan}_{\alpha'}$, the operation that requires their rotations to the current configuration is performed as shown in Eq. (A.44) in Appendix A.1.

Firstly, from the total strain increment in the bi-phase material corresponding to the current time step (n+1), the contribution of each individual phase is assumed for the first ($k = 1$) iterative step of the global scheme: $\Delta\boldsymbol{\epsilon}^{(n+1)}_{\gamma(k=1)}$ and $\Delta\boldsymbol{\epsilon}^{(n+1)}_{\alpha'(k=1)}$. For the first time step ($n = 1$) it is assumed that $\Delta\boldsymbol{\epsilon}^{(n=1)}_{\gamma(k=1)} = (1 - f^{(n=1)}_{\alpha'(k=1)})\Delta\boldsymbol{\epsilon}^{(n=1)}_{\gamma+\alpha'}$ and $\Delta\boldsymbol{\epsilon}^{(n=1)}_{\alpha'(k=1)} = f^{(n=1)}_{\alpha'(k=1)}\Delta\boldsymbol{\epsilon}^{(n=1)}_{\gamma+\alpha'}$, while for the rest of the time steps $\Delta\boldsymbol{\epsilon}^{(n+1)}_{\gamma(k=1)} = \Delta\boldsymbol{\epsilon}^{(n)}_{\gamma}\left(\sqrt{\Delta\boldsymbol{\epsilon}^{(n+1)}_{\gamma+\alpha'} : \Delta\boldsymbol{\epsilon}^{(n+1)}_{\gamma+\alpha'}}/\sqrt{\Delta\boldsymbol{\epsilon}^{(n)}_{\gamma+\alpha'} : \Delta\boldsymbol{\epsilon}^{(n)}_{\gamma+\alpha'}}\right)$ and $\Delta\boldsymbol{\epsilon}^{(n+1)}_{\alpha'(k=1)} = \Delta\boldsymbol{\epsilon}^{(n)}_{\alpha'}\left(\sqrt{\Delta\boldsymbol{\epsilon}^{(n+1)}_{\gamma+\alpha'} : \Delta\boldsymbol{\epsilon}^{(n+1)}_{\gamma+\alpha'}}/\sqrt{\Delta\boldsymbol{\epsilon}^{(n)}_{\gamma+\alpha'} : \Delta\boldsymbol{\epsilon}^{(n)}_{\gamma+\alpha'}}\right)$. This is performed in the *Initialization* box represented in the figure. Subsequently, the constitutive equations for each individual phase (Section 2.1) are solved using the numerical implementation explained in Appendix A.1.

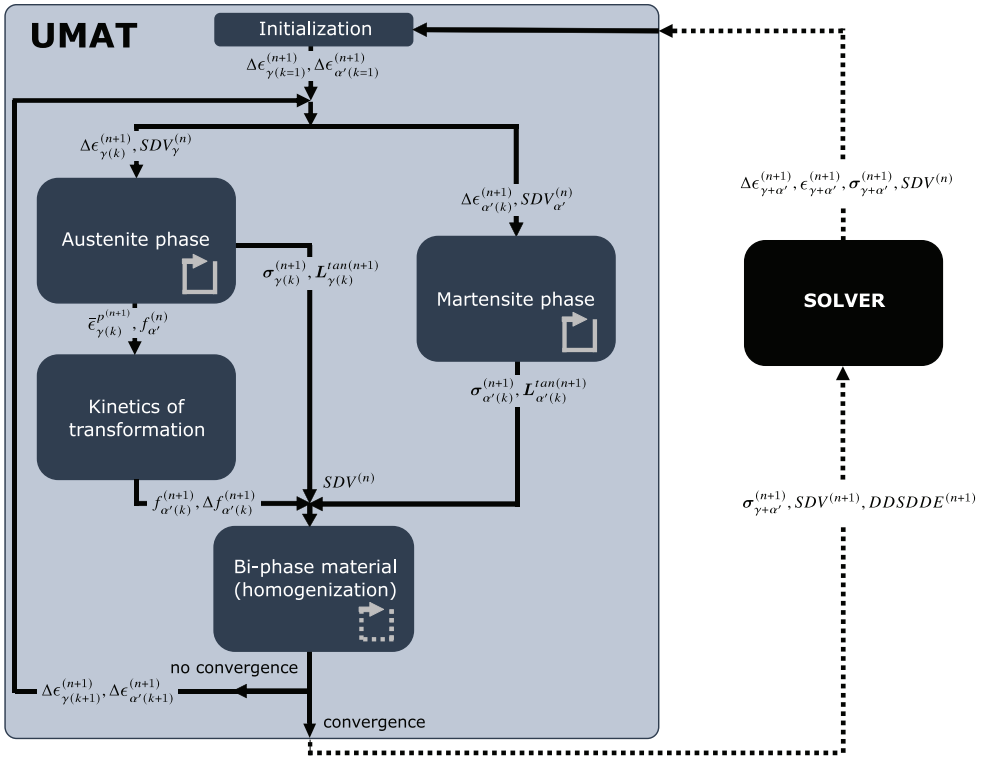

Fig. 1. Sketch of the implementation of the homogenized constitutive model (Mori-Tanaka or Self-Consistent scheme) in ABAQUS/Standard.

In the figure, this step is represented by the *Austenite phase* and *Martensite phase* boxes (notice the loop, which represents the sub-iterative process required to solve the problem). Each box uses the strain increment of the specific k-th iteration of the global iterative scheme as input, along with the internal variables of the corresponding individual phase. Once the current value of the accumulated plastic strain in the austenite phase for the k-th iteration of the global iterative scheme is known, the kinetics of martensitic transformation (Section 2.2) can be solved. This step is represented in the figure by the *Kinetics of transformation* box, and the corresponding implementation is described in Appendix A.2. Afterward, the constitutive equations for the bi-phase material (Section 2.3) are solved, and the bi-phase material's mechanical behavior is calculated for the k-th iteration of the global iterative scheme. In the figure, this step is represented by the *Bi-phase material (homogenization)* box, which uses as inputs the state variables together with the outputs of the *Austenite phase*, *Martensite phase*, and *Kinetics of transformation* boxes. The numerical implementation, which depends on the homogenization scheme (Mori-Tanaka or Self-Consistent), is described in Appendix A.3. The required iterative scheme for the implicit Self-Consistent approach is represented in the figure by a dashed loop, indicating that it is only needed if the Self-Consistent approach is selected. The outcome of the *Bi-phase material (homogenization)* box is the corrected strain increment for each individual phase. Then, the difference between the strain increment assumed at the beginning of the global iterative scheme and the corrected strain increment is calculated. If the difference is larger than a predefined tolerance, a new iteration is performed using the corrected value of the strain increment for each phase as input in the new iterative step of the global scheme: $\Delta\epsilon^{(n+1)}_{\gamma(k+1)}$ and $\Delta\epsilon^{(n+1)}_{\alpha'(k+1)}$. The whole process, which includes the *Austenite phase*, *Martensite phase*, *Kinetics of transformation*, and *Bi-phase material (homogenization)* boxes, is recomputed until the convergence condition is met. When convergence is fulfilled, the converged stress components $\boldsymbol{\sigma}^{(n+1)}_{\gamma+\alpha'}$ and state variables are given to ABAQUS/Standard. The Jacobian tensor also has to be given to ABAQUS/Standard at the end of each time step. The solver uses this tensor in its global Newton scheme to achieve an accurate assessment of the incremental kinematics. To ensure computational efficiency with fast convergence, the consistent Jacobian tensor is used; its numerical implementation is given in Appendix A.4.

4. Identification of material parameters

Two sets of material constants are to be identified: the parameters involved in the mechanical behavior of the individual phases—austenite and martensite—and the parameters involved in the kinetics of martensitic transformation. The first set of parameters consists of the Young's modulus E and the Poisson's ratio ν (Eq. (3)), the initial yield stress σ^{y0} (Eq. (5)), and the parameters describing the mixed kinematic-isotropic hardening: β, h_1, h_2, ψ_1, and ψ_2 (Eqs. (6) and (7)), all of which are specific to each individual phase. On the other hand, the parameters involved in the expression for the kinetics of martensitic transformation proposed by Olson and Cohen (1975) are ζ and ξ (Eq. (9)).

The constitutive model is calibrated to describe the mechanical behavior of two different austenitic steel grades that are widely used in superconducting magnet system applications: AISI 304L and AISI 316LN. The experiments performed by Fernández-Pisón et al. (2021) are the basis for the identification of the constitutive parameters. The data set includes uniaxial tensile stress–strain curves and the corresponding evolution of the volume fraction of martensite with the strain for the two aforementioned grades at room temperature (300 K), liquid nitrogen temperature (77 K), and liquid helium temperature (4 K); see Figs. 4, 13, and 14 therein, where the stress and strain are referred to the bi-phase material. Exceptionally, the values of the Poisson's ratio and the Bauschinger parameter, $\nu = 0.3$ and $\beta = 0.45$, respectively, are taken from Garion et al. (2006) for the same family of steels (AISI 304 and AISI 316L) at cryogenic temperatures. For these two material parameters, identical values for the two individual phases are assumed for the two grades over the whole temperature range analyzed in this work. For the rest of the parameters, an explicit temperature-evolution function is considered, and the coefficients of the function are determined by best-fit operation with the aforementioned experimental data presented in Fernández-Pisón et al. (2021). The idea is to cover the entire analyzed temperature range, unlike conventional approaches that independently determine the material parameters at a certain temperature. The temperature-evolution function selected for the material parameters involved in the mechanical behavior of the individual phases is shown in Eq. (27), which is similar to the one used by Hosseini et al. (2015) for a Chaboche kinematic hardening model. Moreover, the same functions proposed by Fernández-Pisón et al. (2021), which are based on the experimental data provided by Olson and Cohen (1975), are adopted here with regard to the material parameters involved in the kinetics of martensitic transformation, as shown in Eq. (28).

$$\begin{aligned} E(T) &= x_1\left(1 - x_2 e^{(T/x_3)}\right), \quad \sigma^{y0}(T) = x_4\left(1 - x_5 e^{(T/x_6)}\right), \\ h_1(T) &= x_7\left(1 - x_8 e^{(T/x_9)}\right), \quad h_2(T) = x_{10}\left(1 - x_{11} e^{(T/x_{12})}\right), \\ \psi_1(T) &= x_{13}\left(1 - x_{14} e^{(T/x_{15})}\right), \quad \psi_2(T) = x_{16}\left(1 - x_{17} e^{(T/x_{18})}\right) \end{aligned} \tag{27}$$

$$\zeta(T) = \frac{\zeta_2}{1 + e^{-\zeta_3(T-\zeta_1)}} - \frac{\zeta_2}{2}, \qquad \xi(T) = \frac{\xi_2}{1 + e^{-\xi_3(T-\xi_1)}} \tag{28}$$

The identification procedure is split into three parts: (i) identification of the coefficients corresponding to the material parameters of the austenite phase; (ii) identification of the coefficients corresponding to the material parameters of the martensite phase; and (iii) identification of the coefficients corresponding to the material parameters of the kinetics of martensite transformation. The determination of the coefficients is described as follows:

(i) We take as reference the aforementioned experimental stress–strain curves, but we only use the data with a strain level corresponding to a volume fraction of martensite lower than 10% (so the effect of the martensite phase on the selected data is considered to be negligible). For each grade, the selected data is represented as a $\sigma_x - \bar{\epsilon}^p - T$ surface, with σ_x being the axial stress component corresponding to the tensile loading direction, and the surface is then fitted to the function $\sigma_x = \sigma^{y0}(T) + \frac{h_1(T)}{\psi_1(T)}\left(1 - e^{-\psi_1(T)\bar{\epsilon}^p}\right) + \frac{h_2(T)}{\psi_2(T)}\left(1 - e^{-\psi_2(T)\bar{\epsilon}^p}\right)$. This function is adapted from Eq. (5), where a pure isotropic hardening is used because it is sufficient for determining the parameters (monotonic loading test). The best-fitting condition using the least squares method provides the coefficients corresponding to the functions $E(T)$, $\sigma^{y0}(T)$, $h_1(T)$, $h_2(T)$, $\psi_1(T)$, and $\psi_2(T)$ for the austenite phase (see Eq. (27)).

(ii) Unit-cell finite element calculations with a homogenized depiction of the bi-phase aggregate are performed under monotonic uniaxial tensile loading (see Section 5.1, with triaxiality $X_{\Sigma_{\gamma+\alpha'}} = 1/3$ and Lode parameter $L_{\gamma+\alpha'} = -1$). The Self-Consistent scheme version of the UMAT user subroutine described in Section 3 is employed, but the subroutine includes a simplified form of the kinetic law of martensitic transformation: $f_{\alpha'} = 1 - e^{-\xi\left(1 - e^{-\zeta\epsilon_{\gamma+\alpha'_x}}\right)^{4.5}}$, where $\epsilon_{\gamma+\alpha'_x}$ is the axial strain component of the bi-phase material that corresponds to the tensile loading direction (see Fig. 3). This simplified law reduces the coupling between the kinetics of transformation and the homogenization approach, thereby facilitating the parameter identification operation (note that in the original law, Eq. (9), the driving force for the transformation is the accumulated plastic strain in the austenite phase). The finite element calculations are performed for the AISI 304L at three different constant temperatures (300 K, 77 K, and 4 K). The calculations use the material parameters for the austenite phase identified as described in the previous paragraph as well as the material parameters for the

Table 1
Identification of the coefficients of the temperature-evolution parameters corresponding to the austenite and martensite phases and to the kinetic relation of Olson and Cohen (1975), see Eqs. (27) and (28).

AISI 304L						
	x_1 (MPa)	x_2	x_3 (K)	x_4 (MPa)	x_5	x_6 (K)
	$2.06 \cdot 10^5$	$1.52 \cdot 10^{-7}$	$2.29 \cdot 10^1$	$6.67 \cdot 10^2$	$4.77 \cdot 10^{-1}$	$1.00 \cdot 10^3$
Austenite	x_7 (MPa)	x_8	x_9 (K)	x_{10} (MPa)	x_{11}	x_{12} (K)
phase	$1.30 \cdot 10^5$	$6.84 \cdot 10^{-1}$	$1.00 \cdot 10^3$	$2.14 \cdot 10^3$	$1.61 \cdot 10^{-1}$	$1.00 \cdot 10^3$
	x_{13}	x_{14}	x_{15} (K)	x_{16}	x_{17}	x_{18} (K)
	$1.01 \cdot 10^2$	$1.42 \cdot 10^{-10}$	$1.00 \cdot 10^3$	$3.21 \cdot 10^0$	$5.80 \cdot 10^{-2}$	$1.27 \cdot 10^2$
	x_1 (MPa)	x_2	x_3 (K)	x_4 (MPa)	x_5	x_6 (K)
	$2.06 \cdot 10^5$	$1.52 \cdot 10^{-7}$	$2.29 \cdot 10^1$	$3.27 \cdot 10^3$	$6.64 \cdot 10^{-1}$	$1.00 \cdot 10^3$
Martensite	x_7 (MPa)	x_8	x_9 (K)	x_{10} (MPa)	x_{11}	x_{12} (K)
phase	$2.91 \cdot 10^3$	$4.05 \cdot 10^{-1}$	$1.00 \cdot 10^3$	$1.71 \cdot 10^4$	$5.85 \cdot 10^{-1}$	$1.00 \cdot 10^3$
	x_{13}	x_{14}	x_{15} (K)	x_{16}	x_{17}	x_{18} (K)
	$1.60 \cdot 10^1$	$5.88 \cdot 10^{-2}$	$6.67 \cdot 10^2$	$4.61 \cdot 10^0$	$2.37 \cdot 10^{-3}$	$6.09 \cdot 10^1$
Kinetic	ζ_1 (K)	ζ_2	ζ_3 (K^{-1})	ξ_1 (K)	ξ_2	ξ_3 (K^{-1})
relation	$3.36 \cdot 10^2$	$1.31 \cdot 10^1$	$-4.69 \cdot 10^{-2}$	$2.66 \cdot 10^2$	$2.10 \cdot 10^0$	$-8.80 \cdot 10^{-2}$
AISI 316LN						
	x_1 (MPa)	x_2	x_3 (K)	x_4 (MPa)	x_5	x_6 (K)
	$2.06 \cdot 10^5$	$1.52 \cdot 10^{-7}$	$2.29 \cdot 10^1$	$2.65 \cdot 10^3$	$6.63 \cdot 10^{-1}$	$9.89 \cdot 10^2$
Austenite	x_7 (MPa)	x_8	x_9 (K)	x_{10} (MPa)	x_{11}	x_{12} (K)
phase	$6.03 \cdot 10^4$	$6.66 \cdot 10^{-1}$	$9.38 \cdot 10^2$	$5.87 \cdot 10^3$	$3.14 \cdot 10^{-1}$	$4.53 \cdot 10^2$
	x_{13}	x_{14}	x_{15} (K)	x_{16}	x_{17}	x_{18} (K)
	$1.10 \cdot 10^2$	$2.40 \cdot 10^{-1}$	$1.00 \cdot 10^3$	$2.00 \cdot 10^0$	$6.94 \cdot 10^{-5}$	$9.99 \cdot 10^2$
	x_1 (MPa)	x_2	x_3 (K)	x_4 (MPa)	x_5	x_6 (K)
	$2.06 \cdot 10^5$	$1.52 \cdot 10^{-7}$	$2.29 \cdot 10^1$	$3.27 \cdot 10^3$	$6.64 \cdot 10^{-1}$	$1.00 \cdot 10^3$
Martensite	x_7 (MPa)	x_8	x_9 (K)	x_{10} (MPa)	x_{11}	x_{12} (K)
phase	$2.91 \cdot 10^3$	$4.05 \cdot 10^{-1}$	$1.00 \cdot 10^3$	$1.71 \cdot 10^4$	$5.85 \cdot 10^{-1}$	$1.00 \cdot 10^3$
	x_{13}	x_{14}	x_{15} (K)	x_{16}	x_{17}	x_{18} (K)
	$1.60 \cdot 10^1$	$5.88 \cdot 10^{-2}$	$6.67 \cdot 10^2$	$4.61 \cdot 10^0$	$2.37 \cdot 10^{-3}$	$6.09 \cdot 10^1$
Kinetic	ζ_1 (K)	ζ_2	ζ_3 (K^{-1})	ξ_1 (K)	ξ_2	ξ_3 (K^{-1})
relation	$4.62 \cdot 10^2$	$5.89 \cdot 10^0$	$-4.29 \cdot 10^{-3}$	$9.00 \cdot 10^1$	$4.84 \cdot 10^0$	$-4.94 \cdot 10^{-2}$

Table 2
Identification of the material parameters corresponding to the austenite and martensite phases and to the kinetic relation of Olson and Cohen (1975), see Eqs. (27) and (28), for the three analyzed temperatures: 300 K, 77 K, and 4 K.

		AISI 304L			AISI 316LN		
		$T = 300$ K	$T = 77$ K	$T = 4$ K	$T = 300$ K	$T = 77$ K	$T = 4$ K
	E (GPa)	191	206	206	191	206	206
	σ^{y0} (MPa)	238	323	348	272	753	888
Austenite	h_1 (MPa)	10 020	33 922	40 657	5040	16 721	19 980
phase	h_2 (MPa)	1676	1769	1795	2301	3686	4011
	ψ_1	101	101	101	74	81	83
	ψ_2	1.23	2.87	3.02	2.00	2.00	2.00
	E (GPa)	191	206	206	191	206	206
	σ^{y0} (MPa)	338	925	1090	338	925	1090
Martensite	h_1 (MPa)	1319	1638	1727	1319	1638	1727
phase	h_2 (MPa)	3581	6275	7034	3581	6275	7034
	ψ_1	14.49	14.90	15.01	14.49	14.90	15.01
	ψ_2	3.10	4.57	4.59	3.10	4.57	4.59
Kinetic	ζ	4.47	6.53	6.53	0.98	2.00	2.22
relation	ξ	0.10	2.10	2.10	0.00	3.17	4.77

kinetic relation proposed by Fernández-Pisón et al. (2021) (see Table 2 therein). Note that the material parameters for the kinetic relation are taken directly from Fernández-Pisón et al. (2021) in this step of the calibration because this former study assumed the aforementioned simplified kinetic law of martensitic transformation. Moreover, in accordance with the experiments, the bi-phase material is initially considered 100% austenite ($f_{\alpha'}^{(n=1)} = 0$). The coefficients corresponding to the functions $\sigma^{y0}(T)$, $h_1(T)$, $h_2(T)$, $\psi_1(T)$, and $\psi_2(T)$ for the martensite phase are identified for the best correlation between the numerical results and experimental tensile stress–strain curves in the bi-phase material, now covering the full range of strain shown in the source figure (Fig. 4 in Fernández-Pisón et al. (2021)). The coefficients corresponding to the function $E(T)$ are taken to be identical to those obtained for the austenite phase in accordance with Msolli et al. (2016) and Perdahcıoğlu and Geijselaers (2011a,b), among others, who make the simplifying assumption that the elastic properties of both individual phases are equal.

(iii) Unit-cell finite element calculations with a homogenized depiction of the bi-phase aggregate are performed under monotonic

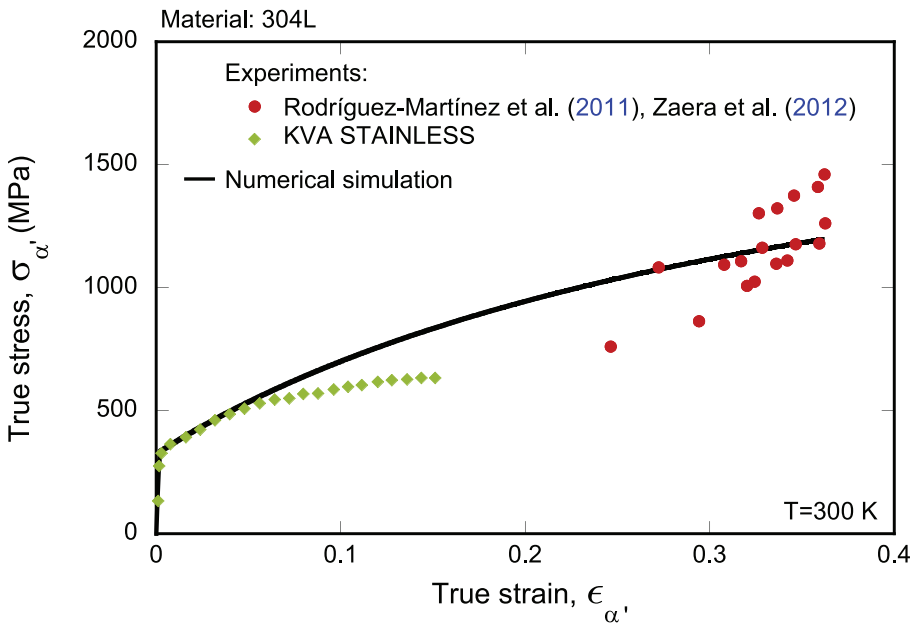

Fig. 2. Comparison of the stress–strain curve for the martensite phase resulting from the calibration performed in this work for AISI 304L and experimental data at $T = 300$ K. The results of the simulations are shown with a black solid line. The experimental data from Rodríguez-Martínez et al. (2011) and Zaera et al. (2012), red markers, corresponds to the mechanical behavior of the single martensite phase on AISI 304 samples. The experimental data supplied by the manufacturer KVA STAINLESS, green markers, corresponds to a martensitic stainless steel AISI 410 (*Data source:* https://www.kvastainless.com). (For interpretation of the references to color in this figure legend, the reader is referred to the web version of this article.)

uniaxial tensile loading. The precise Self-Consistent scheme version of the UMAT user subroutine, as described in Section 3, is employed (including the implementation of the original kinetic law of martensitic transformation shown in Eq. (9)). The finite element calculations are performed for the two grades, AISI 304L and AISI 316LN, at the three different constant temperatures. The calculations use the material parameters for the austenite and martensite phases identified as described in the previous paragraphs. The coefficients corresponding to the functions $\zeta(T)$ and $\xi(T)$ (see Eq. (28)) are identified for the best correlation between the numerical results and the experimental data of the evolution of the volume fraction of martensite with the strain in the bi-phase material reported in Fernández-Pisón et al. (2021).

Table 1 provides the final values of the coefficients for the temperature-evolution functions (Eqs. (27) and (28)). Recall that these functions and associated coefficients are meant to be valid for the three analyzed temperatures—300 K, 77 K, and 4 K—as well as for any other temperature T in the range under consideration. Particularizing these functions for the analyzed temperatures provides the material parameters given in Table 2. Note that the final material parameters for the kinetic relation (ζ and ξ) are different from the ones proposed by Fernández-Pisón et al. (2021), which have also been used here in the second step of the calibration. It is due to the fact that in the third step of the calibration, where those parameters are determined, the original kinetic law of martensitic transformation is used (Eq. (9)). Moreover, the material parameters for the martensite phase of the AISI 316LN are the same as those of the AISI 304L. This is because, unlike for AISI 304L, the experimental stress–strain curves for AISI 316LN steel do not show any significant change as martensite forms. Therefore, only the experimental stress–strain curves for AISI 304L are used to calibrate the martensite phase (as previously mentioned), and it is assumed that the flow stress and strain hardening material parameters for martensite are the same for an AISI 316LN steel grade.

Section 6.2 includes a comparison between tensile test calculations using the calibrated model and experimental data for both steel grades at the three analyzed temperatures (see Figs. 19 and 20). Since the material is initially fully austenitic, this comparison gives information on the accuracy of the calibration performed for the austenite phase. Regarding the martensite phase, the result of an additional unit-cell finite element simulation considering a non-evolving martensitic material ($f_{\alpha'} = 100\%$ and $\dot{f}_{\alpha'} = 0$) is compared with experimental stress–strain curves for martensite at $T = 300$ K taken from the literature (the authors are not aware of any experimental martensite's stress–strain curves at cryogenic temperatures). The comparison is shown in Fig. 2, where the experimental data taken from Zaera et al. (2012) corresponds to the mechanical behavior of the single martensite phase on AISI 304 samples tensile tested by Rodríguez-Martínez et al. (2011), and the experimental data supplied by the manufacturer KVA STAINLESS corresponds to a martensitic stainless steel AISI 410. A good correlation between the numerical results and the experimental data is obtained, which indicates the careful calibration developed for the martensite phase.

5. Finite element models

This section describes the main features of the finite element models created in ABAQUS/Standard to assess the Mori-Tanaka and Self-Consistent homogenization schemes with regard to their ability to describe the mechanical behavior and martensitic transformation of AISI 304L and AISI 316LN austenitic steels. Two different models have been developed: (i) a cubic unit-cell subjected to controlled macroscopic triaxiality and Lode parameter; and (ii) a flat tensile sample subjected to prescribed displacement.

5.1. Unit-cell

The reference configuration of the unit-cell is defined by the domains $0 \leq x \leq L_0$, $0 \leq y \leq L_0$, and $0 \leq z \leq L_0$, where (x, y, z) is a Cartesian coordinate system with origin located at the bottom right corner of the cell and $L_0 = 1$ mm (see Fig. 3(a)). The unit-cell plots included in Figs. 8 and 17 are referred to this coordinate system. We have performed two different types of unit-cell calculations related to the representation of the material microstructure:

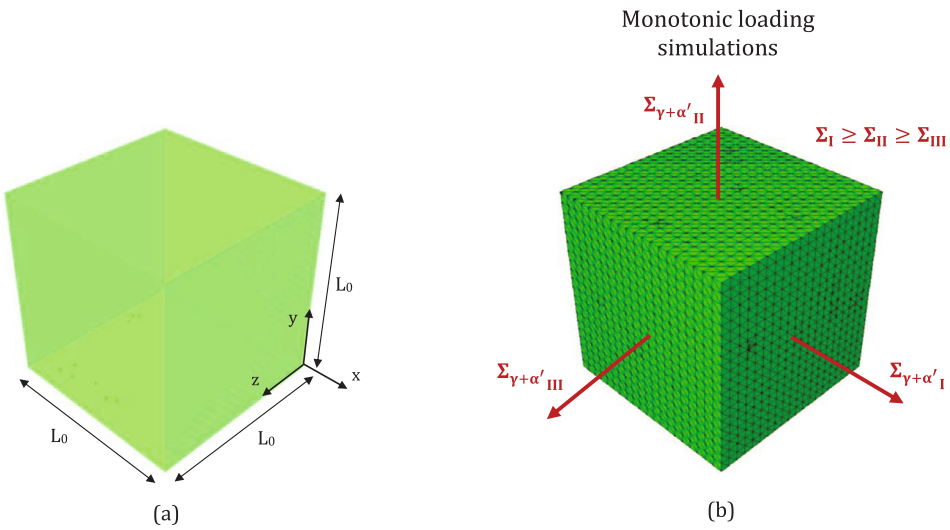

Fig. 3. Cubic unit-cell finite element model: (a) dimensions and Cartesian coordinate system (x, y, z), (b) loading directions for the case of monotonic loading simulations with $\Sigma_{\gamma+\alpha'_I}$, $\Sigma_{\gamma+\alpha'_{II}}$, and $\Sigma_{\gamma+\alpha'_{III}}$ being the principal values of the macroscopic stress tensor of the bi-phase material.

- **Explicit depiction of the martensite inclusions and the austenite matrix**. The mechanical behavior of the individual phases is modeled separately using the constitutive equations of Section 2.1. The material is considered to initially contain martensite inclusions that are represented as spherical particles which are perfectly bonded to the austenite matrix (consistent with the assumptions of the homogenization schemes, see Section 2). Different initial volume fractions of martensite have been investigated: 25%, 45%, and 65%. We have performed calculations with a single central inclusion, and with multiple inclusions distributed in the unit-cell, see Figs. 4(a) and 4(b)–(e), respectively. Note that two distinct cases with FCC-symmetric (face-centered cubic) distributions of inclusions have been examined: one involves a representative volume element with particles intersecting the unit-cell boundaries, see Fig. 4(b), while the other features a unit-cell with multiple inclusions and a boundary layer devoid of particles, see Fig. 4(c). We utilize the latter case for comparison with the configurations shown in Figs. 4(d)–(e), which include random spatial distribution of multiple inclusions and a boundary layer devoid of particles (note that models 4(b)–(c) essentially produce identical results for the same volume fraction of particles, see Section 6.1.1). The simulations with random spatial distribution of the particles have been carried out with inclusions of the same size and also with inclusions of different sizes, see Fig. 4(d)–(e). The particles with the same size have radii of 0.04475 mm, 0.054436 mm, and 0.061534 mm for the martensite volume fractions of 25%, 45%, and 65%, respectively (note that these inclusion sizes are used both in microstructures with random and FCC-symmetric spatial distributions of particles and a boundary layer devoid of inclusions, see Figs. 4(c)–(d)). For the particles with different sizes, see Fig. 4(e), following Giompliakis (2014), we use three different families of particles with radii $\{R_i, R_{ii}, R_{iii}\} = \{\frac{9}{4}R_{min}, \frac{7}{4}R_{min}, R_{min}\}$ and particle concentrations $\{F_i, F_{ii}, F_{iii}\} = \{0.5F_{\alpha'}, 0.25F_{\alpha'}, 0.25F_{\alpha'}\}$, where $F_{\alpha'}$ is the total volume fraction of martensite in the unit-cell and R_{min} is the radius used in the monodisperse microstructure such that R_{min} = 0.04475 mm, 0.054436 mm, and 0.061534 mm for $F_{\alpha'}$ = 25%, 45%, and 65%, respectively. Note that this configuration, with a boundary layer devoid of particles, is suitable for validating the results obtained with the homogenized constitutive models developed in this paper (see Section 6.1.1). Other configurations where the randomly distributed particles are allowed to intersect the boundaries while maintaining the periodicity of the unit-cell can be found in the literature. For results with these other configurations on different composite materials or where localization processes are analyzed, the reader is referred to the works of Torquato (2002) and Pierard et al. (2007). In this work, the unit-cell models (Figs. 4(a)–(e)) have been discretized with ten-node quadratic tetrahedral elements (C3D10 in ABAQUS notation), see Fig. 3(b). A very fine mesh near the spherical particles is necessary to capture the initial geometry and shape evolution of the martensite inclusions during loading. The number of elements increases with the number of inclusions and the martensite volume fraction. For the calculations with a single central particle and a martensite volume fraction of 25%, the mesh is discretized with ≈ 34000 elements, while the mesh of the unit-cell with a FCC-symmetric spatial distribution of the particles, a boundary layer devoid of particles, and 65% martensite consists of ≈ 900000 elements. A mesh sensitivity analysis has been carried out to confirm that the quantitative results and general trends provided in this paper are largely independent of the discretization (the results are not shown for the sake of brevity). A workstation AMD Milan 7453 @ 2.75 GHz with 56 cores has been used to perform the calculations. The computational cost of each simulation varied from 2 hours to 4 weeks, depending on the microstructure considered, using simultaneously all the cores of the workstation.
- **Homogenized depiction of the bi-phasic aggregate**. The effective mechanical behavior of the material is modeled using the constitutive equations of Section 2.3. Simulations are performed using both versions of the UMAT user subroutine (Section 3) corresponding to the Mori-Tanaka and Self-Consistent approaches. The unit-cell has been meshed with 12 ten-node quadratic tetrahedral elements (this is the minimum number of C3D10 elements required to model a cubic geometry). Note that the number of elements is 3000 times less than in the simulations performed with a single central martensite inclusion and 75000 times less than in the calculations with a FCC-symmetric spatial distribution of the particles, a boundary layer devoid of particles, and 65% martensite. The calculations have been performed using a single core of a laptop computer with an Intel(R) Core(TM) i5 – 8350U CPU @ 1.70 GHz. The computational cost of a simulation varied between 5 and 40 minutes, depending on the homogenization scheme considered, i.e., these calculations are significantly faster than the simulations with an explicit depiction of the martensite inclusions and the austenite matrix.

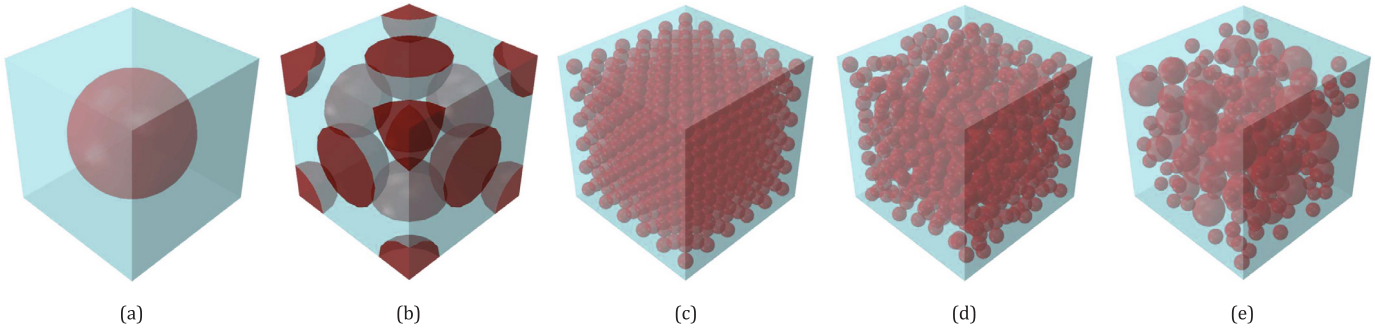

Fig. 4. Unit-cell finite element model with explicit depiction of the martensite inclusions colored in red and the austenite matrix colored in blue: (a) single central inclusion, (b) representative volume element of a FCC-symmetric spatial distribution of inclusions with the same size and particles intersecting the boundaries, (c) FCC-symmetric spatial distribution of inclusions with the same size and a boundary layer devoid of particles, (d) random spatial distribution of inclusions with the same size and a boundary layer devoid of particles, and (e) random spatial distribution of inclusions with different sizes and a boundary layer devoid of particles. The finite element models correspond to the case of $F_{\alpha'} = 25\%$. (For interpretation of the references to color in this figure legend, the reader is referred to the web version of this article.)

The macroscopic stress tensor in the unit-cell (bi-phase material) is defined as the volumetric averaging of the microscopic (local, i.e., defined at each integration point) Cauchy stress tensor $\boldsymbol{\Sigma}_{\gamma+\alpha'} = \frac{1}{V_{cell}} \int_{V_{cell}} \boldsymbol{\sigma} dV$ (Vadillo et al., 2016; Hosseini et al., 2022), with $V_{cell} = \int_{V_{cell}} dV$ being the total volume of the unit-cell. Moreover, the macroscopic strain tensor of the bi-phase material is defined as the volumetric averaging of the microscopic strain tensor $\boldsymbol{\epsilon}_{\gamma+\alpha'} = \frac{1}{V_{cell}} \int_{V_{cell}} \boldsymbol{\epsilon} dV$, where the definition of the microscopic strain tensor provided by ABAQUS/Standard has been adopted, $\dot{\boldsymbol{\epsilon}}^{\nabla} = \boldsymbol{d}$, see Nguyen and Waas (2016). Note that for the simulations with the homogenized depiction of the bi-phasic aggregate, the so-called microscopic stress and strain tensors, $\boldsymbol{\sigma}$ and $\boldsymbol{\epsilon}$, are referred to the bi-phase material, $\boldsymbol{\sigma}_{\gamma+\alpha'}$ and $\boldsymbol{\epsilon}_{\gamma+\alpha'}$, respectively, see Fig. 1. Furthermore, the formulations of the macroscopic stress and strain tensors of the bi-phase material are equivalent to the stress and strain average theorems applied in homogenization procedures, see Eq. (4.1) in Chatzigeorgiou et al. (2018) and Eq. (1.4) in Böhm (1998). Similarly, the macroscopic stress and strain tensors for each individual phase are defined as $\boldsymbol{\Sigma}_p = \frac{1}{V_p} \int_{V_{cell}} \boldsymbol{\sigma}_p dV_p$ and $\boldsymbol{\epsilon}_p = \frac{1}{V_p} \int_{V_{cell}} \boldsymbol{\epsilon}_p dV_p$, with $V_p = \int_{V_{cell}} dV_p$ being the total volume of each individual phase, where the subscript p refers to either the austenite or the martensite phase ($p = \gamma$ or $p = \alpha'$, respectively). In the simulations with explicit depiction of the martensite inclusions and the austenite matrix, the macroscopic fields of each individual phase only account for the elements whose material corresponds to this specific phase (Srivastava et al., 2015). It means that, for the martensite phase, $(\bullet)_p \, dV_p = (\bullet) \, dV$ for elements within the particles and $(\bullet)_p \, dV_p = 0$ for elements within the matrix, and the inverse for the austenite phase. On the other hand, for the simulations with the homogenized depiction of the bi-phasic aggregate, the macroscopic fields are calculated accounting for all the elements in the unit-cell using $(\bullet)_p \, dV_p = (\bullet)_p \, f_p dV$, with f_p being the microscopic volume fraction of the considered phase (see Section 2.2). Note that the formulations of the macroscopic stress and strain tensors for each individual phase are equivalent to the phase-wise uniform stress and strain fields employed in mean-field homogenization approaches, see Eq. (1.16) in Böhm (1998). Furthermore, the macroscopic volume fraction of martensite is defined as $F_{\alpha'} = \frac{1}{V_{cell}} \int_{V_{cell}} dV_{\alpha'}$ where, in simulations with explicit depiction of the martensite inclusions and the austenite matrix, $dV_{\alpha'} = dV$ for elements within the particles and $dV_{\alpha'} = 0$ for elements within the matrix; while, for the simulations with homogenized depiction of the bi-phasic aggregate, $dV_{\alpha'} = f_{\alpha'} dV$ for all the elements. Note that the terms *microscopic* and *macroscopic* adopt the conventional definitions used in unit-cell finite element simulations: *microscopic* refers to the integration point level, and *macroscopic* refers to a volumetric average in the unit-cell. Notice the difference with literature dealing exclusively with homogenization notions, where the term *macroscopic* is reserved for the bi-phase material.

The stress state in the unit-cell (bi-phase material) and in the individual phases is described by the corresponding macroscopic stress triaxiality $X_{\Sigma} = \frac{\Sigma_h}{\overline{\Sigma}}$ and macroscopic Lode parameter $L = \frac{2\Sigma_{II} - \Sigma_I - \Sigma_{III}}{\Sigma_I - \Sigma_{III}}$. Note that $\Sigma_h = \frac{\Sigma_I + \Sigma_{II} + \Sigma_{III}}{3}$ and $\overline{\Sigma} = \sqrt{\frac{3}{2} \boldsymbol{\Sigma}' : \boldsymbol{\Sigma}'}$ are the macroscopic hydrostatic stress and the macroscopic effective stress, respectively, with Σ_I, Σ_{II}, and Σ_{III} ($\Sigma_I \geq \Sigma_{II} \geq \Sigma_{III}$) being the principal values of the macroscopic stress tensor and $\boldsymbol{\Sigma}' = \boldsymbol{\Sigma} - \Sigma_h \mathbf{1}$ being the macroscopic deviatoric stress tensor. Moreover, for representation purposes, we also define a macroscopic effective strain as $\overline{\varepsilon} = \sqrt{\frac{2}{3} \boldsymbol{\varepsilon}' : \boldsymbol{\varepsilon}'}$, where $\boldsymbol{\varepsilon}' = \boldsymbol{\varepsilon} - \varepsilon_h \mathbf{1}$ is the macroscopic deviatoric strain tensor and $\varepsilon_h = \frac{\varepsilon_I + \varepsilon_{II} + \varepsilon_{III}}{3}$ is the macroscopic volumetric strain, with ε_I, ε_{II}, and ε_{III} $(\varepsilon_I \geq \varepsilon_{II} \geq \varepsilon_{III})$ being the principal values of the macroscopic strain tensor. Note that for the previous definitions, the subscripts ($\gamma + \alpha'$, γ, or α', denoting the bi-phase material, austenite phase, and martensite phase, respectively) have been omitted because these definitions can be applied separately to any of them by using the corresponding macroscopic stress and strain tensors that were previously introduced. Hereinafter, when these variables appear without a subscript, it means that they refer to the three of them separately: the bi-phase material, the austenite phase, and the martensite phase.

In the simulations, periodic boundary conditions have been applied on the unit-cell using the equations for the nodal displacements reported in Appendix A of Dakshinamurthy et al. (2021). The multi-point constraint subroutine developed by Dakshinamurthy et al. (2021) has been employed to impose controlled values of macroscopic stress triaxiality and macroscopic Lode parameter in the unit-cell (bi-phase material), $X_{\Sigma_{\gamma+\alpha'}}$ and $L_{\gamma+\alpha'}$, respectively—see also Hosseini et al. (2022) and Vishnu et al. (2023). The loading directions are parallel to the principal directions of the macroscopic stress tensor of the bi-phase material, such that the major loading direction corresponds to the principal stress direction associated with $\Sigma_{\gamma+\alpha'_I}$ and the minor loading direction corresponds to the principal stress direction associated with $\Sigma_{\gamma+\alpha'_{III}}$; see Fig. 3(b) for the case of the monotonic loading simulations (for the cyclic loading simulations, the direction of $\Sigma_{\gamma+\alpha'_I}$ and $\Sigma_{\gamma+\alpha'_{III}}$ switches, see Fig. 12).

The calculations with an explicit description of the microstructure are to be compared with the simulations performed with the Mori-Tanaka and Self-Consistent approaches to evaluate the ability of the homogenization schemes to describe the effective behavior of the bi-phase material and the individual phases. Section 6.1 includes calculations performed under monotonic and cyclic loading for different values of macroscopic triaxiality $X_{\Sigma_{\gamma+\alpha'}} = -0.5$, 0.5, 1.5, and 3 and macroscopic Lode parameter $L_{\gamma+\alpha'} = -1$, 0, and 1 for constant and evolving martensite volume fraction. The calculations are performed using the material parameters corresponding to AISI 304L austenitic stainless steel at the constant temperature of $T = 77$ K (see Table 2). Additional calculations using the material parameters for AISI 304L at

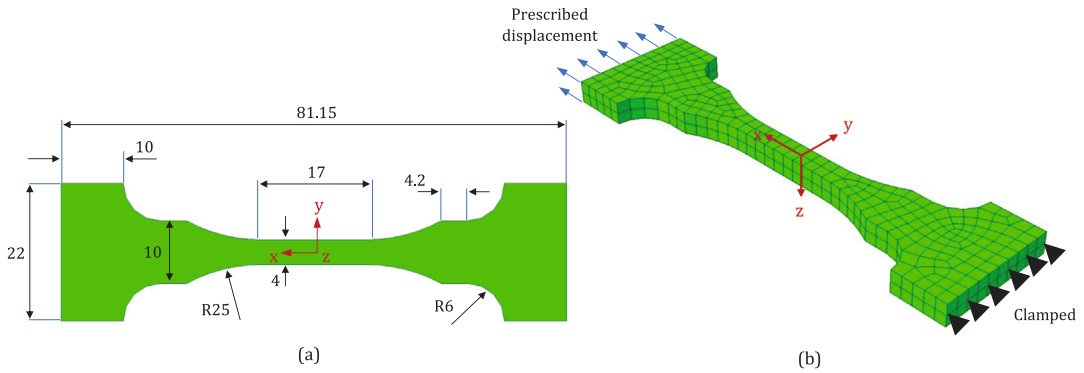

Fig. 5. Tensile sample finite element model: (a) geometry and dimensions in millimeters (thickness is 4 mm), (b) mesh and boundary conditions.

$T = 4$ K and for AISI 316LN at $T = 77$ K are presented in Appendix B and Appendix C, respectively. Note that the material parameters were identified against experiments based on the homogenized model predictions for the evolving bi-phase material under tensile loading (see Section 4). The unit-cell simulations presented in Section 6.1 do not involve any prior calibration of the homogenized model (no further calibrations were performed for constant martensite volume fractions or for different loading conditions). Therefore, the comparison between the unit-cell simulations using the homogenization schemes and the calculations with an explicit description of the microstructure (Section 6.1) is independent of the calibration procedure. The idea is to avoid using the same set of data for both parameter identification and model evaluation.

5.2. Tensile test

The geometry of the tensile sample is based on a "non-proportional test piece" according to the standard ISO-6892-4 (2015), see Fig. 5. This is the sample used by Fernández-Pisón et al. (2021) to perform the tensile experiments that are employed in Section 4 to calibrate the constitutive model. Material points are referred to using a Cartesian coordinate system with positions in the reference configuration denoted as (x, y, z), the origin of coordinates is located in the center of mass of the sample, see Fig. 5.

The boundary conditions used in the finite element model are such that the right-side surface of the sample is clamped:

$$\begin{aligned} &U_x(-40.575, y, z, t) = U_y(-40.575, y, z, t) = U_z(-40.575, y, z, t) = 0 \\ &U_{R_x}(-40.575, y, z, t) = U_{R_y}(-40.575, y, z, t) = U_{R_z}(-40.575, y, z, t) = 0 \end{aligned} \tag{29}$$

and a uniform displacement is prescribed in the axial direction on the left-side surface of the sample:

$$\begin{aligned} &U_x(40.575, y, z, t) = U_0 \\ &U_y(40.575, y, z, t) = U_z(40.575, y, z, t) = 0 \\ &U_{R_x}(40.575, y, z, t) = U_{R_y}(40.575, y, z, t) = U_{R_z}(40.575, y, z, t) = 0 \end{aligned} \tag{30}$$

where U and U_R are the displacement and rotation along a given direction (indicated by the subscript x, y, or z, see Fig. 5) and U_0 is the magnitude of the prescribed displacement, which is taken to be between 15 mm and 20 mm, depending on the sample's material (AISI 304L or AISI 316LN) and the testing temperature, in order to ensure that the material's ultimate tensile strength is attained.

Moreover, a constant temperature is imposed in the finite element simulations:

$$T(x, y, z, t) = T_0 \tag{31}$$

where T_0 is 300 K, 77 K, or 4 K. The analysis is isothermal, the sample's temperature is uniform in space and remains constant over time. This assumption is based on the observation that under cryogenic conditions and low strain rates, the heat released during the test (generated by the deformation or phase transformation) is rapidly removed by the cryogenic coolant. The reader is referred to the work of Tabin et al. (2016, 2019), which shows local temperature rises in the form of δ-Dirac function (temperature spikes) on tensile samples during testing at 4 K.

The effective mechanical behavior of the material is modeled using the constitutive equations of Section 2.3 (i.e., the homogenized depiction of the bi-phasic aggregate). Simulations are performed using the UMAT user subroutine described in Section 3. The material is considered to be fully austenitic in the undeformed configuration. The martensitic transformation occurs as the loading proceeds. The sample has been meshed with 450 eight-node tri-linear brick elements (C3D8 in ABAQUS notation). A mesh convergence study has been performed in which the time evolution of different critical output variables, namely stress, strain, volume fraction of martensite, and necking inception, were compared against different mesh sizes. While we have found some mesh sensitivity in the numerical results, we have checked that it does not significantly affect our results, neither qualitatively nor quantitatively. The calculations have been carried out using a single core of a laptop computer with an Intel(R) Core(TM) i5 – 8350U CPU @ 1.70 GHz. The computational cost of a simulation varied between 10 and 45 minutes, depending on the rate of the martensitic transformation (the calculations are faster for cases showing a slow or nonexistent transformation) and on the homogenization scheme considered (the Mori-Tanaka scheme was 10% faster than the Self-Consistent for the case with the maximum time difference between the two). Note that the computational cost is not significantly higher than in the unit-cell calculations using the same homogenized model because the unit-cell calculations include cyclic loading simulations where the accumulated macroscopic effective strain of the bi-phase material is more than three times higher than in the tensile simulations. The tensile test calculations are to be compared with the experiments of Fernández-Pisón et al. (2021) to check the ability of the developed homogenized model to predict the martensitic transformation in AISI 304L and AISI 316LN steels subjected to cryogenic temperatures (see Figs. 19 and 20).

6. Results

The calculations performed with the unit-cell model and the tensile sample are reported in Sections 6.1 and 6.2, respectively.

6.1. Unit-cell calculations

The results obtained with the explicit representation of the martensite inclusions and the austenite matrix are systematically compared to the calculations carried out using Mori-Tanaka and Self-Consistent homogenization schemes. The calculations are performed with parameters corresponding to AISI 304L steel tested at $T = 77$ K, see Table 2.

Section 6.1.1 shows results for different values of stress triaxiality $X_{\Sigma_{\gamma+\alpha'}} = -0.5$, 0.5, 1.5, and 3 and Lode parameter $L_{\gamma+\alpha'} = -1$, 0, and 1, for monotonic and cyclic loading, and for a constant volume fraction of martensite of $F_{\alpha'} = 45\%$. Section 6.1.2 includes calculations performed with two additional values of constant martensite volume fraction, $F_{\alpha'} = 25\%$ and 65%, for stress triaxiality $X_{\Sigma_{\gamma+\alpha'}} = 0.5$, and Lode parameter $L_{\gamma+\alpha'} = -1$. Simulations with evolving volume fraction of martensite for $X_{\Sigma_{\gamma+\alpha'}} = 0.5$ and $L_{\gamma+\alpha'} = -1$ are shown in Section 6.1.3. Note that the calculations presented in Sections 6.1.1 and 6.1.2 assess the predictive capacity of both homogenization models to capture the mechanical response of unit-cells with an explicit representation of the martensitic microstructure. The mechanical behavior of the individual phases in both the homogenization models and the simulations with microstructure representation is the same. It is important to emphasize that there has not been any prior calibration of the homogenized models to align with the mechanical response of the unit-cells featuring microstructure representation.

6.1.1. Salient results

Fig. 6 shows the evolution of the normalized macroscopic effective stress $\bar{\Sigma}/\sigma_\gamma^{y0}$ with the macroscopic effective strain $\bar{\varepsilon}$ for calculations with different microstructures with an explicit representation of the martensite inclusions: (a) single central particle, (b) representative volume element of a FCC-symmetric spatial distribution of inclusions with the same size and particles intersecting the boundaries, (c) FCC-symmetric spatial distribution of inclusions with the same size and a boundary layer devoid of particles and (d) random spatial distribution of particles with different sizes. The volume fraction of martensite is $F_{\alpha'} = 45\%$. The choice of this high martensite volume fraction is motivated by the fact that the model has been specifically developed for cryogenic temperatures, during which certain grades show large amount of transformed martensite. Note also that a microstructure with a random distribution of particles of the same size (similar to the one shown in Fig. 4(d) for $F_{\alpha'} = 25\%$) is not possible for $F_{\alpha'} = 45\%$ (however, other configurations that do not have the particle-free boundary layer are able to achieve larger fractions, see Torquato (2002) and Luo et al. (2023)). The results with explicit depiction of the microstructure are compared with the predictions of the Mori-Tanaka and Self-Consistent homogenization schemes for the bi-phase material, the austenite phase, and the martensite phase (for the homogenized model, a constant $f_{\alpha'} = 45\%$ is imposed). The idea is to assess the capability of the homogenized models to describe the mechanical response of the effective material and the individual phases in unit-cell calculations with an explicit description of the microstructure for

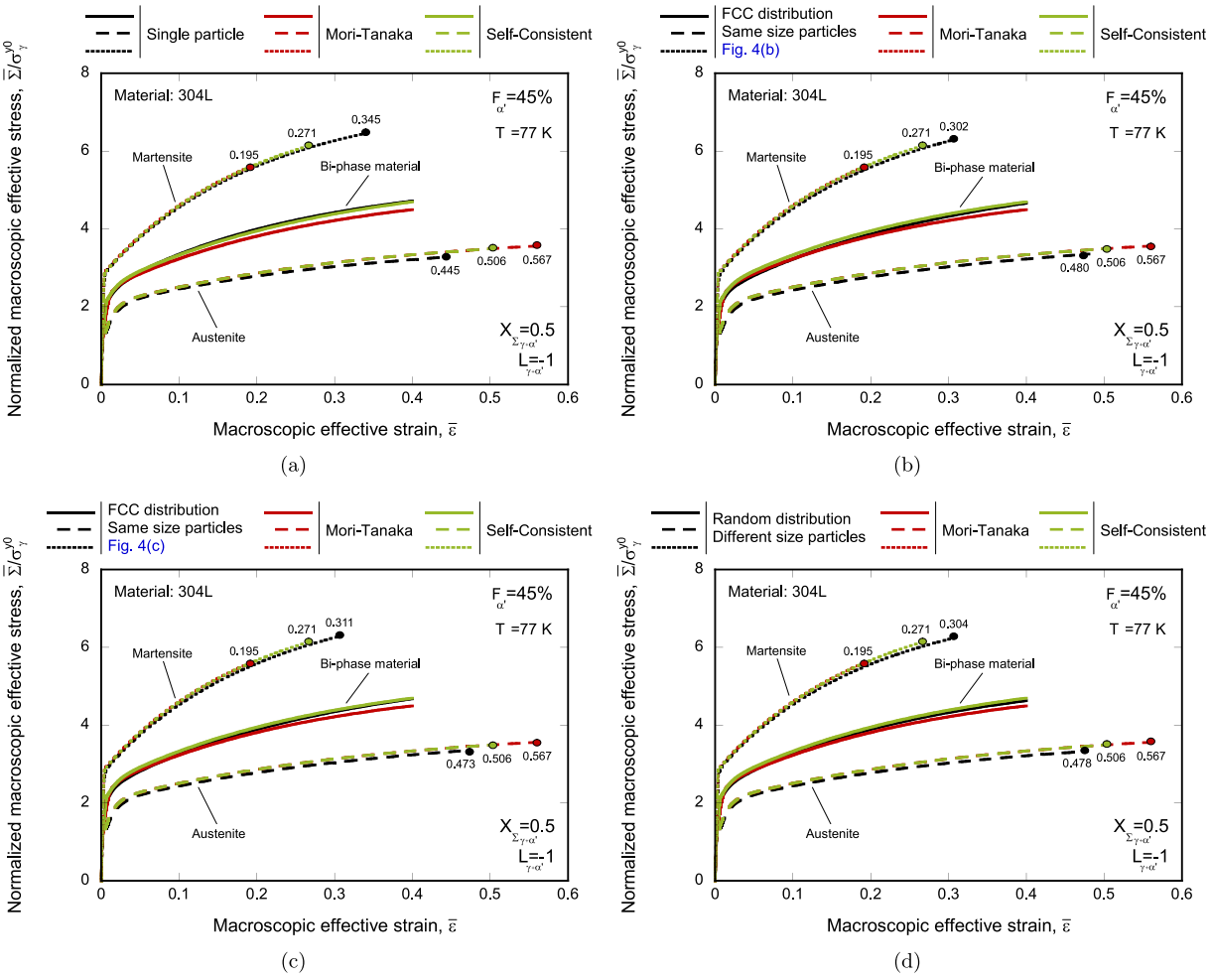

Fig. 6. Unit-cell finite element simulations. Monotonic loading. Material 304L, temperature $T = 77$ K, and volume fraction of martensite $F_{\alpha'} = 45\%$. Comparison of Mori-Tanaka and Self-Consistent homogenization schemes with calculations corresponding to different microstructures: (a) single central particle, Fig. 4(a), (b) FCC-symmetric spatial distribution of inclusions with the same size and particles intersecting the boundaries, Fig. 4(b), (c) FCC-symmetric spatial distribution of inclusions with the same size and a boundary layer devoid of particles, Fig. 4(c), and (d) random spatial distribution of particles with different sizes, Fig. 4(e). Evolution of the normalized macroscopic effective stress $\bar{\Sigma}/\sigma_\gamma^{y0}$ with the macroscopic effective strain $\bar{\varepsilon}$. Results corresponding to the bi-phase material, the austenite phase, and the martensite phase for a stress triaxiality and Lode parameter in the unit-cell equal to $X_{\Sigma_{\gamma+\alpha'}} = 0.5$ and $L_{\gamma+\alpha'} = -1$, respectively. The colored markers indicate the value of the macroscopic effective strain in the individual phases for a macroscopic effective strain in the bi-phase material of $\bar{\varepsilon}_{\gamma+\alpha'} = 0.4$. (For interpretation of the references to color in this figure legend, the reader is referred to the web version of this article.)

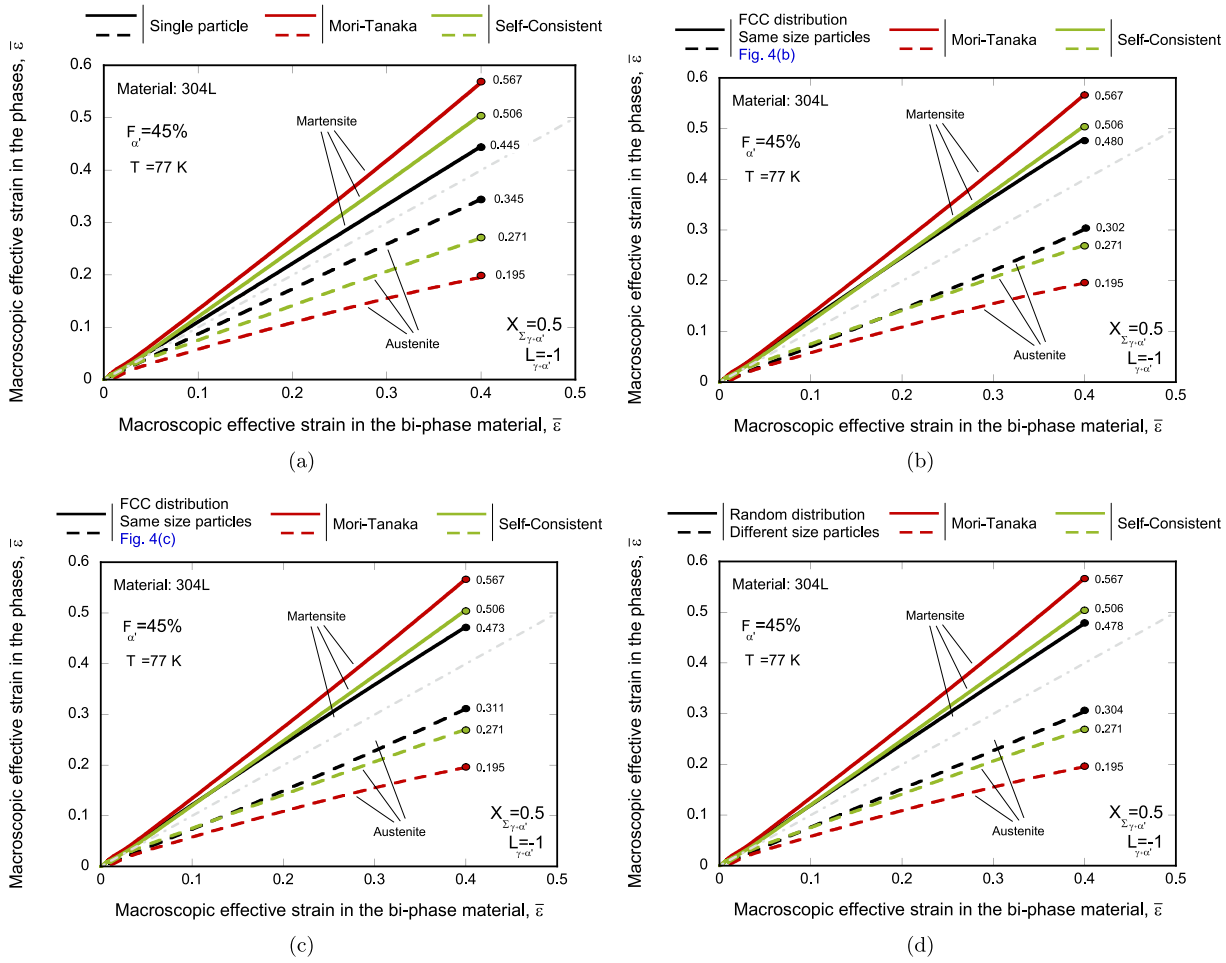

Fig. 7. Unit-cell finite element simulations. Monotonic loading. Material 304L, temperature $T = 77$ K, and volume fraction of martensite $F_{\alpha'} = 45\%$. Comparison of Mori-Tanaka and Self-Consistent homogenization schemes with calculations corresponding to different microstructures: (a) single central particle, Fig. 4(a), (b) FCC-symmetric spatial distribution of inclusions with the same size and particles intersecting the boundaries, Fig. 4(b), (c) FCC-symmetric spatial distribution of inclusions with the same size and a boundary layer devoid of particles, Fig. 4(c), and (d) random spatial distribution of particles with different sizes, Fig. 4(e). Evolution of the macroscopic effective strain in the austenite $\bar{\varepsilon}_{\gamma}$ and the martensite $\bar{\varepsilon}_{\alpha'}$ with the macroscopic effective strain in the bi-phase material $\bar{\varepsilon}_{\gamma+\alpha'}$. Results for a stress triaxiality and Lode parameter in the unit-cell equal to $X_{\Sigma_{\gamma+\alpha'}} = 0.5$ and $L_{\gamma+\alpha'} = -1$, respectively. The colored markers indicate the value of the macroscopic effective strain in the individual phases for a macroscopic effective strain in the bi-phase material of $\bar{\varepsilon}_{\gamma+\alpha'} = 0.4$. (For interpretation of the references to color in this figure legend, the reader is referred to the web version of this article.)

this specific case (martensite inclusions and austenite matrix). The calculations correspond to monotonic loading, with the stress triaxiality and Lode parameter being $X_{\Sigma_{\gamma+\alpha'}} = 0.5$ and $L_{\gamma+\alpha'} = -1$ (axisymmetric tension), respectively. The macroscopic effective strain in the bi-phase material is imposed to reach $\bar{\varepsilon}_{\gamma+\alpha'} = 0.4$, and the colored markers indicate the corresponding value of the macroscopic effective strain in the individual phases. Recall that the behavior of the individual phases is the same in both homogenization schemes and in the simulations with microstructure representation, and that the behavior of the phases was determined based on the tensile experiments presented in Fernández-Pisón et al. (2021). Consequently, the comparison performed between Mori-Tanaka and Self-Consistent predictions with unit-cell simulations including explicit representation of the austenite and martensite microstructure does not entail any a priori calibration of the homogenization schemes.

As can be seen in Fig. 6, the predictions of the homogenization schemes for the effective behavior of the bi-phase material are very close to the results obtained with the four microstructures considered (single central particle, representative volume element of a FCC-symmetric spatial distribution of inclusions with the same size and particles intersecting the boundaries, FCC-symmetric spatial distribution of inclusions with the same size and a boundary layer devoid of particles, and random spatial distribution of particles); notably, the Self-Consistent model virtually overlaps with the unit-cell calculations with explicit representation of the martensite inclusions. However, the partitioning of the strain between the two phases calculated with the homogenization schemes shows important differences with the simulations with explicit representation of the microstructure since both Self-Consistent and Mori-Tanaka underestimate the strain in the martensite and overestimate the strain in the austenite. The largest differences are obtained with the Mori-Tanaka model. For instance, for the calculation with a single central particle (see Fig. 6(a)), for a macroscopic effective strain in the bi-phase material of $\bar{\varepsilon}_{\gamma+\alpha'} = 0.4$, the Self-Consistent and Mori-Tanaka models underestimate the strain in the martensite by 20% and 45%, respectively, and overestimate the strain in the austenite by 14% and 27%. Note that, since the martensite is the hard phase, the effective strain is significantly smaller than in the austenite (as expected). In fact, the larger strain in the martensite predicted by the Self-Consistent scheme explains the slightly higher stress in the bi-phase material obtained by this scheme compared to the Mori-Tanaka scheme (the Self-Consistent $\bar{\Sigma}_{\gamma+\alpha'}/\sigma_{\gamma}^{y0} - \bar{\varepsilon}_{\gamma+\alpha'}$ curve lies above the Mori-Tanaka curve). Moreover, note that, unlike in the original model of Garion and Skoczeń (2002), the strain increment in the bi-phase material does not match the strain increment in the austenite matrix. Note also that the results shown in Figs. 6(b) and 6(c) for the representative volume element of an FCC-symmetric spatial

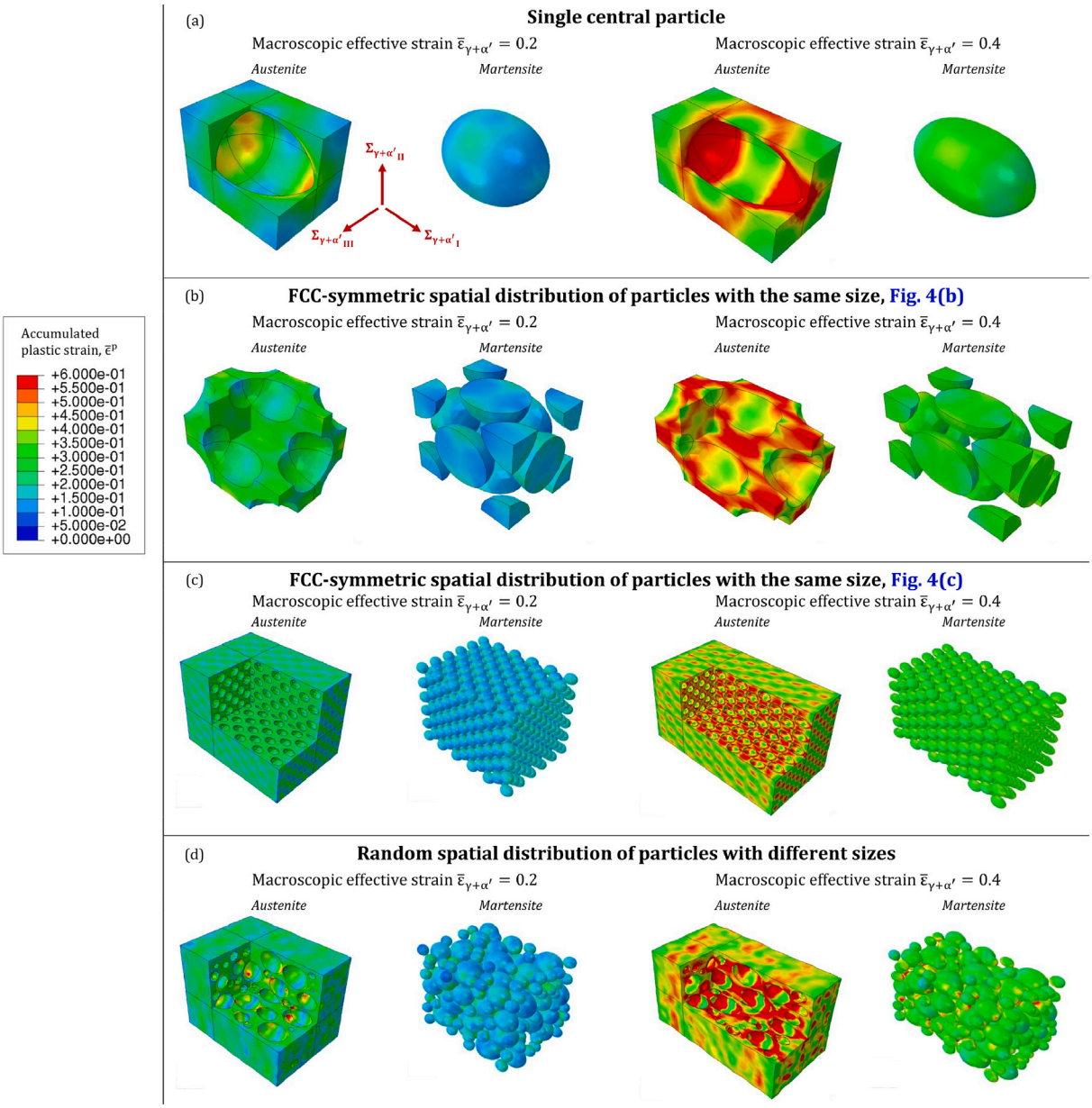

Fig. 8. Unit-cell finite element simulations. Monotonic loading. Material 304L, temperature $T = 77$ K, and volume fraction of martensite $F_{\alpha'} = 45\%$. Contours of accumulated plastic strain $\bar{\varepsilon}^p$ for calculations corresponding to different microstructures: (a) single central particle, Fig. 4(a), (b) FCC-symmetric spatial distribution of inclusions with the same size and particles intersecting the boundaries, Fig. 4(b), (c) FCC-symmetric spatial distribution of inclusions with the same size and a boundary layer devoid of particles, Fig. 4(c), and (d) random spatial distribution of particles with different sizes, Fig. 4(e). Stress triaxiality and Lode parameter in the unit-cell: $X_{\Sigma_{\gamma+\alpha'}} = 0.5$ and $L_{\gamma+\alpha'} = -1$, respectively. (For interpretation of the references to color in this figure legend, the reader is referred to the web version of this article.).

distribution of inclusions with the same size and particles intersecting the boundaries (Fig. 4(b)), and for the FCC-symmetric spatial distribution of inclusions with the same size and a boundary layer devoid of particles (Fig. 4(c)), respectively, are virtually the same. These two representations of the FCC-symmetric spatial distribution of inclusions are essentially equivalent, as expected. Furthermore, for this particular case of martensite inclusions in an austenite matrix, the FCC-symmetric spatial distribution models provide results that are very similar to those with a random spatial distribution (compare Figs. 6(b) and 6(c) with 6(d)).

Fig. 7 shows the evolution of the macroscopic effective strain in the austenite $\bar{\varepsilon}_{\gamma}$ and the martensite $\bar{\varepsilon}_{\alpha'}$ with the macroscopic effective strain in the bi-phase material $\bar{\varepsilon}_{\gamma+\alpha'}$ for the same calculations included in Fig. 6. The strain in the phases increases linearly with the strain in the bi-phase material, with a higher growth rate in the austenite and a lower one in the martensite compared to the bi-phase material (as expected since the martensite is the hard phase). Consistent with Fig. 6, the predictions of the Self-Consistent model are closer to the results obtained with the explicit description of the microstructure than those provided by the Mori-Tanaka homogenization scheme.

The different deformation of austenite matrix and martensite particles is further illustrated in the contour plots of accumulated plastic strain $\bar{\varepsilon}^p$ included in Fig. 8. Note that the results correspond to the same calculations presented in Figs. 6 and 7 with explicit representation of the microstructure. The plots correspond to two different values of the macroscopic effective strain: $\bar{\varepsilon}_{\gamma+\alpha'} = 0.2$ and $\bar{\varepsilon}_{\gamma+\alpha'} = 0.4$, showing matrix and inclusions separately. The cut-view of the matrix shows the imprint of the martensite particles, which stretch out during loading, turning into elongated spheroids with the semimajor axis parallel to the major loading direction. Note that, even when the inclusions lose their

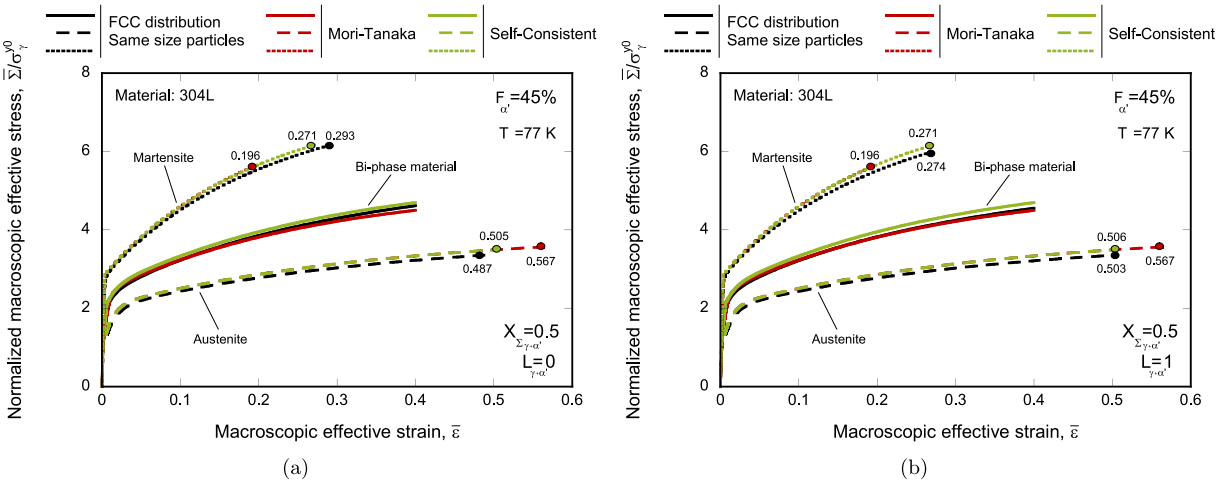

Fig. 9. Unit-cell finite element simulations. Monotonic loading. Material 304L, temperature $T = 77$ K, and volume fraction of martensite $F_{\alpha'} = 45\%$. Comparison of Mori-Tanaka and Self-Consistent homogenization schemes with calculations corresponding to the FCC-symmetric spatial distribution of inclusions with the same size and particles intersecting the boundaries, see Fig. 4(b). Evolution of the normalized macroscopic effective stress $\bar{\Sigma}/\sigma_\gamma^{y0}$ with the macroscopic effective strain $\bar{\varepsilon}$. Results corresponding to the bi-phase material, the austenite phase, and the martensite phase for stress triaxiality in the unit-cell $X_{\Sigma_{\gamma+\alpha'}} = 0.5$. Lode parameter in the unit-cell: (a) $L_{\gamma+\alpha'} = 0$ and (b) $L_{\gamma+\alpha'} = 1$. The colored markers indicate the value of the macroscopic effective strain in the individual phases for a macroscopic effective strain in the bi-phase material of $\bar{\varepsilon}_{\gamma+\alpha'} = 0.4$. (For interpretation of the references to color in this figure legend, the reader is referred to the web version of this article.)

original spherical shape, the expression used for Eshelby's tensor in the homogenized model (Eq. (21)) does not lead to inaccurate predictions of the material's effective behavior (see Figs. 6 and 9). The color coding of the isocontours is such that accumulated plastic strains ranging from 0 to 0.6 correlate with a color scale that goes from blue to red. Accumulated plastic strains above 0.6 remain red. The color maps indicate larger plastic strains and larger plastic strain gradients in the austenite compared to the martensite. Notice that the accumulated plastic strain in the particles is generally smaller than the macroscopic effective strain in the bi-phase material, while the accumulated plastic strain in the matrix is greater (as expected since the martensite is the hard phase in the bi-phase material). Namely, for the macroscopic strain $\bar{\varepsilon}_{\gamma+\alpha'} = 0.4$, the maximum accumulated plastic strain for the microstructures with a single central particle, FCC-symmetric spatial distribution of inclusions with the same size and particles intersecting the boundaries, FCC-symmetric spatial distribution of inclusions with the same size and a boundary layer devoid of particles, and a random spatial distribution of particles is 1.27, 1.40, 2.43, and 12.5, respectively (such high values are obtained because no failure criterion is used). These large values of accumulated plastic strain are located near the interface between austenite and martensite, close to the semimajor axis of the deformed particles, so that the interaction between martensite inclusions promotes plastic localization in the austenite. Furthermore, in a microstructure with randomly distributed particles, the highest accumulated plastic strain occurs in the region between closely spaced inclusions (note that the minimum allowed distance between particles in the undeformed configuration is 1 μm).

Fig. 9 shows the evolution of the normalized macroscopic effective stress $\bar{\Sigma}/\sigma_\gamma^{y0}$ with the macroscopic effective strain $\bar{\varepsilon}$ for the microstructure with FCC-symmetric spatial distribution of inclusions with the same size and particles intersecting the boundaries, see Fig. 4(b), for the Mori-Tanaka and Self-Consistent homogenization schemes. The difference with Fig. 6(b) is that the Lode parameter in the unit-cell is $L_{\gamma+\alpha'} = 0$ (generalized shear) and $L_{\gamma+\alpha'} = 1$ (axisymmetric compression) in Figs. 9(a) and 9(b), respectively. The results for the three values of the Lode parameter are very similar, with the normalized macroscopic effective stress in the bi-phase material for the FCC-symmetric distribution of particles slightly decreasing as the Lode parameter increases (notice that the homogenization scheme providing closer predictions to the $\bar{\Sigma}/\sigma_\gamma^{y0} - \bar{\varepsilon}$ curve obtained with the explicit representation of the microstructure is the Self-Consistent for $L_{\gamma+\alpha'} = -1$, and the Mori-Tanaka for $L_{\gamma+\alpha'} = 1$, compare Figs. 6(b) and 9(b)). Moreover, there is a difference in the strain in the individual phases for the calculations with explicit representation of the microstructure: the effective strain in the austenite/martensite is slightly smaller/greater for $L_{\gamma+\alpha'} = -1$ than for $L_{\gamma+\alpha'} = 1$, with $L_{\gamma+\alpha'} = 0$ representing an intermediate situation between the other two (see the colored markers and the numbers for $\bar{\varepsilon}_{\gamma+\alpha'} = 0.4$ in the legend of Figs. 6(b) and 9).

Fig. 10 includes $\bar{\Sigma}/\sigma_\gamma^{y0} - \bar{\varepsilon}$ curves obtained with the FCC-symmetric spatial distribution of inclusions with the same size and particles intersecting the boundaries, see Fig. 4(b), and with the Mori-Tanaka and Self-Consistent homogenization schemes. The difference with Fig. 6(b) is that the stress triaxiality in the unit-cell is greater: $X_{\Sigma_{\gamma+\alpha'}} = 1.5$ and $X_{\Sigma_{\gamma+\alpha'}} = 3$ in Figs. 10(a) and 10(b), respectively. The $\bar{\Sigma}/\sigma_\gamma^{y0} - \bar{\varepsilon}$ curves are virtually insensitive to the triaxiality because the individual phases are modeled using von Mises plasticity, see Section 2.1. However, the distribution of hydrostatic stress in the phases depends on the triaxiality. Figs. 11(a) and 11(b) show the evolution of the normalized macroscopic hydrostatic stress $\Sigma_h/\sigma_\gamma^{y0}$ with the macroscopic effective strain $\bar{\varepsilon}$ for the same calculations included in Figs. 10(a) and 10(b), respectively. Note that the hydrostatic stress in the bi-phase material and in the individual phases is double for $X_{\Sigma_{\gamma+\alpha'}} = 3$ than for 1.5. The Self-Consistent scheme yields $\Sigma_h/\sigma_\gamma^{y0}$ results that are very similar to the calculations with FCC-symmetric spatial distribution of particles, while the Mori-Tanaka scheme overestimates the hydrostatic stress in the martensite and underestimates the hydrostatic stress in the austenite and in the bi-phase material. For a given value of the effective strain in the individual phases, the hydrostatic stress in the martensite is higher than in the austenite (due to the higher flow strength in the martensite). However, under a given homogenization scheme, the macroscopic hydrostatic stress predicted for the bi-phase material is the same as that for the individual phases at a given value of the macroscopic effective strain in the bi-phase material (recall that the elastic properties of both individual phases are assumed to be equal). For instance, the calculations with the Self-Consistent model for $X_{\Sigma_{\gamma+\alpha'}} = 1.5$ and at $\bar{\varepsilon}_{\gamma+\alpha'} = 0.4$ predicts a normalized macroscopic hydrostatic stress of $\Sigma_h/\sigma_\gamma^{y0} = 7$ for the bi-phase material and the two individual phases (see Fig. 11(a)).

Fig. 12 compares cyclic loading results obtained with the explicit representation of a single central martensitic inclusion, see Fig. 4(a),

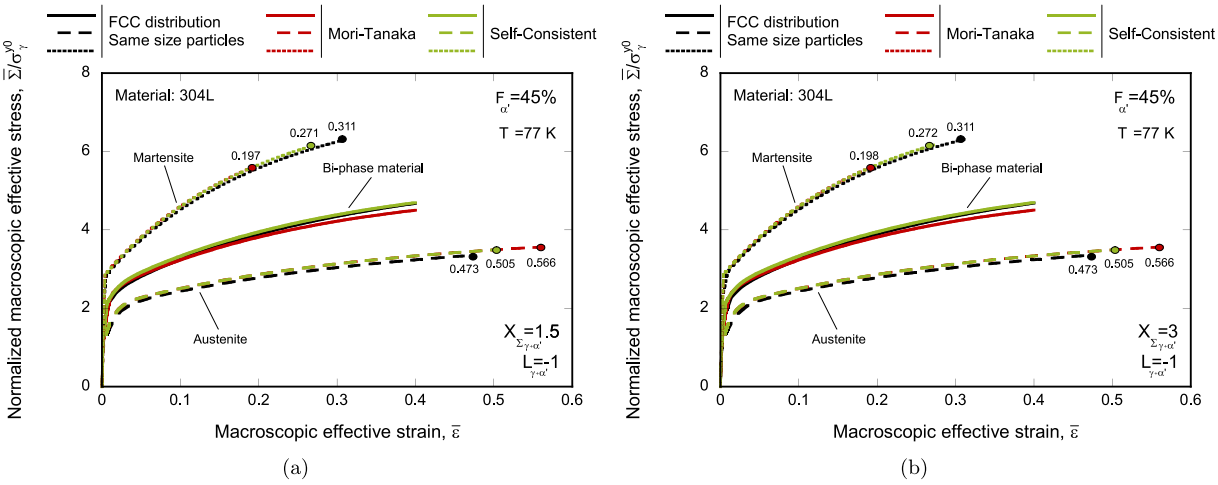

Fig. 10. Unit-cell finite element simulations. Monotonic loading. Material 304L, temperature $T = 77$ K, and volume fraction of martensite $F_{\alpha'} = 45\%$. Comparison of Mori–Tanaka and Self-Consistent homogenization schemes with calculations corresponding to the FCC-symmetric spatial distribution of inclusions with the same size and particles intersecting the boundaries, see Fig. 4(b). Evolution of the normalized macroscopic effective stress $\bar{\Sigma}/\sigma_\gamma^{y0}$ with the macroscopic effective strain $\bar{\varepsilon}$. Results corresponding to the bi-phase material, the austenite phase, and the martensite phase for the Lode parameter in the unit-cell $L_{\gamma+\alpha'} = -1$. Stress triaxiality in the unit-cell: (a) $X_{\Sigma_{\gamma+\alpha'}} = 1.5$ and (b) $X_{\Sigma_{\gamma+\alpha'}} = 3$. The colored markers indicate the value of the macroscopic effective strain in the individual phases for a macroscopic effective strain in the bi-phase material of $\bar{\varepsilon}_{\gamma+\alpha'} = 0.4$. (For interpretation of the references to color in this figure legend, the reader is referred to the web version of this article.)

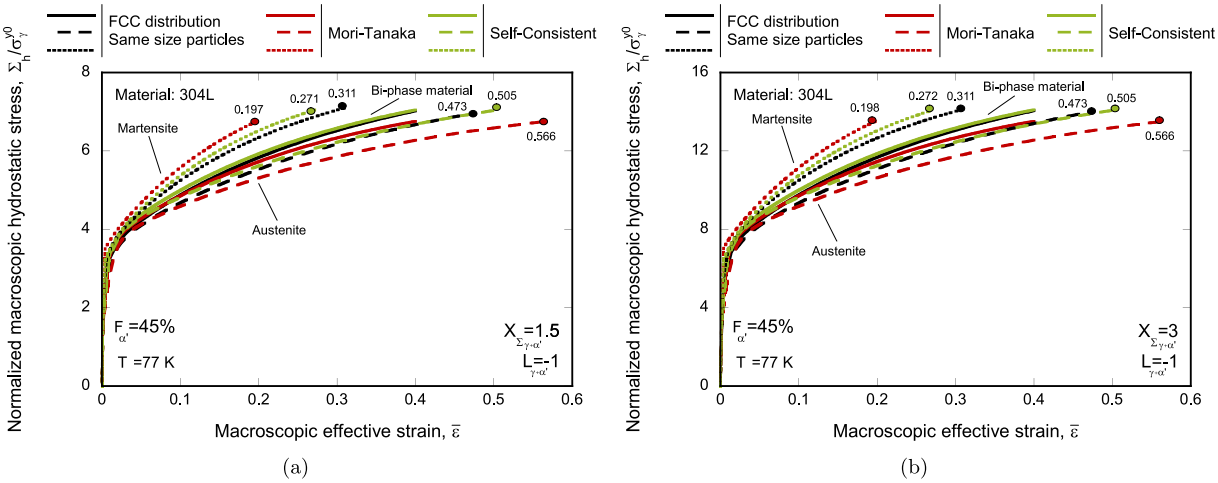

Fig. 11. Unit-cell finite element simulations. Monotonic loading. Material 304L, temperature $T = 77$ K, and volume fraction of martensite $F_{\alpha'} = 45\%$. Comparison of Mori-Tanaka and Self-Consistent homogenization schemes with calculations corresponding to the FCC-symmetric spatial distribution of inclusions with the same size and particles intersecting the boundaries, see Fig. 4(b). Evolution of the normalized macroscopic hydrostatic stress $\Sigma_h/\sigma_\gamma^{y0}$ with the macroscopic effective strain $\bar{\varepsilon}$. Results corresponding to the bi-phase material, the austenite phase, and the martensite phase for the Lode parameter in the unit-cell $L_{\gamma+\alpha'} = -1$. Stress triaxiality in the unit-cell: (a) $X_{\Sigma_{\gamma+\alpha'}} = 1.5$ and (b) $X_{\Sigma_{\gamma+\alpha'}} = 3$. The colored markers indicate the value of the macroscopic effective strain in the individual phases for a macroscopic effective strain in the bi-phase material of $\bar{\varepsilon}_{\gamma+\alpha'} = 0.4$. (For interpretation of the references to color in this figure legend, the reader is referred to the web version of this article.)

with the results from the Mori-Tanaka and Self-Consistent homogenization schemes. The normalized macroscopic effective stress $\bar{\Sigma}/\sigma_\gamma^{y0}$ is plotted against the macroscopic effective strain $\bar{\varepsilon}$ for the bi-phase material, the austenite phase, and the martensite phase in subfigures 12(a), 12(b), and 12(c), respectively. The simulations are performed for the macroscopic effective strain to vary in the bi-phase material $\bar{\varepsilon}_{\gamma+\alpha'}$ from 0.15 to −0.15. Note that the negative values of the macroscopic effective stress and the macroscopic effective strain are for representation purposes only, actually, the macroscopic effective stress and strain are always positive. The positive/negative values of the macroscopic effective strain in the bi-phase material $\bar{\varepsilon}_{\gamma+\alpha'}$ correspond to the positive/negative displacements of the unit-cell side $x = 0$ along the x-direction, see Fig. 3. Moreover, the positive values of the normalized macroscopic effective stress in the bi-phase material $\bar{\Sigma}_{\gamma+\alpha'}/\sigma_\gamma^{y0}$ correspond to $X_{\Sigma_{\gamma+\alpha'}} = 0.5$ and $L_{\gamma+\alpha'} = -1$, while the negative values corresponds to $X_{\Sigma_{\gamma+\alpha'}} = -0.5$ and $L_{\gamma+\alpha'} = 1$ (the sign of triaxiality and Lode parameter in the unit-cell switches during the simulation). For the individual phases, the positive values of the normalized macroscopic effective stress $\bar{\Sigma}_p/\sigma_\gamma^{y0}$ correspond to $L_p = -1$ and the negative values correspond to $L_p = 1$, where the subscript p refers to either the austenite or the martensite phase ($p = \gamma$ or $p = \alpha'$, respectively). The positive/negative values of the macroscopic effective strain $\bar{\varepsilon}_p$ are deduced from the shape of the $\bar{\Sigma}_p/\sigma_\gamma^{y0} - \bar{\varepsilon}_p$ curve. The simulations consist of two and a quarter cycles.

The predictions of the homogenization schemes for the bi-phase material are in satisfactory agreement with the single particle simulation results, see Fig. 12(a), notably in the case of the Self-Consistent approach (the Mori-Tanaka model slightly underestimates the effective stress). Notice that the kinematic contribution to the hardening of the individual phases (recall that the Bauschinger parameter was taken as $\beta = 0.45$ for both austenite and martensite) makes the absolute effective stress in the bi-phase material drop from 1185 MPa at the beginning of the first unloading (see the yellow marker in Fig. 12(a), $\bar{\Sigma}_{\gamma+\alpha'}/\sigma_\gamma^{y0} = 3.67$) to −113 MPa ($\bar{\Sigma}_{\gamma+\alpha'}/\sigma_\gamma^{y0} = -0.35$) when plastic strains

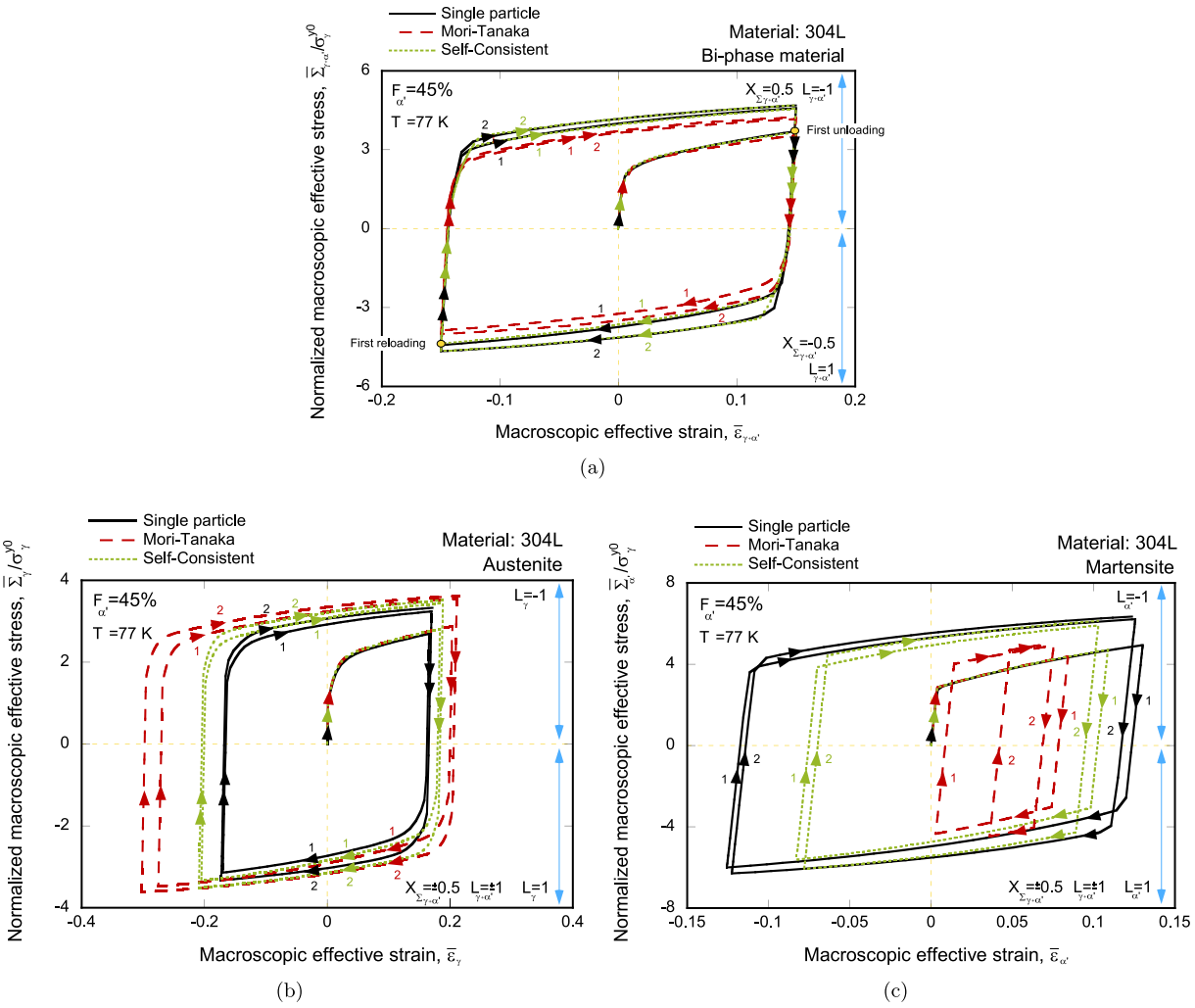

Fig. 12. Unit-cell finite element simulations. Cyclic loading. Material 304L, temperature $T = 77$ K, and volume fraction of martensite $F_{\alpha'} = 45\%$. Varying stress triaxiality $X_{\Sigma_{\gamma+\alpha'}} = \pm 0.5$ and Lode parameter $L_{\gamma+\alpha'} = \pm 1$ in the unit-cell. Comparison of Mori-Tanaka and Self-Consistent homogenization schemes with calculations corresponding to a single central particle, see Fig. 4(a). Evolution of the normalized macroscopic effective stress $\bar{\Sigma}/\sigma_\gamma^{y0}$ with the macroscopic effective strain $\bar{\varepsilon}$ varying the macroscopic effective strain of the bi-phase material between 0.15 and −0.15. Results corresponding to: (a) bi-phase material, (b) austenite phase, and (c) martensite phase. The colored arrows and numbers indicate the loading sequence and order of cycles. (For interpretation of the references to color in this figure legend, the reader is referred to the web version of this article.)

start developing again (these values refer to the unit-cell simulation performed with the Self-Consistent homogenization scheme). However, the homogenization schemes provide less accurate predictions for the mechanical behavior of the individual phases (notice that both the scale of the abscissa and ordinate axis are different in subplots 12(a), 12(b), and 12(c)). Consistent with the results shown in Figs. 6, 9, and 10, Self-Consistent and Mori-Tanaka overestimate the strain in the austenite and underestimate the strain in the martensite, with increasing differences as the number of cycles increases. Notice that the $\bar{\Sigma}/\sigma_\gamma^{y0} - \bar{\varepsilon}$ cycles predicted by the homogenization schemes for the austenite/martensite are exterior/interior to the results for the single central particle, with the cycle obtained with Mori-Tanaka displaying the largest/smallest amplitude.

6.1.2. *The effect of martensite volume fraction*

Fig. 13 shows the evolution of the normalized macroscopic effective stress $\bar{\Sigma}/\sigma_\gamma^{y0}$ with the macroscopic effective strain $\bar{\varepsilon}$ for calculations with two different microstructures: (a) single central particle, see Fig. 4(a), and (b) random spatial distribution of particles with the same size, see Fig. 4(d). The volume fraction of martensite is $F_{\alpha'} = 25\%$ in contrast to the calculations included in previous Section 6.1.1 that correspond to a larger martensite content of 45%. Note that for $F_{\alpha'} = 25\%$, it is possible to create all microstructures introduced in Fig. 4. For the sake of brevity and since it does not significantly affect the results, neither qualitatively nor quantitatively, only the calculations corresponding to the two aforementioned microstructures have been included in Fig. 13 (results for the FCC-symmetric spatial distribution of particles are provided and discussed in a following paragraph). The results are compared with the predictions of the Mori-Tanaka and Self-Consistent homogenization schemes. Recall that the homogenized models have not been calibrated to align with the mechanical response of the unit cells with an explicit representation of the microstructure. Both homogenization schemes and the explicit model use the same behavior of the individual phases, which were determined based on experimental data (see Section 4). The calculations presented in Fig. 13 correspond to monotonic loading, with the stress triaxiality and Lode parameter being $X_{\Sigma_{\gamma+\alpha'}} = 0.5$ and $L_{\gamma+\alpha'} = -1$, respectively. Similarly to the calculations performed with $F_{\alpha'} = 45\%$ in Fig. 6, the homogenization models yield results for the bi-phase material that are in agreement with the calculations with explicit representation of the microstructure, yet both Mori-Tanaka and Self-Consistent overestimate the strain in the austenite and underestimate the strain in the martensite. Moreover, note that in comparison with the results shown in Fig. 6, decreasing the volume fraction of martensite from 45% to 25% has led

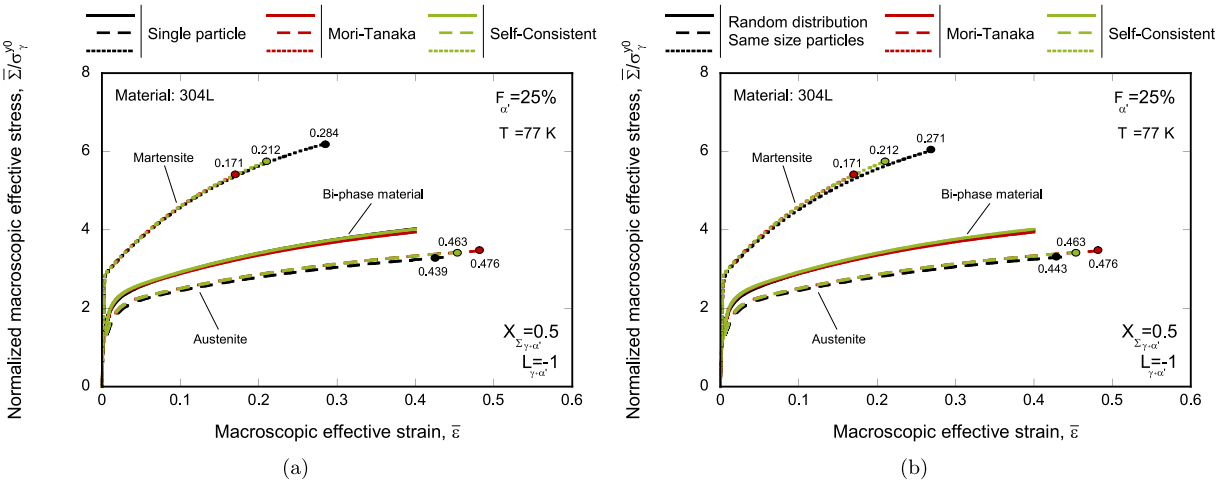

Fig. 13. Unit-cell finite element simulations. Monotonic loading. Material 304L, temperature $T = 77$ K, and volume fraction of martensite $F_{\alpha'} = 25\%$. Comparison of Mori-Tanaka and Self-Consistent homogenization schemes with calculations corresponding to two different microstructures: (a) single central particle, see Fig. 4(a), and (b) random spatial distribution of inclusions with the same size and a boundary layer devoid of particles, see Fig. 4(d). Evolution of the normalized macroscopic effective stress $\bar{\Sigma}/\sigma_\gamma^{y0}$ with the macroscopic effective strain $\bar{\varepsilon}$. Results corresponding to the bi-phase material, the austenite phase, and the martensite phase for a stress triaxiality and Lode parameter in the unit-cell equal to $X_{\Sigma_{\gamma+\alpha'}} = 0.5$ and $L_{\gamma+\alpha'} = -1$, respectively. The colored markers indicate the value of the macroscopic effective strain in the individual phases for a macroscopic effective strain in the bi-phase material of $\bar{\varepsilon}_{\gamma+\alpha'} = 0.4$. (For interpretation of the references to color in this figure legend, the reader is referred to the web version of this article.)

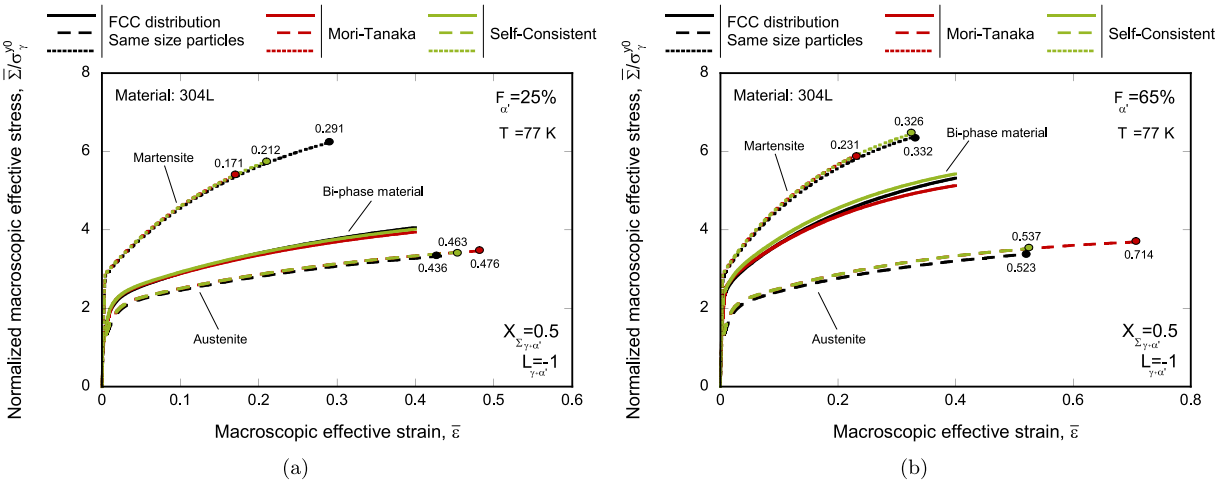

Fig. 14. Unit-cell finite element simulations. Monotonic loading. Material 304L, temperature $T = 77$ K. Comparison of Mori-Tanaka and Self-Consistent homogenization schemes with calculations corresponding to the FCC-symmetric spatial distribution of inclusions with the same size and particles intersecting the boundaries, see Fig. 4(b), for two volume fractions of martensite: (a) $F_{\alpha'} = 25\%$ and (b) $F_{\alpha'} = 65\%$. Evolution of the normalized macroscopic effective stress $\bar{\Sigma}/\sigma_\gamma^{y0}$ with the macroscopic effective strain $\bar{\varepsilon}$. Results corresponding to the bi-phase material, the austenite phase, and the martensite phase for a stress triaxiality and Lode parameter in the unit-cell equal to $X_{\Sigma_{\gamma+\alpha'}} = 0.5$ and $L_{\gamma+\alpha'} = -1$, respectively. The colored markers indicate the value of the macroscopic effective strain in the individual phases for a macroscopic effective strain in the bi-phase material of $\bar{\varepsilon}_{\gamma+\alpha'} = 0.4$. (For interpretation of the references to color in this figure legend, the reader is referred to the web version of this article.)

to a decrease in the normalized macroscopic effective stress of $\approx 30\%$ for a macroscopic effective strain of $\bar{\varepsilon}_{\gamma+\alpha'} = 0.4$.

The effect of the martensite volume fraction is further investigated in Fig. 14, which shows the evolution of the normalized macroscopic effective stress $\bar{\Sigma}/\sigma_\gamma^{y0}$ with the macroscopic effective strain $\bar{\varepsilon}$ for calculations performed with the FCC-symmetric spatial distribution of inclusions with the same size and particles intersecting the boundaries, see Fig. 4(b). Two different values of the volume fraction of martensite are considered, $F_{\alpha'} = 25\%$ in subplot 14(a) and $F_{\alpha'} = 65\%$ in subplot 14(b). Note that neither the single central inclusion nor the random spatial distribution of inclusions with a boundary layer devoid of particles are possible for $F_{\alpha'} = 65\%$. The results are compared with the predictions obtained from Mori-Tanaka and Self-Consistent models (for the homogenized models, a constant $f_{\alpha'} = 25\%$ and $f_{\alpha'} = 65\%$ is imposed, corresponding to subplots 14(a) and 14(b), respectively). Notice that the macroscopic effective stress is shifted upward as the volume fraction of martensite increases. For instance, the calculations with the FCC-symmetric spatial distribution of particles predict that the value of $\bar{\Sigma}_{\gamma+\alpha'}/\sigma_\gamma^{y0}$ for $\bar{\varepsilon}_{\gamma+\alpha'} = 0.4$ is 4.06 for $F_{\alpha'} = 25\%$, and 5.32 for $F_{\alpha'} = 65\%$. The predictions of the homogenization schemes for the effective behavior of the bi-phase material are close to the results obtained with the FCC-symmetric distribution of particles for both analyzed volume fractions of martensite. The $\bar{\Sigma}_{\gamma+\alpha'}/\sigma_\gamma^{y0} - \bar{\varepsilon}_{\gamma+\alpha'}$ curves predicted by the two homogenization models differ more as the volume fraction of martensite increases, with the curve corresponding to the Self-Consistent scheme lying above the one corresponding to the Mori-Tanaka model, which is explained by the higher strain in the martensite for the Self-Consistent scheme. In fact, there are notable differences in the results obtained from the two homogenization schemes for the partitioning of the strain between the phases. Specifically, for the Self-Consistent model, the predictions are closer to the calculations with explicit representation of the microstructure as the volume of martensite increases, while in the case of the Mori-Tanaka model, the

predictions are less accurate. These results are consistent with the fact that the validity of the Mori-Tanaka scheme is questioned when the matrix-particle microtopology is lost for a high volume fraction of martensite (see Section 1, and Böhm (1998) and Chatzigeorgiou et al. (2018)). On the other hand, notice the exceptional quantitative agreement between the Self-Consistent predictions and the results of the FCC-symmetric distribution of particles for $F_{\alpha'} = 65\%$ (less than 3% and 2% difference in the macroscopic effective strain in the austenite and the martensite, respectively, for a macroscopic strain in the bi-phase material of $\bar{\varepsilon}_{\gamma+\alpha'} = 0.4$).

6.1.3. The effect of martensitic transformation

Fig. 15(a) shows the predictions of Mori-Tanaka and Self-Consistent homogenization schemes for the evolution of the normalized macroscopic effective stress $\bar{\Sigma}/\sigma_{\gamma}^{y0}$ with the macroscopic effective strain $\bar{\varepsilon}$ for the bi-phase material and the individual phases. The results correspond to monotonic loading, temperature $T = 77$ K, stress triaxiality $X_{\Sigma_{\gamma+\alpha'}} = 0.5$ and Lode parameter $L_{\gamma+\alpha'} = -1$. Fig. 15(b) displays the corresponding evolution of the macroscopic volume fraction of martensite $F_{\alpha'}$ (%) with the macroscopic effective strain in the bi-phase material $\bar{\varepsilon}_{\gamma+\alpha'}$. Note that the scale of the abscissa axis in Fig. 15(b) is four times smaller than in Fig. 15(a) for better visualization of the martensitic transformation. Recall that the behavior of the individual phases and the kinetics of the martensitic transformation are the same in both homogenization schemes and were determined based on the tensile experiments presented in Fernández-Pisón et al. (2021).

The $\bar{\Sigma}/\sigma_{\gamma}^{y0} - \bar{\varepsilon}$ curves shown in Fig. 15 (a) for the bi-phase material display a sigmoidal-type shape due to the transformation of austenite into martensite. At the beginning of the loading process, the effective stress in the bi-phase material corresponds to the effective stress in the austenite (the bi-phase material is initially 100% austenite). As the loading continues, the formation of martensite leads to a rapid increase of the effective stress in the bi-phase material, which eventually approaches the effective stress of the martensite (e.g., for $\bar{\varepsilon}_{\gamma+\alpha'} = 0.1$ both Mori-Tanaka and Self-Consistent predict 8.6% of martensite; and for $\bar{\varepsilon}_{\gamma+\alpha'} = 0.2$, they predict 84.7% and 76.7%, respectively, see Fig. 15(b)). The differences in the effective stress of the bi-phase material ultimately come from the differences in the partitioning of the strain between the two phases predicted by the two homogenization schemes. On the one hand, the greater strain in the austenite computed with the Mori-Tanaka model (see Fig. 15(a)) makes the volume fraction of transformed martensite increase faster (see Fig. 15(b)). Note that the law of Olson and Cohen (1975) solely depends on the accumulated plastic strain in the austenite, see Eq. (9). Moreover, this faster transformation for the Mori-Tanaka model implies a faster increase in the macroscopic effective stress of the bi-phase material since, as concluded from Section 6.1.2, a higher martensite volume fraction yields a higher effective stress (compare Figs. 6(b) and 14). On the other hand, for a similar martensite volume fraction (large strain values where the transformation is close to saturation, see Fig. 15(b)), the greater strain in the martensite predicted by the Self-Consistent model makes the effective stress in the bi-phase material to increase (see Fig. 15(a)). These results make apparent the effect of the homogenization scheme on the kinetics of the phase transformation.

Fig. 16 presents results for a unit-cell that contains a single central austenite particle, see Fig. 4(a), of 45% volume which is modeled with Mori-Tanaka and Self-Consistent homogenization schemes (separately) while accounting for the martensitic transformation. The matrix material surrounding the inclusion is modeled as non-transforming austenite. The difference with respect to the results in Fig. 15 is that only the inclusion (instead of the whole unit-cell) may transform. The idea is to model the formation of a martensite inclusion in an initially (fully) austenitic material. Also, the idea is to analyze the non-uniform distribution of martensite in the particle since, in the previous simulations, the microscopic volume fraction of martensite was always uniform and equal to the macroscopic value. Note that this configuration could also be used to analyze TRIP steels by simply modeling the matrix material as a non-transforming ferrite. Fig. 16(a) shows the evolution of the normalized macroscopic effective stress $\bar{\Sigma}/\sigma_{\gamma}^{y0}$ with the macroscopic effective strain $\bar{\varepsilon}$ for the bi-phase material and the individual phases, while Fig. 16(b) includes the evolution of the macroscopic volume fraction of martensite $F_{\alpha'}$ (%) with the macroscopic effective strain in the bi-phase material $\bar{\varepsilon}_{\gamma+\alpha'}$. Note that, unlike Fig. 15, the scale of the abscissa axis in Figs. 16(a) and Fig. 16(b) is the same.

The calculation results shown in Fig. 16 yield the same qualitative results as the ones in Fig. 15. The Mori-Tanaka scheme predicts less/more strain in the martensite/austenite than the Self-Consistent model and thus faster martensite transformation, which yields greater strain hardening and effective stress in the bi-phase material for intermediate values of the macroscopic effective strain (greater strain hardening within the range 0.14–0.17 and greater effective stress within

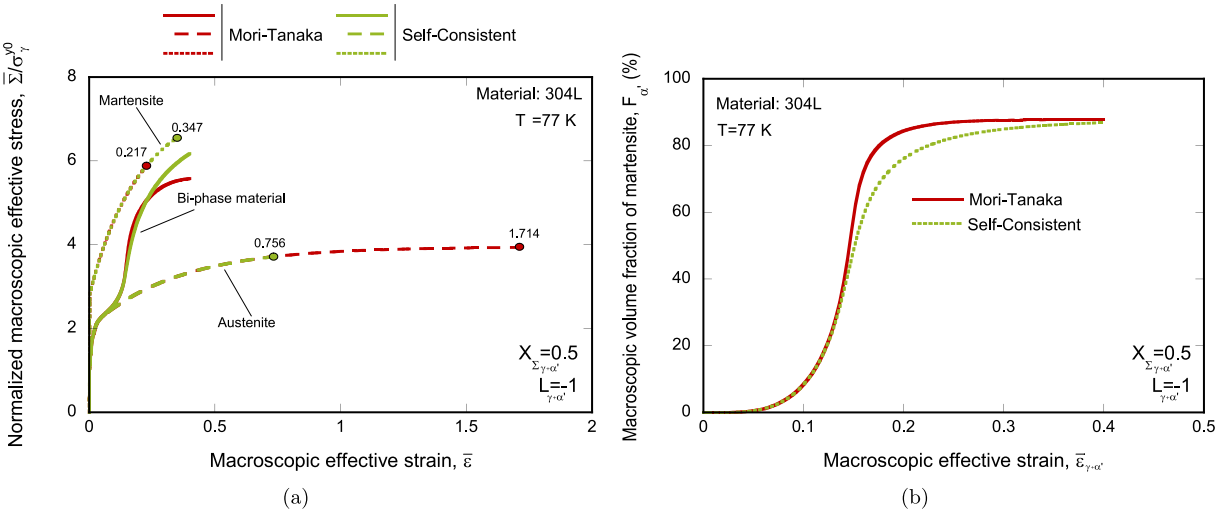

Fig. 15. Unit-cell finite element simulations. Monotonic loading. Material 304L, temperature $T = 77$ K. Stress triaxiality and Lode parameter in the unit-cell are $X_{\Sigma_{\gamma+\alpha'}} = 0.5$ and $L_{\gamma+\alpha'} = -1$, respectively. Comparison of Mori-Tanaka and Self-Consistent homogenization schemes. (a) Evolution of the normalized macroscopic effective stress $\bar{\Sigma}/\sigma_{\gamma}^{y0}$ with the macroscopic effective strain $\bar{\varepsilon}$. The red and green markers indicate the value of the macroscopic effective strain in the individual phases for a macroscopic effective strain in the bi-phase material of $\bar{\varepsilon}_{\gamma+\alpha'} = 0.4$. (b) Evolution of the macroscopic volume fraction of martensite $F_{\alpha'}$ (%) with the macroscopic effective strain in the bi-phase material $\bar{\varepsilon}_{\gamma+\alpha'}$. (For interpretation of the references to color in this figure legend, the reader is referred to the web version of this article.)

the range 0.14 − 0.24) and lower strain hardening and effective stress for larger strain values, see Fig. 16(a). The rapid martensitic transformation increases the hardening rate, while the high martensite volume fraction and the large strain in the martensite increase the effective stress. Note that the maximum difference in the martensite volume fraction between Mori-Tanaka and Self-Consistent models shown in Fig. 16(b) corresponds to $\bar{\varepsilon}_{\gamma+\alpha'} = 0.16$. For this value of the macroscopic effective strain in the bi-phase material, the volume fraction of martensite in the unit-cell (referred to as the macroscopic volume fraction of martensite $F_{\alpha'}$) is 33% and 27% for Mori-Tanaka and Self-Consistent models, respectively, while the fraction of the austenite particle that has transformed into martensite amounts to 74.2% and 61.2%, respectively. The contours of the microscopic volume fraction of martensite included in Fig. 17 show that, as expected, the transformation does not occur uniformly throughout the particle (the cut-view has been included to expose the non-uniform transformation inside of the particle). Note that a microscopic volume fraction of martensite equal to $f_{\alpha'} = 100\%$, would mean that the given element has been completely transformed into martensite. Moreover, Fig. 18 shows the evolution of the microscopic volume fraction of martensite $f_{\alpha'}$ (%) along the normalized major semi-axis of the inclusion $\bar{x}$ measured along the white solid line indicated in Fig. 17 (note that the data plotted in Fig. 18 covers the entire major semi-axis of the inclusion). The results correspond to three different values of the macroscopic effective strain in the bi-phase material $\bar{\varepsilon}_{\gamma+\alpha'} = 0.08$, 0.16 and 0.24 (see yellow and blue markers in Fig. 16(b)). Note that $\bar{\varepsilon}_{\gamma+\alpha'} = 0.16$ corresponds to the contour plots shown in Fig. 17. For $\bar{\varepsilon}_{\gamma+\alpha'} = 0.08$, the martensite volume fraction is relatively small $\approx$ 3.5%, and it is evenly distributed throughout the

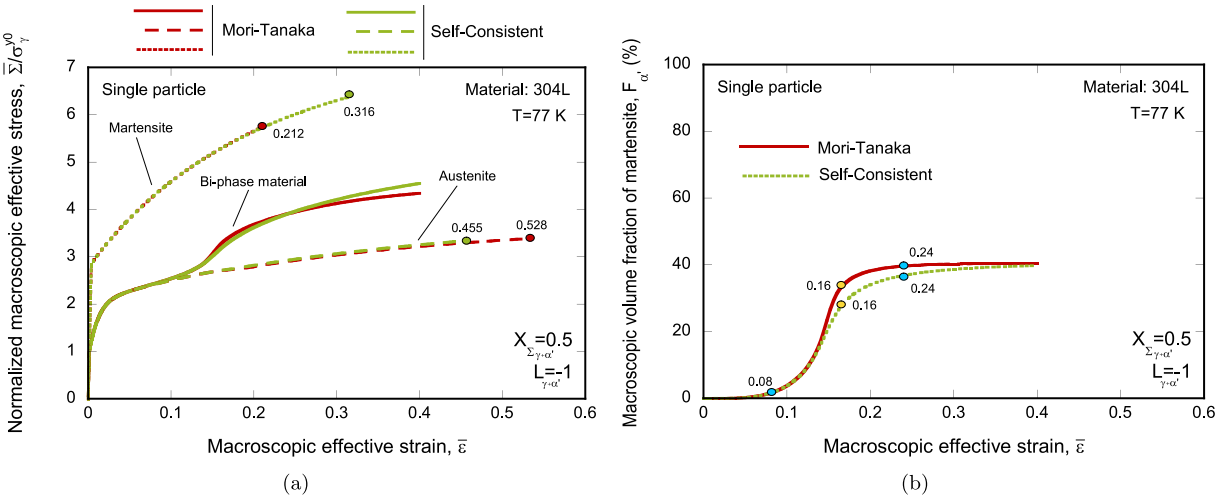

Fig. 16. Unit-cell finite element simulations. Monotonic loading. Material 304L, temperature $T = 77$ K. Stress triaxiality and Lode parameter in the unit-cell are $X_{\Sigma_{\gamma+\alpha'}} = 0.5$ and $L_{\gamma+\alpha'} = -1$, respectively. Comparison of Mori-Tanaka and Self-Consistent homogenization schemes. The unit-cell contains an austenite inclusion of 45% volume, which is modeled with Mori-Tanaka and Self-Consistent homogenization schemes, separately, while accounting for the martensitic transformation in a non-transforming austenite matrix. (a) Evolution of the normalized macroscopic effective stress $\bar{\Sigma}/\sigma_\gamma^{y0}$ with the macroscopic effective strain $\bar{\varepsilon}$. The red and green markers indicate the value of the macroscopic effective strain in the individual phases for a macroscopic effective strain in the bi-phase material of $\bar{\varepsilon}_{\gamma+\alpha'} = 0.4$. (b) Evolution of the macroscopic volume fraction of martensite $F_{\alpha'}$ (%) with the macroscopic effective strain in the bi-phase material $\bar{\varepsilon}_{\gamma+\alpha'}$. The yellow markers indicate the value of the macroscopic effective strain in the bi-phase material corresponding to the maximum difference in the martensite volume fraction between the Mori-Tanaka and Self-Consistent models (for this strain value, the contours and evolution of the microscopic volume fraction of martensite are shown in Figs. 17 and 18, respectively). The blue markers correspond to values of the macroscopic effective strain in the bi-phase material of 0.08 and 0.24 (for these strain values, the evolution of the microscopic volume fraction of martensite is also shown in Fig. 18). (For interpretation of the references to color in this figure legend, the reader is referred to the web version of this article.)

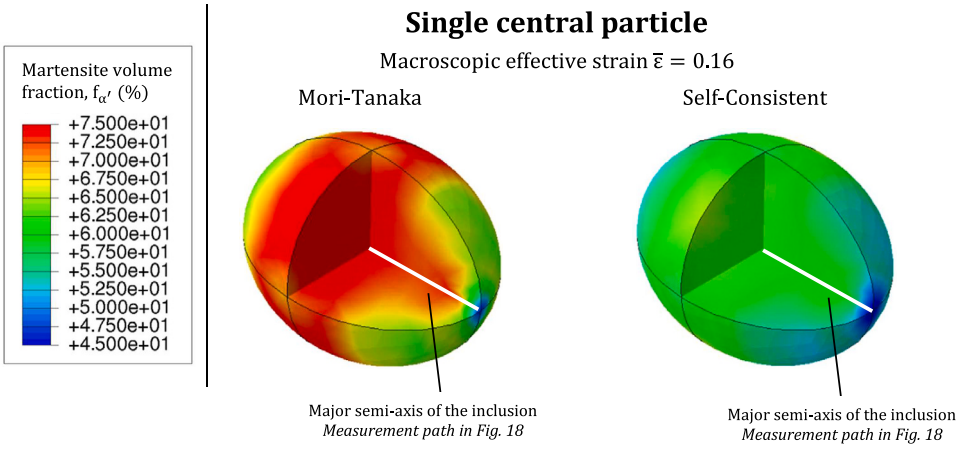

Fig. 17. Unit-cell finite element simulations. Monotonic loading. Material 304L and temperature $T = 77$ K. Contours of the microscopic volume fraction of martensite $f_{\alpha'}$ (%) for calculations corresponding to a single austenite inclusion of 45% volume, which is modeled with Mori-Tanaka and Self-Consistent homogenization schemes, separately, while accounting for the martensitic transformation in a fully non-evolving austenite matrix. The plots correspond to a macroscopic effective strain in the bi-phase material of $\bar{\varepsilon}_{\gamma+\alpha'} = 0.16$ and a macroscopic volume fraction of $F_{\alpha'} = 33\%$ and $F_{\alpha'} = 27\%$ for the Mori-Tanaka and Self-Consistent homogenization schemes, respectively (see the yellow marker in Fig. 16(b)). The white solid line included in the figure indicates the major semi-axis of the inclusion, which corresponds to the measurement path used in Fig. 18. (For interpretation of the references to color in this figure legend, the reader is referred to the web version of this article.).

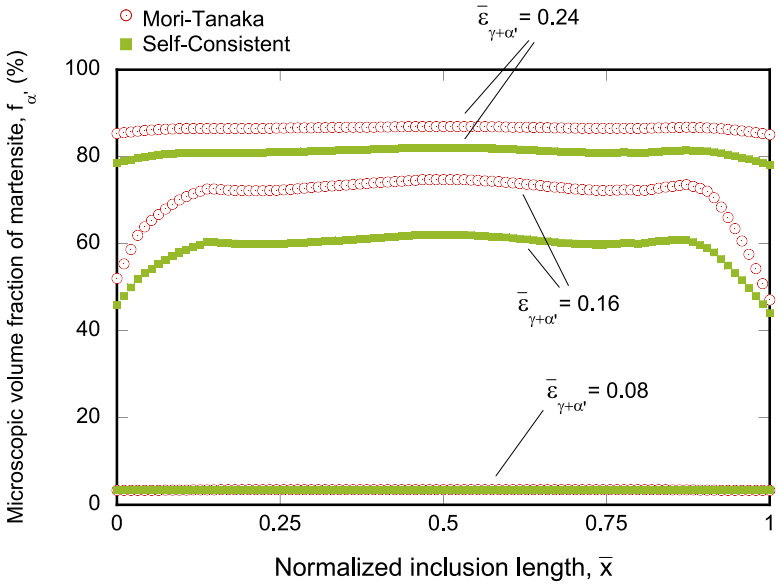

Fig. 18. Unit-cell finite element simulations. Monotonic loading. Material 304L and temperature $T = 77$ K. Comparison of Mori-Tanaka and Self-Consistent homogenization schemes. Calculations corresponding to a single austenite inclusion of 45% volume, which is modeled with Mori-Tanaka and Self-Consistent homogenization schemes, while accounting for the martensitic transformation in a fully non-evolving austenite matrix. Evolution of the microscopic volume fraction of martensite $f_{\alpha'}$ (%) along the normalized major semi-axis of the inclusion $\bar{x}$, see white solid line in Fig. 17. The data correspond to three values of the macroscopic effective strain in the bi-phase material of $\bar{\varepsilon}_{\gamma+\alpha'}$: 0.08, 0.16 and 0.24. The corresponding values of the macroscopic volume fraction are: $F_{\alpha'} = 1.5\%$, 33% and 40%, and $F_{\alpha'} = 1.5\%$, 27% and 37%, for the Mori-Tanaka and Self-Consistent homogenization schemes, respectively (see the yellow and blue markers in Fig. 16(b)). (For interpretation of the references to color in this figure legend, the reader is referred to the web version of this article.).

inclusion. Furthermore, there are no noticeable differences between the predictions obtained from both homogenization schemes. However, for $\bar{\varepsilon}_{\gamma+\alpha'} = 0.16$, the Mori-Tanaka scheme predicts $\approx 12\%$ more martensite than the Self-Consistent model (as mentioned above), and the volume fraction of martensite is greater in the central section of the inclusion, where larger plastic strains are attained. The lower transformation is located near the interface between inclusion and matrix (where the maximum plastic strain in the austenite matrix occurs, see Fig. 8 and the discussion therein). Similar qualitative results are obtained for $\bar{\varepsilon}_{\gamma+\alpha'} = 0.24$, but the martensite volume fraction predicted by both Mori-Tanaka and Self-Consistent schemes is greater, and the difference in the predictions between both homogenization schemes are smaller (5% more martensite predicted by the Mori-Tanaka model).

6.2. Tensile test calculations

The experimental results reported by Fernández-Pisón et al. (2021) for AISI 304L and AISI 316LN samples subjected to uniaxial tension are compared with numerical simulations performed with the finite element model presented in Section 5.2, in which the mechanical behavior of the bi-phase material is described with Mori-Tanaka and Self-Consistent homogenization schemes separately. Recall that the material parameters for both steel grades are included in Table 2. The comparison between experiments and finite elements is performed for the samples subjected to three different temperatures: $T = 300$ K (room temperature), 77 K, and 4 K. In the calculations, the temperature is assumed to be constant during the entire deformation process, and the material is considered to be initially fully austenitic, consistent with the microstructural observations of Fernández-Pisón et al. (2021).

Fig. 19 shows experimental data and finite element results for the evolution of the true stress σ and the volume fraction of martensite $f_{\alpha'}$ with the true strain ϵ in AISI 304L tensile samples. Note that true strain and true stress are computed in the same manner in the experiments and in the finite element simulations. On the one hand, $\epsilon = \ln(1+e)$, where $e = \frac{\Delta L}{L}$ is the nominal strain, with L being the initial gage length and ΔL the axial elongation of the gage length. On the other hand, $\sigma = \frac{F}{A}(1+e)$, where F is the axial force in the sample and A is the initial cross-section area in the gage region. The volume fraction of martensite is computed by averaging the martensite content in the gage, both in the experiments (for each measuring method, see Fernández-Pisón et al. (2021)) and in the finite element simulations. The data shown in the graphs correspond to strain values before the maximum axial force is reached. Moreover, note that at $T = 4$ K, the experiments showed discontinuous plastic flow (see Fernández-Pisón et al. (2021)), yet the constitutive model does not include features to describe this material instability, so the test data in Fig. 19(c) correspond to the upper envelop of the actual experimental results in order to facilitate the comparison with the simulations.

For $T = 300$ K, see Fig. 19(a), both homogenization schemes yield virtually the same results. Mori-Tanaka and Self-Consistent predictions find very good quantitative agreement with the experimental stress–strain characteristic and capture the quasi-linear increase of the volume fraction of martensite with the sample deformation. Just like in the experiments, the simulations predict the transformation to start at $\epsilon \approx 0.05$, such that the content of martensite reaches $\approx 5\%$ when $\epsilon \approx 0.4$. The quantitative differences between experiments and simulations for the volume fraction of martensite are due to the inherent scatter of the local experimental measurements (see Fernández-Pisón et al., 2021). The relatively low amount of austenite transformed into martensite causes the strain hardening of the material to be roughly linear (i.e., very similar to the strain hardening of the austenite phase).

For $T = 77$ K, see Fig. 19(b), the experimental $\sigma - \epsilon$ curve displays a sigmoidal shape—due to the increasing amount of austenite transformed into martensite—which is captured by both Mori-Tanaka and Self-Consistent models. Notice that both the scale of the abscissa and ordinate axis are different than in Fig. 19(a). The quantitative differences between measured and predicted stress–strain characteristics are mainly limited to a narrow range of intermediate strain values, $0.15 \leq \epsilon \leq 0.25$, for which the homogenization models overestimate the stress and strain hardening of the material. Notice that both Mori-Tanaka and Self-Consistent provide *fairly accurate* predictions for the strain at which transformation starts ($\epsilon \approx 0.05$), for the strain at which transformation ends ($\epsilon \approx 0.25$), and for the saturation value of martensite ($f_{\alpha'} \approx 85\%$). Indeed, the strain at which the transformation

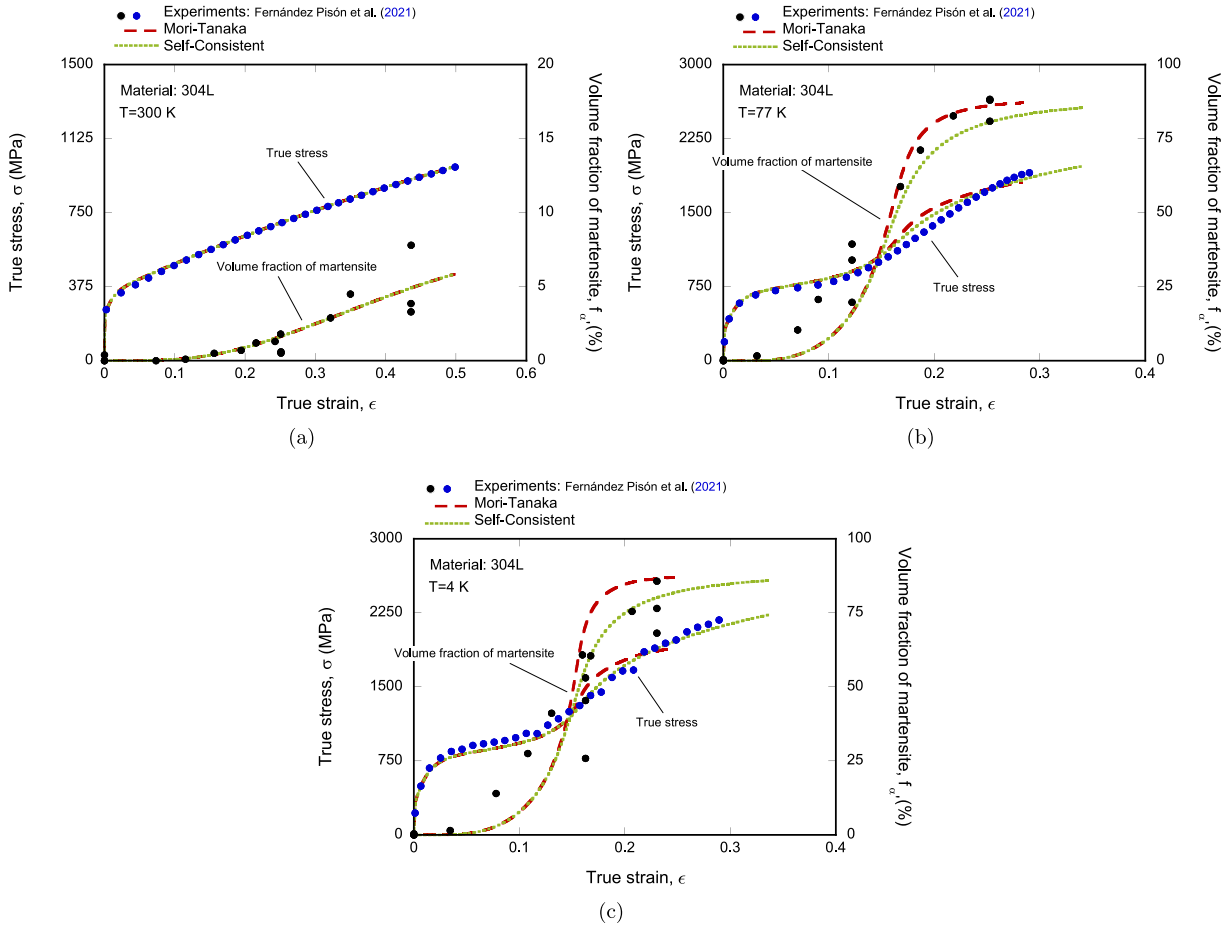

Fig. 19. Tensile test finite element simulations. Material 304L. Evolution of the true stress σ and the volume fraction of martensite $f_{\alpha'}$ versus the true strain ϵ for calculations performed with Mori-Tanaka and Self-Consistent homogenization schemes accounting for the martensitic transformation in an initial fully austenitic material. Comparison with the experimental results reported in Fernández-Pisón et al. (2021). Temperature: (a) $T = 300$ K, (b) $T = 77$ K, and (c) $T = 4$ K. (For interpretation of the references to color in this figure legend, the reader is referred to the web version of this article.)

begins and the saturation value of martensite are not influenced by the homogenization scheme but are determined by the Olson and Cohen (1975) law and the corresponding material parameters. On the other hand, the transformation rate obtained with the homogenization models for intermediate strains seems to be greater than in the experiments, especially for the Mori-Tanaka model, causing the overestimation of the stress and the strain hardening at intermediate values of strain.

For $T = 4$ K, see Fig. 19(c), the experimental results for the evolution of the true stress σ and the volume fraction of martensite $f_{\alpha'}$ are qualitatively very similar to the data obtained at 77 K. On the other hand, the flow strength of the material has increased with the decrease in testing temperature, most likely due to the temperature sensitivity of the individual phases rather than to the martensitic transformation, which occurs at a similar rate to that at 77 K. Both Mori-Tanaka and Self-Consistent models describe the sigmoidal strain hardening of the material and the boost of the flow stress with the temperature decrease. For instance, the homogenization models capture the increase in the initial yield stress of the material as the testing temperature decreases, which goes from 300 MPa to 350 MPa and 400 MPa (determined from the experimental curves as the 0.2% offset yield strength according to the standard ASTM-E8) at 300 K, 77 K, and 4 K, respectively. It shows the accurate calibration of the mechanical behavior of the austenite (at low strains $\epsilon \leq 0.1$, the microstructure of the material is largely austenite). Moreover, notice that at larger strains ($\epsilon \geq 0.15$), the predictions of the Self-Consistent scheme are closer to the experiments than the results obtained with the Mori-Tanaka model, just like it happened for 77 K, because the Self-Consistent scheme shows a lower transformation rate (Mori-Tanaka seems to overestimate the maximum transformation rate at intermediate strains).

Fig. 20 shows experimental data and finite element results for the evolution of the true stress and the volume fraction of martensite with the true strain in AISI 316LN tensile samples tested at 300 K, 77 K, and 4 K. The only difference with respect to the results shown in Fig. 19 is the steel grade investigated.

For $T = 300$ K, see Fig. 20(a), both homogenization models accurately predict the flow strength level and the quasi-linear hardening of the material, as well as the lack of martensitic transformation within the whole range of strains considered (recall that the data displayed in the graphs correspond to strain values prior to the maximum axial force being attained). Decreasing the testing temperature to 77 K makes the flow strength increase and promotes the transformation from austenite into martensite, Fig. 20(b). Notice that both the scale of the abscissa and ordinate axis are different than in Fig. 20(a). The strain hardening of the material is quasi-linear (as for 300 K), most likely because the mechanical behavior of austenite and martensite phases is more similar than in the case of AISI 304L, see Fig. C.22, and also because of the gradual transformation and relatively low volume fraction of transformed austenite (slower transformation and

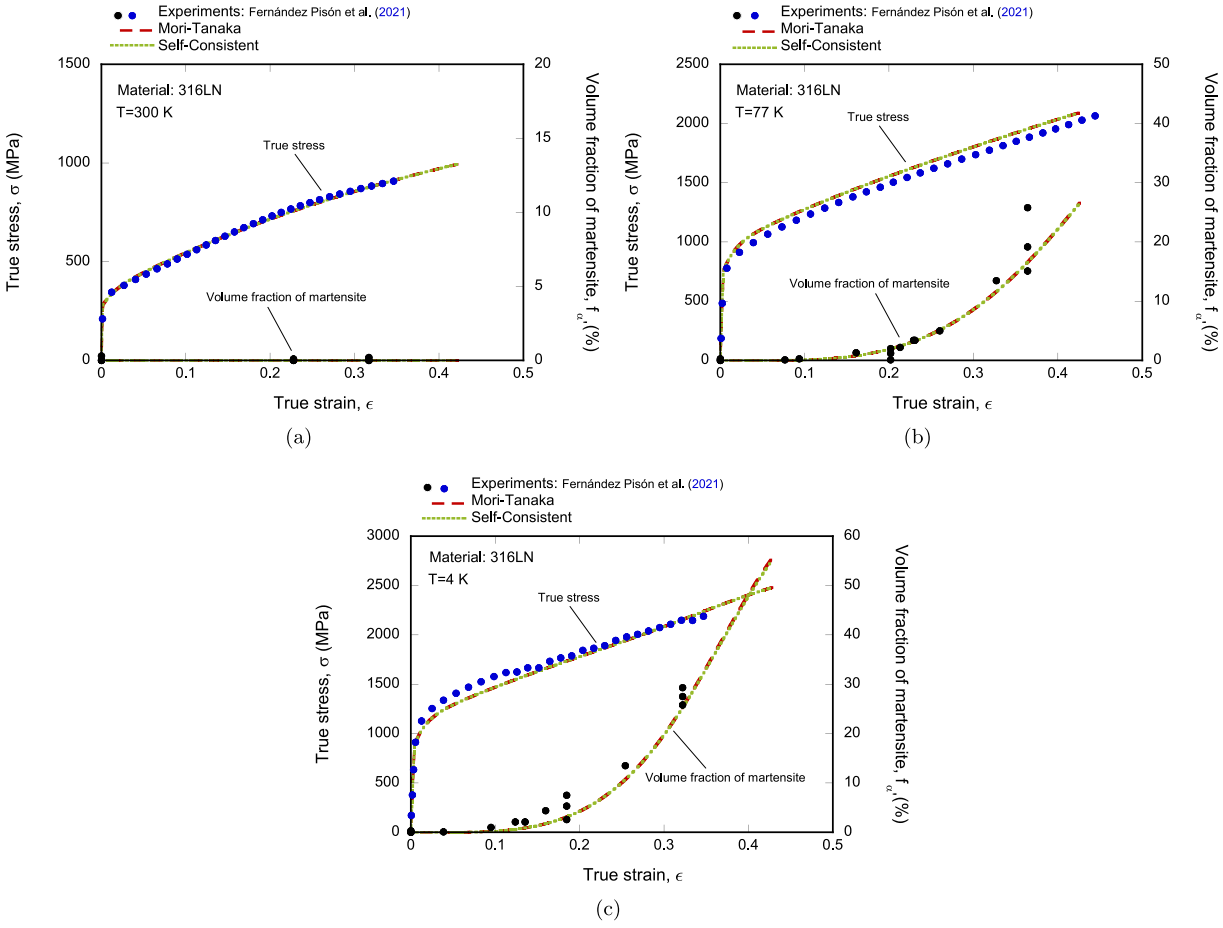

Fig. 20. Tensile test finite element simulations. Material 316LN. Evolution of the true stress σ and the volume fraction of martensite $f_{\alpha'}$ versus the true strain ϵ for calculations performed with Mori-Tanaka and Self-Consistent homogenization schemes accounting for the martensitic transformation in an initial fully austenitic material. Comparison with the experimental results reported in Fernández-Pisón et al. (2021). Temperature: (a) $T = 300$ K, (b) $T = 77$ K, and (c) $T = 4$ K. (For interpretation of the references to color in this figure legend, the reader is referred to the web version of this article.)

less content of martensite than in the case of AISI 304L at the same temperature of 77 K). The evolution of the volume fraction of martensite displays a concave-upward shape, reaching $f_{\alpha'} \approx 20\%$ for $\epsilon \approx 0.4$. Notice that the predictions of both homogenization schemes overlap and find very good qualitative and quantitative agreement with the experimental results. Similarly, both Mori-Tanaka and Self-Consistent yield virtually the same numerical results at 4 K, see Fig. 20(c), and predict the increase in the flow strength of the material and the greater transformation rate with the temperature decrease (recall that the test data included in the graph corresponds to the upper envelop of the flow stress, so it does not show the discontinuous plastic flow observed in the actual experimental results, see Fernández-Pisón et al., 2021). For instance, the simulations accurately predict that the initial yield stress of AISI 316LN increases as the testing temperature decreases, which goes from 750 MPa to 950 MPa (determined from the experimental curves as the 0.2% offset yield strength according to the standard ASTM-E8) at 77 K and 4 K, respectively. Besides, the simulations also capture the concave-upward shape of the evolution of the volume fraction of martensite with the strain in the sample, such that $f_{\alpha'} \approx 27\%$ for $\epsilon \approx 0.32$. Note that if the amount of transformed martensite is low, practically any homogenization model can generate results that replicate the material's effective behavior. Moreover, in such a case, one could even forget the homogenization approach and instead employ a conventional material model with a macroscopic yield function that does not consider the evolving material microstructure. However, in applications like high-field superconducting magnet systems, it is critical to ascertain whether the material undergoes martensitic transformation and consequently exhibits ferromagnetic properties. In such cases, it is encouraged to consider homogenization models that account for the phase transformation.

These results suggest that if the mechanical behavior of the phases is *similar* (as in the case of AISI 316LN, see the behavior of the individual phases in Fig. C.22), the differences in the predictions of Mori-Tanaka and Self-Consistent models are small, and both homogenization schemes accurately capture the effective mechanical behavior of the material and the rate of the martensitic transformation for a wide range of strains and testing temperatures, see Fig. 20. However, if the mechanical behavior of the phases is *rather* different (as in the case of AISI 304L, see the behavior of the individual phases for example in Fig. B.21), the differences in the predictions of Mori-Tanaka and Self-Consistent models become noticeable, and the Self-Consistent scheme

yields results closer to experiments for the effective behavior of the material and for the martensitic transformation rate at low temperatures and large strains (when the volume fraction of transformed martensite is large), see Fig. 19.

7. Summary and conclusions

In this paper, we have developed a homogenized constitutive model based on a Hill-type incremental formulation to capture the effective mechanical behavior and martensitic transformation of austenitic steels at cryogenic temperatures. Two different mean-field homogenization schemes have been used: the explicit Mori-Tanaka scheme, which assumes the austenite phase as the parent medium in which the martensite phase is embedded, and the implicit Self-Consistent scheme, which considers the homogenized material as the parent medium in which the austenite and martensite phases are embedded. The individual phases have been modeled with linear elasticity and von Mises plasticity. The evolution of the yield stress has been described with a rate-independent nonlinear mixed kinematic-isotropic hardening law, and the martensitic transformation has been modeled with the sigmoidal kinetic relationship proposed by Olson and Cohen (1975). A return mapping algorithm based on the implicit backward Euler integration scheme has been used to implement the constitutive model into ABAQUS/Standard through a UMAT user subroutine, for which a closed-form expression of the consistent Jacobian tensor has been derived. The UMAT code is included as *Supplementary Material*. Former tensile experiments performed at 300 K, 77 K, and 4 K have been used to identify the parameters describing the mechanical behavior of the individual phases and the kinetics of the martensitic transformation for AISI 304L and AISI 316LN steel grades. The Mori-Tanaka and Self-Consistent schemes integrated into the model have been evaluated with regard to their ability to describe the mechanical behavior of the bi-phase material by comparing the predictions of the homogenization schemes with unit-cell finite element calculations with an explicit description of the martensite inclusions and the austenite matrix. The comparison has been performed for different stress states with controlled triaxiality and Lode parameter under monotonic and cycling loading. Moreover, finite element simulations on tensile samples subjected to prescribed displacement at the three different constant temperatures (300 K, 77 K, and 4 K) have been compared with the experiments to validate the capability of the homogenized constitutive model to predict cryogenic martensitic transformation in austenitic stainless steels. The main conclusions drawn from this investigation are as follows:

- Mori-Tanaka and Self-Consistent models yield predictions for the effective behavior of the bi-phase material that find quantitative agreement with unit-cell calculations carried out with explicit description of the austenite matrix and the martensite inclusions under monotonic and cyclic loading.
- The partitioning of the strain between the two phases calculated with the homogenization schemes shows noticeable differences with the unit-cell simulations with explicit representation of the microstructure since both Self-Consistent and Mori-Tanaka underestimate the strain in the martensite and overestimate the strain in the austenite.
- The predictions of the Self-Consistent/Mori-Tanaka model for the strain in the phases in general find better/worse agreement with the calculations with explicit representation of the microstructure as the volume of martensite increases.
- The Self-Consistent model yields results for the hydrostatic stress in the bi-phase material and the individual phases that are very similar to the calculations with explicit description of the martensite particles, while the Mori-Tanaka model overestimates the hydrostatic stress in the martensite and underestimates the hydrostatic stress in the austenite and in the bi-phase material.
- Increasing differences in the mechanical behavior of the individual phases boosts the differences in the predictions of Mori-Tanaka and Self-Consistent models, such that the Self-Consistent scheme yields results closer to those of the unit-cell calculations and experiments for the effective behavior of the material and also for the martensitic transformation rate, specifically at large strains and low temperatures.
- The two homogenization schemes investigated accurately describe the quasi-linear strain hardening and temperature sensitivity of the flow strength of AISI 316LN, as well as the lack of martensitic transformation at 300 K and the concave-upward shape of the martensite content evolution at 77 K and 4 K.
- Mori-Tanaka and Self-Consistent yield virtually the same numerical results for the mechanical behavior of AISI 304L at 300 K and capture the quasi-linear increase of the volume fraction of martensite with the material straining.
- The differences in the results of the two homogenization schemes for the AISI 304L become noticeable at cryogenic temperatures since the transformation rate at intermediate strains predicted by the Mori-Tanaka model is greater than in the experiments, leading to an overestimation of the stress and the strain hardening of the material, while the Self-Consistent model captures accurately the sigmoidal shape of both strain hardening and martensite content evolution.

All in all, the key outcomes of this work are: (i) the validation of the homogenization schemes against finite element models that include a resolved description of the austenite–martensite microstructure for different stress states, and (ii) the suitability of the homogenized model to predict the mechanical behavior at large strains and high volume fractions of transformed martensite. The quantitative agreement of the homogenized model predictions with unit-cell finite element calculations and experimental data, notably in the case of the Self-Consistent scheme, validates the constitutive framework developed in this work. The homogenized model has been proven to be suitable for predicting the mechanical behavior and martensitic transformation of austenitic stainless steels under the wide range of temperatures of interest for superconducting magnet systems. Future work includes: (i) enhancing the model formulation to take into account the discontinuous plastic flow shown by AISI 304L and AISI 316LN at 4 K (Fernández-Pisón et al., 2021), (ii) capturing the strain rate sensitivity of the flow strength of the material (Tomita and Iwamoto, 1995; Papatriantafillou et al., 2006), and (iii) accounting for a rate of change of the probability of martensite nucleation as well as stress state (Stringfellow et al., 1992) and strain rate (Tomita and Iwamoto, 1995) sensitivities in the kinetics of the martensitic transformation.

CRediT authorship contribution statement

P. Fernández-Pisón: Conceptualization, Data curation, Formal analysis, Investigation, Methodology, Software, Validation, Writing – original draft, Writing – review & editing. **A.R. Vishnu:** Methodology, Software, Writing – review & editing. **G. Vadillo:** Conceptualization, Methodology, Software, Writing – review & editing. **J.A. Rodríguez-Martínez:** Conceptualization, Formal analysis, Funding acquisition, Investigation, Methodology, Project administration, Resources, Supervision, Validation, Writing – original draft, Writing – review & editing.

Declaration of competing interest

The authors declare that they have no known competing financial interests or personal relationships that could have appeared to influence the work reported in this paper.

Data availability

We have attached the link to the UMAT code at the Supplementary Data Section.

Acknowledgments

This work is dedicated to Alan Needleman for his outstanding contributions in the field of Mechanics of Materials. His unwavering passion and energy are an inspiration and example to all of us.

The authors would like to thank Prof. Ankit Srivastava (Texas A&M University, USA) and Prof. Katarzyna Kowalczyk-Gajewska (Institute of Fundamental Technological Research of Polish Academy of Sciences, Poland) for the fruitful discussions.

Funding

The research leading to these results has received funding from the European Union's Horizon2020 Programme (Excellent Science, Marie Skłodowska-Curie Actions) under REA grant agreement 777896 (Project QUANTIFY).

G. Vadillo acknowledges the financial support provided by the Spanish Ministry of Science and Innovation under the programme Proyectos I+D Excelencia 2017. Project APPLIED, DPI2017-88608-P.

Appendix A. Specifics of the numerical implementation

A.1. Numerical implementation of the individual phases

The numerical implementation is performed using a return mapping algorithm in which an implicit backward Euler integration scheme is employed (Safaei, 2013; Hosseini and Rodríguez-Martínez, 2021). The discretized constitutive equations are the following:

$$\boldsymbol{\epsilon}^{(n+1)} = \Delta\mathfrak{R}_{(n)}^{(n+1)}\boldsymbol{\epsilon}^{(n)}\Delta\mathfrak{R}_{(n)}^{(n+1)^{\mathrm{T}}} + \Delta\boldsymbol{\epsilon}^{(n+1)} \tag{A.1}$$

$$\boldsymbol{\epsilon}^{p(n+1)} = \Delta\mathfrak{R}_{(n)}^{(n+1)}\boldsymbol{\epsilon}^{p(n)}\Delta\mathfrak{R}_{(n)}^{(n+1)^{\mathrm{T}}} + \Delta\lambda^{(n+1)}\boldsymbol{N}^{(n+1)} \tag{A.2}$$

$$\begin{aligned}\boldsymbol{\sigma}^{(n+1)} &= \Delta\mathfrak{R}_{(n)}^{(n+1)}\boldsymbol{\sigma}^{(n)}\Delta\mathfrak{R}_{(n)}^{(n+1)^{\mathrm{T}}} + \boldsymbol{L}^{e} : \left(\Delta\boldsymbol{\epsilon}^{e(n+1)}\right)\\ &= \boldsymbol{\sigma}^{tr(n+1)} - \boldsymbol{L}^{e} : \left(\Delta\boldsymbol{\epsilon}^{p(n+1)}\right)\end{aligned} \tag{A.3}$$

$$\boldsymbol{X}_1^{(n+1)} = \Delta\mathfrak{R}_{(n)}^{(n+1)}\boldsymbol{X}_1^{(n)}\Delta\mathfrak{R}_{(n)}^{(n+1)^{\mathrm{T}}} + \Delta\lambda^{(n+1)}\boldsymbol{q}_{X_1}^{(n+1)} \tag{A.4}$$

$$\boldsymbol{X}_2^{(n+1)} = \Delta\mathfrak{R}_{(n)}^{(n+1)}\boldsymbol{X}_2^{(n)}\Delta\mathfrak{R}_{(n)}^{(n+1)^{\mathrm{T}}} + \Delta\lambda^{(n+1)}\boldsymbol{q}_{X_2}^{(n+1)} \tag{A.5}$$

$$R_1^{(n+1)} = (1-\beta)\frac{h_1}{\psi_1}\left(1 - e^{-\psi_1\left(\bar{\epsilon}^{p(n)} + \Delta\lambda^{(n+1)}\right)}\right) \tag{A.6}$$

$$R_2^{(n+1)} = (1-\beta)\frac{h_2}{\psi_2}\left(1 - e^{-\psi_2\left(\bar{\epsilon}^{p(n)} + \Delta\lambda^{(n+1)}\right)}\right) \tag{A.7}$$

$$F^{(n+1)} = J_2\left(\boldsymbol{\sigma}^{rel(n+1)}\right) - \left(\sigma^{y0} + R_1^{(n+1)} + R_2^{(n+1)}\right) \leq 0 \tag{A.8}$$

with $\boldsymbol{N}^{(n+1)} = \frac{3}{2}\frac{\boldsymbol{\sigma}^{rel(n+1)}}{J_2\left(\boldsymbol{\sigma}^{rel(n+1)}\right)}$, $\boldsymbol{q}_{X_1}^{(n+1)} = \beta h_1\frac{\boldsymbol{\sigma}^{rel(n+1)}}{J_2\left(\boldsymbol{\sigma}^{rel(n+1)}\right)} - \psi_1\boldsymbol{X}_1^{(n+1)}$, $\boldsymbol{q}_{X_2}^{(n+1)} = \beta h_2\frac{\boldsymbol{\sigma}^{rel(n+1)}}{J_2\left(\boldsymbol{\sigma}^{rel(n+1)}\right)} - \psi_2\boldsymbol{X}_2^{(n+1)}$, $J_2\left(\boldsymbol{\sigma}^{rel(n+1)}\right) = \sqrt{\frac{3}{2}\left(\boldsymbol{\sigma}^{rel(n+1)}\right) : \left(\boldsymbol{\sigma}^{rel(n+1)}\right)}$, and $\boldsymbol{\sigma}^{rel(n+1)} = \boldsymbol{s}^{(n+1)} - \boldsymbol{X}_1^{(n+1)} - \boldsymbol{X}_2^{(n+1)}$. Eq. (A.3) includes the trial stress $\boldsymbol{\sigma}^{tr(n+1)} = \Delta\mathfrak{R}_{(n)}^{(n+1)}\boldsymbol{\sigma}^{(n)}\Delta\mathfrak{R}_{(n)}^{(n+1)^{\mathrm{T}}} + \boldsymbol{L}^{e} : \Delta\boldsymbol{\epsilon}^{(n+1)}$, which is calculated during the elastic predictor step of the return mapping algorithm (Zaera and Fernández-Sáez, 2006), as well as the decomposition of the total strain increment into elastic and plastic components $\Delta\boldsymbol{\epsilon}^{(n+1)} = \Delta\boldsymbol{\epsilon}^{e(n+1)} + \Delta\boldsymbol{\epsilon}^{p(n+1)}$. Notice the update of the variables in the objective increments (term $\Delta\mathfrak{R}_{(n)}^{(n+1)}(\bullet)^{(n)}\Delta\mathfrak{R}_{(n)}^{(n+1)^{\mathrm{T}}}$), which accounts for the incremental rotation of the material basis. The predefined ABAQUS function *ROTSIG* can be used to compute this term (the incremental rotation $\Delta\mathfrak{R}_{(n)}^{(n+1)}$ is provided by the ABAQUS variable *DROT*).

The plastic multiplier increment is computed using an iterative Newton–Raphson procedure based on the linearization of the set of equations, assuming that the total strain and the values of the previous step (n) are constants. According to the Newton–Raphson procedure, the linearization of any equation such as $g(\Delta\lambda) = 0$ leads to $g_{(k+1)} = g_{(k)} + \left(\frac{dg}{d\Delta\lambda}\right)_{(k)}\delta\lambda_{(k)} = 0$ and subsequently $\delta\lambda_{(k)} = \frac{-g_{(k)}}{\left(\frac{dg}{d\Delta\lambda}\right)_{(k)}}$, where $\delta\lambda_{(k)}$ is the iterative change in $\Delta\lambda$ at the k-th iteration of the Newton–Raphson procedure (Eq. (A.24)). Thus, the updated expressions of Eqs. (A.2)–(A.5) and (A.8) can be cast into the following forms suitable for the Newton–Raphson iteration scheme:

$$\begin{aligned}\boldsymbol{g}_1^{(n+1)} &= -\boldsymbol{\epsilon}^{p(n+1)} + \Delta\mathfrak{R}_{(n)}^{(n+1)}\boldsymbol{\epsilon}^{p(n)}\Delta\mathfrak{R}_{(n)}^{(n+1)^{\mathrm{T}}} + \Delta\lambda^{(n+1)}\boldsymbol{N}^{(n+1)}\\ &= (\boldsymbol{L}^{e})^{-1} : \left(\boldsymbol{\sigma}^{(n+1)} - \boldsymbol{\sigma}^{tr(n+1)}\right) + \Delta\lambda^{(n+1)}\boldsymbol{N}^{(n+1)}\end{aligned} \tag{A.9}$$

$$\boldsymbol{g}_2^{(n+1)} = -\boldsymbol{X}_1^{(n+1)} + \Delta\mathfrak{R}_{(n)}^{(n+1)}\boldsymbol{X}_1^{(n)}\Delta\mathfrak{R}_{(n)}^{(n+1)^{\mathrm{T}}} + \Delta\lambda^{(n+1)}\boldsymbol{q}_{X_1}^{(n+1)} \tag{A.10}$$

$$\boldsymbol{g}_3^{(n+1)} = -\boldsymbol{X}_2^{(n+1)} + \Delta\mathfrak{R}_{(n)}^{(n+1)}\boldsymbol{X}_2^{(n)}\Delta\mathfrak{R}_{(n)}^{(n+1)^{\mathrm{T}}} + \Delta\lambda^{(n+1)}\boldsymbol{q}_{X_2}^{(n+1)} \tag{A.11}$$

$$F^{(n+1)} = J_2\left(\boldsymbol{\sigma}^{rel(n+1)}\right) - \left(\sigma^{y0} + R_1^{(n+1)} + R_2^{(n+1)}\right) \tag{A.12}$$

Note that Eqs. (A.6) and (A.7) are not included because they do not need to be linearized, Eq. (A.10) combines Eqs. (A.2) and (A.3), and Eqs. (A.12) is particularized for the case of plastic yielding ($F = 0$). Linearization of Eqs. (A.10)–(A.12) gives:

$$\boldsymbol{g}_{1(k)}^{(n+1)} + (\boldsymbol{L}^{e})^{-1} : \left(\frac{d\boldsymbol{\sigma}}{d\Delta\lambda}\right)_{(k)}^{(n+1)}\delta\lambda_{(k)}^{(n+1)} + \Delta\lambda_{(k)}^{(n+1)}\left(\frac{d\boldsymbol{N}}{d\Delta\lambda}\right)_{(k)}^{(n+1)}\delta\lambda_{(k)}^{(n+1)} + \delta\lambda_{(k)}^{(n+1)}\boldsymbol{N}_{(k)}^{(n+1)} = 0 \tag{A.13}$$

$$\boldsymbol{g}_{2(k)}^{(n+1)} - \left(\frac{d\boldsymbol{X}_1}{d\Delta\lambda}\right)_{(k)}^{(n+1)}\delta\lambda_{(k)}^{(n+1)} + \Delta\lambda_{(k)}^{(n+1)}\left(\frac{d\boldsymbol{q}_{X_1}}{d\Delta\lambda}\right)_{(k)}^{(n+1)}\delta\lambda_{(k)}^{(n+1)} + \delta\lambda_{(k)}^{(n+1)}\boldsymbol{q}_{X_1(k)}^{(n+1)} = 0 \tag{A.14}$$

$$\boldsymbol{g}_{3(k)}^{(n+1)} - \left(\frac{d\boldsymbol{X}_2}{d\Delta\lambda}\right)_{(k)}^{(n+1)}\delta\lambda_{(k)}^{(n+1)} + \Delta\lambda_{(k)}^{(n+1)}\left(\frac{d\boldsymbol{q}_{X_2}}{d\Delta\lambda}\right)_{(k)}^{(n+1)}\delta\lambda_{(k)}^{(n+1)} + \delta\lambda_{(k)}^{(n+1)}\boldsymbol{q}_{X_2(k)}^{(n+1)} = 0 \tag{A.15}$$

$$\begin{aligned}F_{(k)}^{(n+1)} &+ \left(\frac{dF}{d\boldsymbol{\sigma}} : \frac{d\boldsymbol{\sigma}}{d\Delta\lambda}\right)_{(k)}^{(n+1)}\delta\lambda_{(k)}^{(n+1)} + \left(\frac{dF}{d\boldsymbol{X}_1} : \frac{d\boldsymbol{X}_1}{d\Delta\lambda}\right)_{(k)}^{(n+1)}\delta\lambda_{(k)}^{(n+1)}\\ &+ \left(\frac{dF}{d\boldsymbol{X}_2} : \frac{d\boldsymbol{X}_2}{d\Delta\lambda}\right)_{(k)}^{(n+1)}\delta\lambda_{(k)}^{(n+1)}\\ &+ \left(\frac{dF}{dR_1}\frac{dR_1}{d\Delta\lambda}\right)_{(k)}^{(n+1)}\delta\lambda_{(k)}^{(n+1)} + \left(\frac{dF}{dR_2}\frac{dR_2}{d\Delta\lambda}\right)_{(k)}^{(n+1)}\delta\lambda_{(k)}^{(n+1)} = 0\end{aligned} \tag{A.16}$$

where all the derivatives can be expressed as a function of $\left(\frac{d\boldsymbol{\sigma}}{d\Delta\lambda}\right)_{(k)}^{(n+1)}$, $\left(\frac{d\boldsymbol{X}_1}{d\Delta\lambda}\right)_{(k)}^{(n+1)}$, $\left(\frac{d\boldsymbol{X}_2}{d\Delta\lambda}\right)_{(k)}^{(n+1)}$, $\left(\frac{dR_1}{d\Delta\lambda}\right)_{(k)}^{(n+1)}$, and $\left(\frac{dR_2}{d\Delta\lambda}\right)_{(k)}^{(n+1)}$, such that the linearized Eqs. (A.13)–(A.15) can be written in matrix form as follows:

$$\mathbb{G}_{(k)}^{(n+1)} + \left(\mathbb{E}_{(k)}^{(n+1)}\right)^{-1}\Delta\mathbb{K}_{(k)}^{(n+1)} + \delta\lambda_{(k)}^{(n+1)}\mathbb{B}_{(k)}^{(n+1)} = \mathbb{O} \tag{A.17}$$

with:

$$\mathbb{G}_{(k)}^{(n+1)} = \begin{Bmatrix}\left[\boldsymbol{g}_{1(k)}^{(n+1)}\right]\\ \left[\boldsymbol{g}_{2(k)}^{(n+1)}\right]\\ \left[\boldsymbol{g}_{3(k)}^{(n+1)}\right]\end{Bmatrix} \qquad \Delta\mathbb{K}_{(k)}^{(n+1)} = \begin{Bmatrix}\left[\left(\frac{d\boldsymbol{\sigma}}{d\Delta\lambda}\right)_{(k)}^{(n+1)}\right]\\ \left[\left(\frac{d\boldsymbol{X}_1}{d\Delta\lambda}\right)_{(k)}^{(n+1)}\right]\\ \left[\left(\frac{d\boldsymbol{X}_2}{d\Delta\lambda}\right)_{(k)}^{(n+1)}\right]\end{Bmatrix}\delta\lambda_{(k)}^{(n+1)}$$

$$\mathbb{B}_{(k)}^{(n+1)} = \begin{Bmatrix}\left[\boldsymbol{N}_{(k)}^{(n+1)}\right]\\ \left[\boldsymbol{q}_{X_1(k)}^{(n+1)}\right]\\ \left[\boldsymbol{q}_{X_2(k)}^{(n+1)}\right]\end{Bmatrix} \qquad \mathbb{O} = \begin{Bmatrix}[\boldsymbol{0}]\\ [\boldsymbol{0}]\\ [\boldsymbol{0}]\end{Bmatrix} \tag{A.18}$$

$$\left(\mathbb{E}_{(k)}^{(n+1)}\right)^{-1}=\begin{Bmatrix}\left[\boldsymbol{L}^{e}\right]^{-1}+\Delta\lambda_{(k)}^{(n+1)}\left[\left(\frac{d\boldsymbol{N}}{d\boldsymbol{\sigma}}\right)_{(k)}^{(n+1)}\right] & -\Delta\lambda_{(k)}^{(n+1)}\left[\left(\frac{d\boldsymbol{N}}{d\boldsymbol{\sigma}}\right)_{(k)}^{(n+1)}\right] & -\Delta\lambda_{(k)}^{(n+1)}\left[\left(\frac{d\boldsymbol{N}}{d\boldsymbol{\sigma}}\right)_{(k)}^{(n+1)}\right]\\ \Delta\lambda_{(k)}^{(n+1)}\left[\left(\frac{d\boldsymbol{q}_{X_1}}{d\boldsymbol{\sigma}}\right)_{(k)}^{(n+1)}\right] & -\Delta\lambda_{(k)}^{(n+1)}\left[\left(\left(\frac{d\boldsymbol{q}_{X_1}}{d\boldsymbol{\sigma}}\right)_{(k)}^{(n+1)}+\psi_1\boldsymbol{I}\right)-\boldsymbol{I}\right] & -\Delta\lambda_{(k)}^{(n+1)}\left[\left(\frac{d\boldsymbol{q}_{X_1}}{d\boldsymbol{\sigma}}\right)_{(k)}^{(n+1)}\right]\\ \Delta\lambda_{(k)}^{(n+1)}\frac{h_2}{h_1}\left[\left(\frac{d\boldsymbol{q}_{X_1}}{d\boldsymbol{\sigma}}\right)_{(k)}^{(n+1)}\right] & -\Delta\lambda_{(k)}^{(n+1)}\frac{h_2}{h_1}\left[\left(\frac{d\boldsymbol{q}_{X_1}}{d\boldsymbol{\sigma}}\right)_{(k)}^{(n+1)}\right] & -\Delta\lambda_{(k)}^{(n+1)}\left[\left(\frac{h_2}{h_1}\left(\frac{d\boldsymbol{q}_{X_1}}{d\boldsymbol{\sigma}}\right)_{(k)}^{(n+1)}+\psi_2\boldsymbol{I}\right)-\boldsymbol{I}\right]\end{Bmatrix} \tag{A.19}$$

Box I.

and $\left(\mathbb{E}_{(k)}^{(n+1)}\right)^{-1}$ is given in Box I (Eq. (A.19)). Note that $[(\bullet)]$ denotes the 6×1 or 6×6 matrix which corresponds to the symmetric second-order or fourth-order tensor, respectively (see Eqs. (C.1) and (C.5) in Doghri (2000)); and $[\mathbf{0}]$ is a 6×1 null matrix. Therefore, $\mathbb{G}_{(k)}^{(n+1)}$, $\Delta\mathbb{K}_{(k)}^{(n+1)}$, $\mathbb{B}_{(k)}^{(n+1)}$, and $\mathbb{O}$ are 18×1 matrices, and $\mathbb{E}_{(k)}^{(n+1)}$ is a 18×18 matrix.

The linearized Eq. (A.16) can also be written in matrix form as:

$$F_{(k)}^{(n+1)}+\left(\Delta\mathbb{F}_{(k)}^{(n+1)}\right)^{T}\Delta\mathbb{K}_{(k)}^{(n+1)}-\left(\frac{dR_1}{d\Delta\lambda}\right)_{(k)}^{(n+1)}\delta\lambda_{(k)}^{(n+1)}-\left(\frac{dR_2}{d\Delta\lambda}\right)_{(k)}^{(n+1)}\delta\lambda_{(k)}^{(n+1)}=0 \tag{A.20}$$

where the 18×1 matrix $\Delta\mathbb{F}_{(k)}^{(n+1)}$ is defined as:

$$\Delta\mathbb{F}_{(k)}^{(n+1)}=\begin{Bmatrix}\left[\left(\frac{dF}{d\boldsymbol{\sigma}}\right)_{(k)}^{(n+1)}\right]\\ \left[\left(\frac{dF}{d\boldsymbol{X}_1}\right)_{(k)}^{(n+1)}\right]\\ \left[\left(\frac{dF}{d\boldsymbol{X}_2}\right)_{(k)}^{(n+1)}\right]\end{Bmatrix}=\begin{Bmatrix}\left[\boldsymbol{N}_{(k)}^{(n+1)}\right]\\ -\left[\boldsymbol{N}_{(k)}^{(n+1)}\right]\\ -\left[\boldsymbol{N}_{(k)}^{(n+1)}\right]\end{Bmatrix} \tag{A.21}$$

Substituting Eq. (A.17) into Eq. (A.20) results in:

$$F_{(k)}^{(n+1)}-\left(\Delta\mathbb{F}_{(k)}^{(n+1)}\right)^{T}\mathbb{E}_{(k)}^{(n+1)}\mathbb{G}_{(k)}^{(n+1)}-\delta\lambda_{(k)}^{(n+1)}\left(\left(\Delta\mathbb{F}_{(k)}^{(n+1)}\right)^{T}\mathbb{E}_{(k)}^{(n+1)}\mathbb{B}_{(k)}^{(n+1)}\right)-\delta\lambda_{(k)}^{(n+1)}\left(\left(\frac{dR_1}{d\Delta\lambda}\right)_{(k)}^{(n+1)}+\left(\frac{dR_2}{d\Delta\lambda}\right)_{(k)}^{(n+1)}\right)=0 \tag{A.22}$$

from which $\delta\lambda_{(k)}^{(n+1)}$ is computed:

$$\delta\lambda_{(k)}^{(n+1)}=\frac{F_{(k)}^{(n+1)}-\left(\Delta\mathbb{F}_{(k)}^{(n+1)}\right)^{T}\mathbb{E}_{(k)}^{(n+1)}\mathbb{G}_{(k)}^{(n+1)}}{\left(\Delta\mathbb{F}_{(k)}^{(n+1)}\right)^{T}\mathbb{E}_{(k)}^{(n+1)}\mathbb{B}_{(k)}^{(n+1)}+\left(\left(\frac{dR_1}{d\Delta\lambda}\right)_{(k)}^{(n+1)}+\left(\frac{dR_2}{d\Delta\lambda}\right)_{(k)}^{(n+1)}\right)} \tag{A.23}$$

which allows us to determine the plastic multiplier increment:

$$\Delta\lambda_{(k+1)}^{(n+1)}=\Delta\lambda_{(k)}^{(n+1)}+\delta\lambda_{(k)}^{(n+1)} \tag{A.24}$$

which is used for the subsequent update of all the variables. Note that $R_{1(k+1)}^{(n+1)}$ and $R_{2(k+1)}^{(n+1)}$ are updated directly using Eqs. (A.6) and (A.7), respectively. The rest of the variables are updated using $(\bullet)_{(k+1)}^{(n+1)}=(\bullet)_{(k)}^{(n+1)}+\left(\frac{d(\bullet)}{d\Delta\lambda}\right)_{(k)}^{(n+1)}\delta\lambda_{(k)}^{(n+1)}$, where $\left(\frac{d\boldsymbol{\epsilon}^{p}}{d\Delta\lambda}\right)_{(k)}^{(n+1)}=(\boldsymbol{L}^{e})^{-1}\left(\frac{d\boldsymbol{\sigma}}{d\Delta\lambda}\right)_{(k)}^{(n+1)}$ and $\left(\frac{d\boldsymbol{X}_1}{d\Delta\lambda}\right)_{(k)}^{(n+1)}$, $\left(\frac{d\boldsymbol{X}_2}{d\Delta\lambda}\right)_{(k)}^{(n+1)}$, and $\left(\frac{d\boldsymbol{\sigma}}{d\Delta\lambda}\right)_{(k)}^{(n+1)}$ are obtained by solving $\Delta\mathbb{K}_{(k)}^{(n+1)}$ from Eqs. (A.17). The iterative Newton–Raphson method continues until convergence is obtained within an acceptably small tolerance: $\boldsymbol{g}_{1(k+1)}^{(n+1)}\approx\mathbf{0}$, $\boldsymbol{g}_{2(k+1)}^{(n+1)}\approx\mathbf{0}$, $\boldsymbol{g}_{3(k+1)}^{(n+1)}\approx\mathbf{0}$, and $F_{(k+1)}^{(n+1)}\approx0$ (see Eqs. (A.10)–(A.12)). Note that if the material behaves elastically during the loading step, then $F^{(n+1)}<0$ and $\Delta\lambda^{(n+1)}=0$.

Additionally, for the implementation of the homogenization procedure, it is necessary to compute the instantaneous algorithmic tangent operator $\boldsymbol{L}^{tan}=\frac{d(\Delta\boldsymbol{\sigma})}{d(\Delta\boldsymbol{\epsilon})}$ (as defined in Doghri and Ouaar (2003)). For that purpose, the discretized constitutive Eqs. (A.2)–(A.8) are differentiated with respect to all the variables at t^{n+1}, assuming the values of the previous step (n) as constant but the total strain as non-constant:

$$d\left(\Delta\boldsymbol{\epsilon}^{p(n+1)}\right)=d\left(\Delta\lambda^{(n+1)}\right)\boldsymbol{N}^{(n+1)}+\Delta\lambda^{(n+1)}d\boldsymbol{N}^{(n+1)} \tag{A.25}$$

$$\begin{aligned}\left(\Delta\boldsymbol{\sigma}^{(n+1)}\right)&=\boldsymbol{L}^{e}:d\left(\Delta\boldsymbol{\epsilon}^{e(n+1)}\right)\\&=\boldsymbol{L}^{e}:\left(d\left(\Delta\boldsymbol{\epsilon}^{(n+1)}\right)-d\left(\Delta\boldsymbol{\epsilon}^{p(n+1)}\right)\right)\end{aligned} \tag{A.26}$$

$$d\left(\Delta\boldsymbol{X}_1^{(n+1)}\right)=d\left(\Delta\lambda^{(n+1)}\right)\boldsymbol{q}_{X_1}^{(n+1)}+\Delta\lambda^{(n+1)}d\boldsymbol{q}_{X_1}^{(n+1)} \tag{A.27}$$

$$d\left(\Delta\boldsymbol{X}_2^{(n+1)}\right)=d\left(\Delta\lambda^{(n+1)}\right)\boldsymbol{q}_{X_2}^{(n+1)}+\Delta\lambda^{(n+1)}d\boldsymbol{q}_{X_2}^{(n+1)} \tag{A.28}$$

$$d\left(\Delta R_1^{(n+1)}\right)=\left(\frac{dR_1}{d\Delta\lambda}\right)^{(n+1)}d\left(\Delta\lambda^{(n+1)}\right) \tag{A.29}$$

$$d\left(\Delta R_2^{(n+1)}\right)=\left(\frac{dR_2}{d\Delta\lambda}\right)^{(n+1)}d\left(\Delta\lambda^{(n+1)}\right) \tag{A.30}$$

$$\begin{aligned}&\left(\frac{dF}{d\boldsymbol{\sigma}}:\frac{d\boldsymbol{\sigma}}{d\left(\Delta\boldsymbol{\sigma}\right)}\right)^{(n+1)}:d\left(\Delta\boldsymbol{\sigma}^{(n+1)}\right)\\&+\left(\frac{dF}{d\boldsymbol{X}_1}:\frac{d\boldsymbol{X}_1}{d\left(\Delta\boldsymbol{X}_1\right)}\right)^{(n+1)}:d\left(\Delta\boldsymbol{X}_1^{(n+1)}\right)\\&+\left(\frac{dF}{d\boldsymbol{X}_2}:\frac{d\boldsymbol{X}_2}{d\left(\Delta\boldsymbol{X}_2\right)}\right)^{(n+1)}:d\left(\Delta\boldsymbol{X}_2^{(n+1)}\right)\\&+\left(\frac{dF}{dR_1}\frac{dR_1}{d\Delta R_1}\right)^{(n+1)}d\left(\Delta R_1^{(n+1)}\right)+\left(\frac{dF}{dR_2}\frac{dR_2}{d\Delta R_2}\right)^{(n+1)}d\left(\Delta R_2^{(n+1)}\right)=0\end{aligned} \tag{A.31}$$

where Eq. (A.31) is particularized for the case of plastic flow ($F^{(n+1)}=0$).

Eqs. (A.25)–(A.28) and (A.31) are rearranged similarly to (A.10)–(A.12) (note that Eqs. (A.29) and (A.30) do not need to be linearized). Expressions (A.25)–(A.28) are then rewritten as:

$$-d\left(\Delta\boldsymbol{\epsilon}^{(n+1)}\right)+(\boldsymbol{L}^{e})^{-1}:\left(\Delta\boldsymbol{\sigma}^{(n+1)}\right)+d\left(\Delta\lambda^{(n+1)}\right)\boldsymbol{N}^{(n+1)}+\Delta\lambda^{(n+1)}d\boldsymbol{N}^{(n+1)}=0 \tag{A.32}$$

$$-d\left(\Delta\boldsymbol{X}_1^{(n+1)}\right)+d\left(\Delta\lambda^{(n+1)}\right)\boldsymbol{q}_{X_1}^{(n+1)}+\Delta\lambda^{(n+1)}d\boldsymbol{q}_{X_1}^{(n+1)}=0 \tag{A.33}$$

$$-d\left(\Delta\boldsymbol{X}_2^{(n+1)}\right)+d\left(\Delta\lambda^{(n+1)}\right)\boldsymbol{q}_{X_2}^{(n+1)}+\Delta\lambda^{(n+1)}d\boldsymbol{q}_{X_2}^{(n+1)}=0 \tag{A.34}$$

where Eq. (A.32) results from combining Eqs. (A.25) and (A.26). This set of Eqs. (A.32)–(A.34) is expressed in matrix form as follows:

$$-\mathbb{G}^{*(n+1)}+\left(\mathbb{E}^{(n+1)}\right)^{-1}\Delta\mathbb{K}^{*(n+1)}+d\left(\Delta\lambda^{(n+1)}\right)\mathbb{B}^{(n+1)}=\mathbb{O} \tag{A.35}$$

where $\mathbb{B}^{(n+1)}$, $\mathbb{O}$, and $\mathbb{E}^{(n+1)}$ are defined in Eqs. $(A.18)_3$, $(A.18)_4$, and (A.19), respectively (the subscript (k) should be omitted), while $\mathbb{G}^{*(n+1)}$ and $\Delta\mathbb{K}^{*(n+1)}$ are defined as:

$$\mathbb{G}^{*(n+1)}=\begin{Bmatrix}\left[d\left(\Delta\boldsymbol{\epsilon}^{(n+1)}\right)\right]\\ [\mathbf{0}]\\ [\mathbf{0}]\end{Bmatrix}\qquad\Delta\mathbb{K}^{*(n+1)}=\begin{Bmatrix}\left[d\left(\Delta\boldsymbol{\sigma}^{(n+1)}\right)\right]\\ \left[d\left(\Delta\boldsymbol{X}_1^{(n+1)}\right)\right]\\ \left[d\left(\Delta\boldsymbol{X}_2^{(n+1)}\right)\right]\end{Bmatrix} \tag{A.36}$$

Moreover, Eq. (A.31) can also be rewritten using the matrix formulation:

$$\left(\boldsymbol{\Delta\mathbb{F}}^{(n+1)}\right)^T \boldsymbol{\Delta\mathbb{K}}^{*(n+1)} - d\left(\Delta R_1^{(n+1)}\right) - d\left(\Delta R_2^{(n+1)}\right) = 0 \tag{A.37}$$

where $\boldsymbol{\Delta\mathbb{F}}^{(n+1)}$ is defined in Eq. (A.21) (the subscript (k) should be omitted).

Subsequently, inserting Eq. (A.35) and Eqs. (A.29)–(A.30) into Eq. (A.37) leads to:

$$d\left(\Delta\lambda^{(n+1)}\right) = \frac{\left(\boldsymbol{\Delta\mathbb{F}}^{(n+1)}\right)^T \mathbb{E}^{(n+1)}\mathbb{G}^{*(n+1)}}{\left(\boldsymbol{\Delta\mathbb{F}}^{(n+1)}\right)^T \mathbb{E}^{(n+1)}\mathbb{B}^{(n+1)} + \left(\left(\frac{dR_1}{d\Delta\lambda}\right)^{(n+1)} + \left(\frac{dR_2}{d\Delta\lambda}\right)^{(n+1)}\right)} \tag{A.38}$$

and inserting Eq. (A.38) into (A.35) results in:

$$\boldsymbol{\Delta\mathbb{K}}^{*(n+1)} = \mathbb{E}^{(n+1)}\mathbb{G}^{*(n+1)} - \frac{\mathbb{E}^{(n+1)}\mathbb{B}^{(n+1)}\left(\boldsymbol{\Delta\mathbb{F}}^{(n+1)}\right)^T \mathbb{E}^{(n+1)}\mathbb{G}^{*(n+1)}}{\left(\boldsymbol{\Delta\mathbb{F}}^{(n+1)}\right)^T \mathbb{E}^{(n+1)}\mathbb{B}^{(n+1)} + \left(\left(\frac{dR_1}{d\Delta\lambda}\right)^{(n+1)} + \left(\frac{dR_2}{d\Delta\lambda}\right)^{(n+1)}\right)} \tag{A.39}$$

from which the 18×18 matrix $\mathbb{L}^{(n+1)}$ can be defined:

$$\mathbb{L}^{(n+1)} = \mathbb{E}^{(n+1)} - \frac{\mathbb{E}^{(n+1)}\mathbb{B}^{(n+1)}\left(\boldsymbol{\Delta\mathbb{F}}^{(n+1)}\right)^T \mathbb{E}^{(n+1)}}{\left(\boldsymbol{\Delta\mathbb{F}}^{(n+1)}\right)^T \mathbb{E}^{(n+1)}\mathbb{B}^{(n+1)} + \left(\left(\frac{dR_1}{d\Delta\lambda}\right)^{(n+1)} + \left(\frac{dR_2}{d\Delta\lambda}\right)^{(n+1)}\right)} \tag{A.40}$$

so that $\boldsymbol{\Delta\mathbb{K}}^{*(n+1)} = \mathbb{L}^{(n+1)}\mathbb{G}^{*(n+1)}$, which, using the definitions of $\mathbb{G}^{*(n+1)}$ and $\boldsymbol{\Delta\mathbb{K}}^{*(n+1)}$ shown in Eq. (A.36), leads to:

$$\begin{Bmatrix} \left[d\left(\Delta\boldsymbol{\sigma}^{(n+1)}\right)\right] \\ \left[d\left(\Delta\boldsymbol{X}_1^{(n+1)}\right)\right] \\ \left[d\left(\Delta\boldsymbol{X}_2^{(n+1)}\right)\right] \end{Bmatrix} = \begin{bmatrix} \mathbb{L}_{11}^{(n+1)} & \mathbb{L}_{12}^{(n+1)} & \mathbb{L}_{13}^{(n+1)} \\ \mathbb{L}_{21}^{(n+1)} & \mathbb{L}_{22}^{(n+1)} & \mathbb{L}_{23}^{(n+1)} \\ \mathbb{L}_{31}^{(n+1)} & \mathbb{L}_{32}^{(n+1)} & \mathbb{L}_{33}^{(n+1)} \end{bmatrix} \begin{Bmatrix} \left[d\left(\Delta\boldsymbol{\epsilon}^{(n+1)}\right)\right] \\ [\mathbf{0}] \\ [\mathbf{0}] \end{Bmatrix} \tag{A.41}$$

where each component $\mathbb{L}_{ij}^{(n+1)}$ is a 6×6 matrix (with i and j ranging between 1 and 3). The component $\mathbb{L}_{11}^{(n+1)}$ is particularly interesting since $\left[d\left(\Delta\boldsymbol{\sigma}^{(n+1)}\right)\right] = \mathbb{L}_{11}^{(n+1)}\left[d\left(\Delta\boldsymbol{\epsilon}^{(n+1)}\right)\right]$, so that it corresponds to the 6×6 matrix format of the instantaneous algorithmic tangent operator:

$$\left[\boldsymbol{L}^{tan(n+1)}\right] = \mathbb{L}_{11}^{(n+1)} \tag{A.42}$$

which can be easily converted to its original format as a symmetric fourth-order tensor (see Eq. (C.5) in Doghri (2000)).

A generalized variable-point rule $(\bullet)^{(n+\Lambda)} = (1-\Lambda)(\bullet)^{(n)} + \Lambda(\bullet)^{(n+1)}$ is used for the numerical implementation of the instantaneous algorithmic tangent operator, where explicit and implicit integrations correspond to $\Lambda = 0$ and $\Lambda > 0$, respectively, with special cases: $\Lambda = 1$ (backward Euler) and $\Lambda = 1/2$ (mid-point rule). In this work, the value of Λ is determined as the one providing the least difference between the increment of stress calculated using the implicit backward Euler integration scheme (after convergence) and the one resulting from the relationship:

$$\Delta\boldsymbol{\sigma}^{(n+1)} = \boldsymbol{L}^{tan(n+\Lambda)} : \Delta\boldsymbol{\epsilon}^{(n+1)} \tag{A.43}$$

which is the numerical implementation of Eq. (8). In order to apply the generalized variable-point rule, the algorithmic tangent operator of the previous step $\boldsymbol{L}^{tan(n)}$ has to be rotated to the current configuration. The generalized variable-point rule can be written in the following 6×6 matrix format:

$$\left[\boldsymbol{L}^{tan(n+\Lambda)}\right] = (1-\Lambda)\left[Q\left(\Delta\mathfrak{R}_{(n)}^{(n+1)}\right)\right]\left[\boldsymbol{L}^{tan(n)}\right]\left[Q\left(\Delta\mathfrak{R}_{(n)}^{(n+1)^{\mathrm{T}}}\right)\right] + \Lambda\left[\boldsymbol{L}^{tan(n+1)}\right] \tag{A.44}$$

where $[Q(\bullet)]$ is a 6×6 matrix that allows to express operations with non-symmetric tensors (such as $\Delta\mathfrak{R}_{(n)}^{(n+1)}$) using a 6×6 matrix format, see Eqs. (C.22) and (C.29) in Doghri (2000). Note that, if for the considered time step the material behaves elastically, the instantaneous algorithmic tangent operator corresponds to the elastic stiffness tensor $\boldsymbol{L}^e$.

A.2. Numerical implementation of kinetics of the martensitic transformation

The implementation of the kinetics of martensitic transformation is performed by adapting Eq. (9) to the specific time step, see Eq. (A.45). The increment of the volume fraction of martensite is calculated as the difference between the current step and the previous step, see Eq. (A.46).

$$f_{\alpha'}^{(n+1)} = 1 - e^{-\xi\left(1-e^{-\zeta\bar{\epsilon}_\gamma^{p(n+1)}}\right)^{4.5}} \tag{A.45}$$

$$\Delta f_{\alpha'}^{(n+1)} = f_{\alpha'}^{(n+1)} - f_{\alpha'}^{(n)} \tag{A.46}$$

A.3. Numerical implementation of the bi-phase material (homogenization)

The implementation of the homogenization procedure consists of two parts. Firstly, the strain and stress increments of the bi-phase material are calculated, the same procedure is followed for both Mori-Tanaka and Self-Consistent approaches. Note that the values of the mechanical fields in the austenite and martensite are taken from the previous resolution of the equations corresponding to the individual phases, see Appendix A.1. Secondly, the instantaneous strain concentration tensors, which depend on the homogenization scheme, are computed and the strain increment for each individual phase is corrected.

The strain increment components of the bi-phase material are calculated as follows:

$$\Delta\boldsymbol{\epsilon}_{TR(vol)}^{(n+1)} = \frac{1}{3}\Delta f_{\alpha'}^{(n+1)}\Delta v\mathbf{1} \tag{A.47}$$

$$\Delta\boldsymbol{\epsilon}_{HM(TR)}^{(n+1)} = \Delta f_{\alpha'}^{(n+1)}\left(\boldsymbol{\epsilon}_{\alpha'}^{(n+1)} - \boldsymbol{\epsilon}_{\gamma}^{(n+1)}\right) \tag{A.48}$$

$$\Delta\boldsymbol{\epsilon}_{HM(noTR)}^{(n+1)} = \Delta\boldsymbol{\epsilon}_{\gamma+\alpha'}^{(n+1)} - \Delta\boldsymbol{\epsilon}_{HM(TR)}^{(n+1)} - \Delta\boldsymbol{\epsilon}_{TR(vol)}^{(n+1)} \tag{A.49}$$

Moreover, the two terms corresponding to the homogenized stress increment are calculated, and the stress increment of the bi-phase material is then computed:

$$\Delta\boldsymbol{\sigma}_{HM(noTR)}^{(n+1)} = \left(1 - f_{\alpha'}^{(n+1)}\right)\Delta\boldsymbol{\sigma}_{\gamma}^{(n+1)} + f_{\alpha'}^{(n+1)}\Delta\boldsymbol{\sigma}_{\alpha'}^{(n+1)} \tag{A.50}$$

$$\Delta\boldsymbol{\sigma}_{HM(TR)}^{(n+1)} = \Delta f_{\alpha'}^{(n+1)}\left(\boldsymbol{\sigma}_{\alpha'}^{(n+1)} - \boldsymbol{\sigma}_{\gamma}^{(n+1)}\right) \tag{A.51}$$

$$\Delta\boldsymbol{\sigma}_{\gamma+\alpha'}^{(n+1)} = \Delta\boldsymbol{\sigma}_{HM(noTR)}^{(n+1)} + \Delta\boldsymbol{\sigma}_{HM(TR)}^{(n+1)} \tag{A.52}$$

Depending on the homogenization scheme, the instantaneous strain concentration tensors are calculated:

- **Mori-Tanaka scheme**. First, the tangent bulk and shear moduli corresponding to the isotropic version of the algorithmic tangent operator of the austenite phase are calculated (see Eq. (A.53)). Subsequently, the tangent Poisson's ratio and the Eshelby's tensor are determined (see Eq. (A.54)). Then, the instantaneous dilute concentration tensor is obtained, from which the instantaneous strain concentration tensor is calculated for each phase (see Eqs. (A.55)–(A.57)). Finally, the homogenized tangent stiffness tensor, which is later used for the computation of the Jacobian tensor A.4, is determined (see Eq. (A.58)).

$$\kappa_{\gamma}^{tan(n+1)} = \frac{1}{3}\boldsymbol{I}_{vol} :: \boldsymbol{L}_{\gamma}^{tan(n+\Lambda)}, \qquad \mu_{\gamma}^{tan(n+1)} = \frac{1}{10}\boldsymbol{I}_{dev} :: \boldsymbol{L}_{\gamma}^{tan(n+\Lambda)} \tag{A.53}$$

$$\nu_{\gamma}^{tan(n+1)} = \frac{3\kappa_{\gamma}^{tan(n+1)} - 2\mu_{\gamma}^{tan(n+1)}}{2\left(3\kappa_{\gamma}^{tan(n+1)} + \mu_{\gamma}^{tan(n+1)}\right)},$$
$$\boldsymbol{S}_{\gamma,spher}^{tan\text{-}iso(n+1)} = \frac{1}{3}\frac{1+\nu_{\gamma}^{tan(n+1)}}{1-\nu_{\gamma}^{tan(n+1)}}\boldsymbol{I}_{vol} + \frac{2}{15}\frac{4-5\nu_{\gamma}^{tan(n+1)}}{1-\nu_{\gamma}^{tan(n+1)}}\boldsymbol{I}_{dev}$$
$$\boldsymbol{A}_{dil(\alpha',\gamma)}^{tan(n+1)} = \left(\boldsymbol{I} + \boldsymbol{S}_{\gamma,spher}^{tan\text{-}iso(n+1)} : \left(\boldsymbol{L}_{\gamma}^{tan(n+\Lambda)}\right)^{-1} : \left(\boldsymbol{L}_{\alpha'}^{tan(n+\Lambda)} - \boldsymbol{L}_{\gamma}^{tan(n+\Lambda)}\right)\right)^{-1} \tag{A.54, A.55}$$

$$\boldsymbol{A}_{\gamma(noTR)}^{tan(n+1)} = \left(\left(1 - f_{\alpha'}^{(n+1)}\right)\boldsymbol{I} + f_{\alpha'}^{(n+1)}\boldsymbol{A}_{dil(\alpha',\gamma)}^{tan(n+1)}\right)^{-1} \tag{A.56}$$

$$\boldsymbol{A}_{\alpha'(noTR)}^{tan(n+1)} = \boldsymbol{A}_{dil(\alpha',\gamma)}^{tan(n+1)} : \left(\left(1 - f_{\alpha'}^{(n+1)}\right)\boldsymbol{I} + f_{\alpha'}^{(n+1)}\boldsymbol{A}_{dil(\alpha',\gamma)}^{tan(n+1)}\right)^{-1} \tag{A.57}$$

$$\boldsymbol{L}_{HM(noTR)}^{tan(n+1)} = (1 - f_{\alpha'}^{(n+1)})\boldsymbol{L}_{\gamma}^{tan(n+\Lambda)} : \boldsymbol{A}_{\gamma(noTR)}^{tan(n+1)} + f_{\alpha'}^{(n+1)}\boldsymbol{L}_{\alpha'}^{tan(n+\Lambda)} : \boldsymbol{A}_{\alpha'(noTR)}^{tan(n+1)} \tag{A.58}$$

- **Self-Consistent scheme**. For the first iteration of the scheme, a trial homogenized tangent stiffness tensor is assumed and used to calculate the tangent bulk and shear moduli corresponding to the isotropic version of the tensor (see Eq. (A.59)). Subsequently, the tangent Poisson's ratio and the Eshelby's tensor are determined (see Eq. (A.60)). Then, the instantaneous strain concentration tensor for each phase is calculated (Eqs. (A.61)–(A.62)). Afterward, the instantaneous homogenized tangent stiffness tensor is computed and updated for the next iteration (see Eq. (A.63)). The set of Eqs. (A.59)–(A.63) is recomputed until the difference between the instantaneous homogenized tangent stiffness tensor calculated in consecutive iterations is lower than a specific tolerance (note that the subscript (k) indicates the step in the iterative scheme).

$$\kappa_{HM(noTR)(k)}^{tan(n+1)} = \frac{1}{3}\boldsymbol{I}_{vol} :: \boldsymbol{L}_{HM(noTR)(k)}^{tan(n+1)},$$
$$\mu_{HM(noTR)(k)}^{tan(n+1)} = \frac{1}{10}\boldsymbol{I}_{dev} :: \boldsymbol{L}_{HM(noTR)(k)}^{tan(n+1)} \tag{A.59}$$

$$\nu_{HM(noTR)(k)}^{tan(n+1)} = \frac{3\kappa_{HM(noTR)(k)}^{tan(n+1)} - 2\mu_{HM(noTR)(k)}^{tan(n+1)}}{2\left(3\kappa_{HM(noTR)(k)}^{tan(n+1)} + \mu_{HM(noTR)(k)}^{tan(n+1)}\right)},$$
$$\boldsymbol{S}_{HM(noTR)(k),spher}^{tan\text{-}iso(n+1)} = \frac{1}{3}\frac{1+\nu_{HM(noTR)(k)}^{tan(n+1)}}{1-\nu_{HM(noTR)(k)}^{tan(n+1)}}\boldsymbol{I}_{vol} + \frac{2}{15}\frac{4-5\nu_{HM(noTR)(k)}^{tan(n+1)}}{1-\nu_{HM(noTR)(k)}^{tan(n+1)}}\boldsymbol{I}_{dev} \tag{A.60}$$

$$\boldsymbol{A}_{\gamma(noTR)(k)}^{tan(n+1)} = \left(\boldsymbol{I} + \boldsymbol{S}_{HM(noTR)(k),spher}^{tan\text{-}iso(n+1)} : \left(\boldsymbol{L}_{HM(noTR)(k)}^{tan(n+1)}\right)^{-1} : \left(\boldsymbol{L}_{\gamma}^{tan(n+\Lambda)} - \boldsymbol{L}_{HM(noTR)(k)}^{tan(n+1)}\right)\right)^{-1} \tag{A.61}$$

$$\boldsymbol{A}_{\alpha'(noTR)(k)}^{tan(n+1)} = \left(\boldsymbol{I} + \boldsymbol{S}_{HM(noTR)(k),spher}^{tan\text{-}iso(n+1)} : \left(\boldsymbol{L}_{HM(noTR)(k)}^{tan(n+1)}\right)^{-1} : \left(\boldsymbol{L}_{\alpha'}^{tan(n+\Lambda)} - \boldsymbol{L}_{HM(noTR)(k)}^{tan(n+1)}\right)\right)^{-1} \tag{A.62}$$

$$\boldsymbol{L}_{HM(noTR)(k+1)}^{tan(n+1)} = (1 - f_{\alpha'}^{(n+1)})\boldsymbol{L}_{\gamma}^{tan(n+\Lambda)} : \boldsymbol{A}_{\gamma(noTR)(k)}^{tan(n+1)} + f_{\alpha'}^{(n+1)}\boldsymbol{L}_{\alpha'}^{tan(n+\Lambda)} : \boldsymbol{A}_{\alpha'(noTR)(k)}^{tan(n+1)} \tag{A.63}$$

Finally, the strain increment in each phase is corrected using the corresponding instantaneous strain concentration tensor. If $f_{\alpha'}^{(n+1)} < 1$, the corrected strain increment for the austenite is calculated with Eq. (A.64); otherwise, $\Delta\boldsymbol{\epsilon}_{\gamma}^{(n+1)} = \boldsymbol{0}$. If $f_{\alpha'}^{(n+1)} > 0$, the corrected strain increment for the martensite is calculated with Eq. (A.65); otherwise, $\Delta\boldsymbol{\epsilon}_{\alpha'}^{(n+1)} = \boldsymbol{0}$.

$$\Delta\boldsymbol{\epsilon}_{\gamma}^{(n+1)} = \boldsymbol{A}_{\gamma(noTR)}^{tan(n+1)} : \Delta\boldsymbol{\epsilon}_{HM(noTR)}^{(n+1)} \tag{A.64}$$

$$\Delta\boldsymbol{\epsilon}_{\alpha'}^{(n+1)} = \boldsymbol{A}_{\alpha'(noTR)}^{tan(n+1)} : \Delta\boldsymbol{\epsilon}_{HM(noTR)}^{(n+1)} \tag{A.65}$$

A.4. Numerical implementation of the consistent Jacobian tensor

The consistent Jacobian tensor is defined as:

$$\frac{1}{J_{\gamma+\alpha'}^{(n+1)}}\frac{\partial\Delta\boldsymbol{\tau}_{\gamma+\alpha'}^{(n+1)}}{\partial\Delta\boldsymbol{\epsilon}_{\gamma+\alpha'}^{(n+1)}} = \boldsymbol{\sigma}_{\gamma+\alpha'}^{(n+1)} \otimes \boldsymbol{1} + \boldsymbol{L}_{\gamma+\alpha'}^{tan(n+1)} \tag{A.66}$$

which refers to the objective increment of the fields at the integration point level $(\gamma + \alpha')$ for the current time step $(n + 1)$, where $\boldsymbol{\tau}$ is the Kirchhoff stress tensor, J is the determinant of the deformation gradient tensor, and $\boldsymbol{L}_{\gamma+\alpha'}^{tan(n+1)}$ is the so-called material tangent modulus which is given by $\Delta\boldsymbol{\sigma}_{\gamma+\alpha'}^{(n+1)} = \boldsymbol{L}_{\gamma+\alpha'}^{tan(n+1)} : \Delta\boldsymbol{\epsilon}_{\gamma+\alpha'}^{(n+1)}$. In order to derive the expression of the material tangent modulus, the relationship between the stress increment and the strain increment in the bi-phase material must be established.

For that purpose, the stress increment in the bi-phase material is expressed as follows (see Eqs. (12) and (14)):

$$\Delta\boldsymbol{\sigma}_{\gamma+\alpha'}^{(n+1)} = \Delta\boldsymbol{\sigma}_{HM}^{(n+1)} = \Delta\boldsymbol{\sigma}_{HM(noTR)}^{(n+1)} + \Delta\boldsymbol{\sigma}_{HM(TR)}^{(n+1)} \tag{A.67}$$

with (see Eq. (16)):

$$\Delta\boldsymbol{\sigma}_{HM(noTR)}^{(n+1)} = \boldsymbol{L}_{HM(noTR)}^{tan(n+1)} : \Delta\boldsymbol{\epsilon}_{HM(noTR)}^{(n+1)} \tag{A.68}$$

$$\Delta\boldsymbol{\sigma}_{HM(TR)}^{(n+1)} = \left(\boldsymbol{\sigma}_{\alpha'}^{(n+1)} - \boldsymbol{\sigma}_{\gamma}^{(n+1)}\right)\left(\boldsymbol{\phi}^{(n+1)} : \Delta\boldsymbol{\epsilon}_{HM(noTR)}^{(n+1)}\right) \tag{A.69}$$

where the term $\Delta\boldsymbol{\sigma}_{HM(noTR)}^{(n+1)}$ is expressed as a function of $\Delta\boldsymbol{\epsilon}_{HM(noTR)}^{(n+1)}$ using the tensor $\boldsymbol{L}_{HM(noTR)}^{tan(n+1)}$ (see Eq. (26)), and the term $\Delta\boldsymbol{\sigma}_{HM(TR)}^{(n+1)}$ is also expressed as a function of $\Delta\boldsymbol{\epsilon}_{HM(noTR)}^{(n+1)}$ using the relationship $\Delta f_{\alpha'}^{(n+1)} = \boldsymbol{\phi}^{(n+1)} : \Delta\boldsymbol{\epsilon}_{HM(noTR)}^{(n+1)}$. The consistent second-order tensor $\boldsymbol{\phi}^{(n+1)}$ is obtained as follows:

$$\boldsymbol{\phi}^{(n+1)} = \left(\frac{d\left(\Delta f_{\alpha'}\right)}{d\left(\Delta\boldsymbol{\epsilon}_{HM(noTR)}\right)}\right)^{(n+1)} = \left(\phi_1\,\boldsymbol{\phi}_2 : \boldsymbol{\phi}_3 : \boldsymbol{\phi}_4\right)^{(n+1)} \tag{A.70}$$

with:

$$\phi_1^{(n+1)} = \left(\frac{d\left(\Delta f_{\alpha'}\right)}{d\left(\Delta\bar{\epsilon}_{\gamma}^{p}\right)}\right)^{(n+1)} = 4.5\xi\zeta[1 - e^{-\zeta\bar{\epsilon}_{\gamma}^{p(n+1)}}]^{3.5}e^{-\zeta\bar{\epsilon}_{\gamma}^{p(n+1)}}(1 - f_{\alpha'}^{(n+1)}) \tag{A.71}$$

$$\boldsymbol{\phi}_2^{(n+1)} = \left(\frac{d\left(\Delta\bar{\epsilon}_{\gamma}^{p}\right)}{d\left(\Delta\boldsymbol{\epsilon}_{\gamma}^{p}\right)}\right)^{(n+1)} = \frac{2}{3}\frac{\Delta\boldsymbol{\epsilon}_{\gamma}^{p(n+1)}}{\Delta\bar{\epsilon}_{\gamma}^{p(n+1)}} \tag{A.72}$$

$$\boldsymbol{\phi}_3^{(n+1)} = \left(\frac{d\left(\Delta\boldsymbol{\epsilon}_{\gamma}^{p}\right)}{d\left(\Delta\boldsymbol{\epsilon}_{\gamma}\right)}\right)^{(n+1)} = \left[\boldsymbol{I} - \left(\boldsymbol{L}_{\gamma}^{e}\right)^{-1} : \boldsymbol{L}_{\gamma}^{tan(n+\Lambda)}\right] \tag{A.73}$$

$$\boldsymbol{\phi}_4^{(n+1)} = \left(\frac{d\left(\Delta\boldsymbol{\epsilon}_{\gamma}\right)}{d\left(\Delta\boldsymbol{\epsilon}_{HM(noTR)}\right)}\right)^{(n+1)} = \boldsymbol{A}_{\gamma(noTR)}^{tan(n+1)} \tag{A.74}$$

Thus, inserting Eqs. (A.68) and (A.69) into Eq. (A.67) leads to:

$$\Delta\boldsymbol{\sigma}_{\gamma+\alpha'}^{(n+1)} = \left(\boldsymbol{L}_{HM(noTR)}^{tan(n+1)} + \left(\boldsymbol{\sigma}_{\alpha'}^{(n+1)} - \boldsymbol{\sigma}_{\gamma}^{(n+1)}\right) \otimes \boldsymbol{\phi}^{(n+1)}\right) : \Delta\boldsymbol{\epsilon}_{HM(noTR)}^{(n+1)} \tag{A.75}$$

where a relationship between $\Delta\boldsymbol{\epsilon}_{HM(noTR)}^{(n+1)}$ and $\Delta\boldsymbol{\epsilon}_{\gamma+\alpha'}^{(n+1)}$ is still required. For this purpose, the relationship $\Delta f_{\alpha'}^{(n+1)} = \boldsymbol{\phi}^{(n+1)} : \Delta\boldsymbol{\epsilon}_{HM(noTR)}^{(n+1)}$ is also used in the definition of $\Delta\boldsymbol{\epsilon}_{HM(TR)}^{(n+1)}$ and $\Delta\boldsymbol{\epsilon}_{TR(vol)}^{(n+1)}$ as follows (see Eqs. $(15)_2$ and (11), respectively):

$$\Delta\boldsymbol{\epsilon}_{HM(TR)}^{(n+1)} = \left(\boldsymbol{\epsilon}_{\alpha'}^{(n+1)} - \boldsymbol{\epsilon}_{\gamma}^{(n+1)}\right)\left(\boldsymbol{\phi}^{(n+1)} : \Delta\boldsymbol{\epsilon}_{HM(noTR)}^{(n+1)}\right) \tag{A.76}$$

$$\Delta\boldsymbol{\epsilon}_{TR(vol)}^{(n+1)} = \frac{1}{3}\Delta v\boldsymbol{1}\left(\boldsymbol{\phi}^{(n+1)} : \Delta\boldsymbol{\epsilon}_{HM(noTR)}^{(n+1)}\right) \tag{A.77}$$

so that the total strain increment in the bi-phase material (see Eqs. (10) and (13)) is expressed as:

$$\Delta\boldsymbol{\epsilon}^{(n+1)}_{\gamma+\alpha'} = \Delta\boldsymbol{\epsilon}^{(n+1)}_{HM(noTR)} + \Delta\boldsymbol{\epsilon}^{(n+1)}_{HM(TR)} + \Delta\boldsymbol{\epsilon}^{(n+1)}_{TR(vol)} = \left(\boldsymbol{I} + \left(\left(\boldsymbol{\epsilon}^{(n+1)}_{\alpha'} - \boldsymbol{\epsilon}^{(n+1)}_{\gamma}\right) + \frac{1}{3}\Delta v\mathbf{1}\right) \otimes \boldsymbol{\phi}^{(n+1)}\right) : \Delta\boldsymbol{\epsilon}^{(n+1)}_{HM(noTR)} \tag{A.78}$$

which, inserted into Eq. (A.75), leads to $\Delta\boldsymbol{\sigma}^{(n+1)}_{\gamma+\alpha'} = \boldsymbol{L}^{tan(n+1)}_{\gamma+\alpha'} : \Delta\boldsymbol{\epsilon}^{(n+1)}_{\gamma+\alpha'}$, where the instantaneous material tangent modulus is given by:

$$\boldsymbol{L}^{tan(n+1)}_{\gamma+\alpha'} = \left(\boldsymbol{L}^{tan(n+1)}_{HM(noTR)} + \left(\boldsymbol{\sigma}^{(n+1)}_{\alpha'} - \boldsymbol{\sigma}^{(n+1)}_{\gamma}\right) \otimes \boldsymbol{\phi}^{(n+1)}\right) : \left(\boldsymbol{I} + \left(\left(\boldsymbol{\epsilon}^{(n+1)}_{\alpha'} - \boldsymbol{\epsilon}^{(n+1)}_{\gamma}\right) + \frac{1}{3}\Delta v\mathbf{1}\right) \otimes \boldsymbol{\phi}^{(n+1)}\right)^{-1} \tag{A.79}$$

Note that the material tangent modulus (Eq. (A.79)) and the consistent Jacobian tensor (Eq. (A.66)) may be nonsymmetric, so the unsymmetric equation solution capability in ABAQUS/Standard should be invoked (see Section 6.1.1 in ABAQUS (2016)).

Appendix B. Unit-cell calculations: the effect of temperature

Fig. B.21 shows the evolution of the normalized macroscopic effective stress $\bar{\Sigma}/\sigma^{y0}_{\gamma}$ with the macroscopic effective strain $\bar{\varepsilon}$ for a simulation with the FCC-symmetric spatial distribution of inclusions with the same size and particles intersecting the boundaries, Fig. 4(b). The material parameters correspond to AISI 304L. The results are compared with the predictions of the Mori-Tanaka and Self-Consistent homogenization schemes. The martensite volume fraction is 45%, i.e., the simulations do not take into account the martensitic transformation. The difference with the calculations included in Fig. 6(b) is that the material temperature is lower: 4 K (instead of 77 K). The comparison of Figs. 6(b) and B.21 shows that with decreasing temperature, the $\bar{\Sigma}/\sigma^{y0}_{\gamma} - \bar{\varepsilon}$ curves of both the individual phases and the bi-phase material shift upward (due to the temperature sensitivity of the flow strength of both austenite and martensite, see Table 2). Notice that the Self-Consistent model predictions find excellent agreement with the results obtained with the explicit representation of the martensite inclusions for the bi-phase material, while underestimating the strain in the martensite and overestimating the strain of the austenite, just like at the higher temperature of $T = 77$ K. On the other hand, note that the Mori-Tanaka model predictions are less accurate for this low temperature as compared to 77 K: the effective stress in the bi-phase material is increasingly underestimated, and the differences in the strain of the phases are more important.

Appendix C. Unit-cell calculations: the effect of material parameters

Fig. C.22 shows the evolution of the normalized macroscopic effective stress $\bar{\Sigma}/\sigma^{y0}_{\gamma}$ with the macroscopic effective strain $\bar{\varepsilon}$ for a simulation with the FCC-symmetric spatial distribution of inclusions with the same size and particles intersecting the boundaries, Fig. 4(b). The results are compared with the predictions of Mori-Tanaka and Self-Consistent homogenization schemes. The martensite volume fraction is constant 45%, i.e., the simulations do not take into account the martensitic transformation. The difference with the calculations included in Fig. 6(b) is that the material parameters correspond to stainless steel 316LN, see Table 2. The simulations with the homogenization models yield predictions that are much closer to the results obtained with the explicit representation of the martensite inclusions than in the case of steel 304L (compare Figs. 6(b) and C.22). Most likely, it is due to the fact that the mechanical behavior of austenite and martensite is more similar in the case of 316LN. Note that for a macroscopic effective strain of $\bar{\varepsilon} = 0.4$, the value of the macroscopic effective stress in the martensite is (only) 9% greater than in the austenite, while in the case of the 304L steel, the difference is 98%.

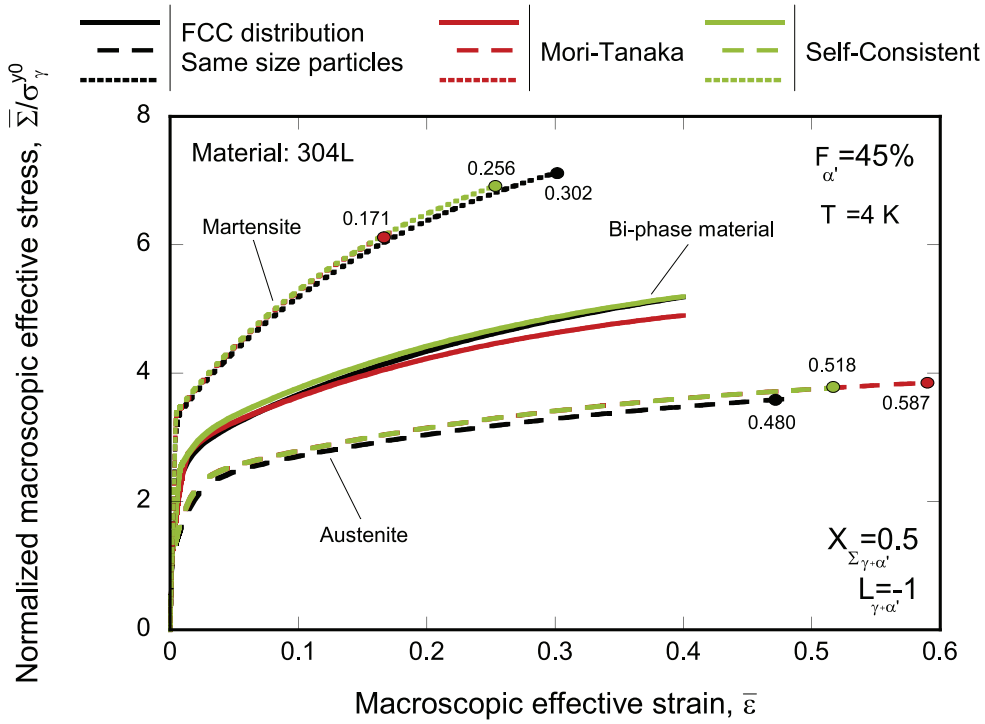

Fig. B.21. Unit-cell finite element simulations. Monotonic loading. Material 304L, temperature $T = 4$ K, and volume fraction of martensite $F_{\alpha'} = 45\%$. Comparison of Mori-Tanaka and Self-Consistent homogenization schemes with calculations corresponding to the FCC-symmetric spatial distribution of inclusions with the same size and particles intersecting the boundaries, Fig. 4(b). Evolution of the normalized macroscopic effective stress $\bar{\Sigma}/\sigma^{y0}_{\gamma}$ with the macroscopic effective strain $\bar{\varepsilon}$. Results corresponding to the bi-phase material, the austenite phase, and the martensite phase for stress triaxiality $X_{\Sigma_{\gamma+\alpha'}} = 0.5$ and Lode parameter $L_{\gamma+\alpha'} = -1$. The colored markers indicate the maximum value of the macroscopic effective strain for the individual phases for a macroscopic effective strain of the bi-phase material of $\bar{\varepsilon}_{\gamma+\alpha'} = 0.4$. (For interpretation of the references to color in this figure legend, the reader is referred to the web version of this article.)

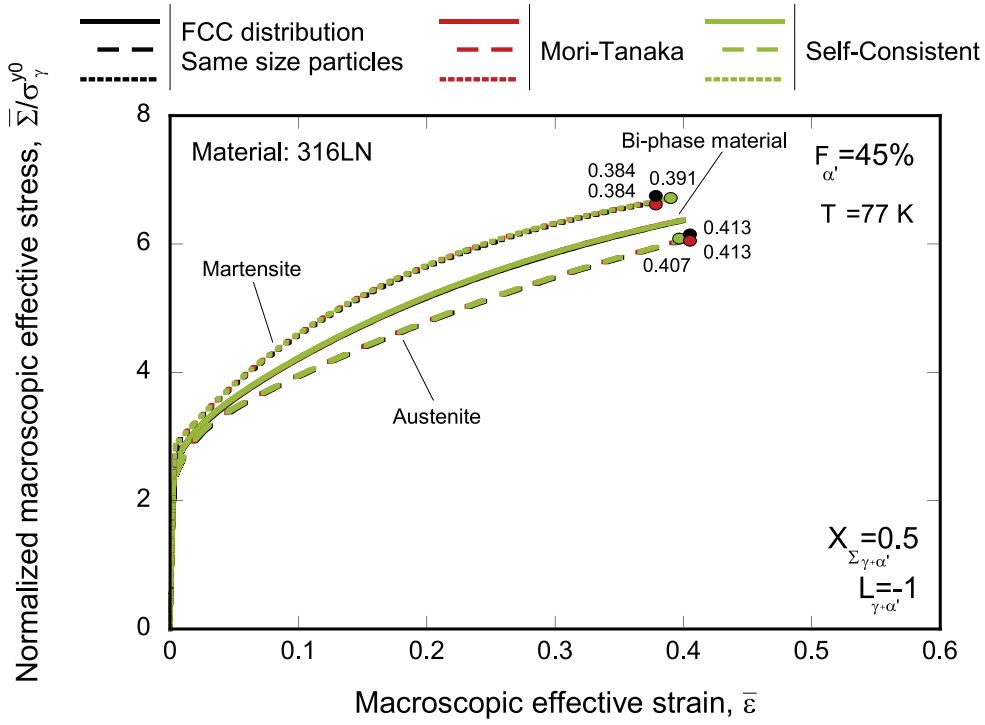

Fig. C.22. Unit-cell finite element simulations. Monotonic loading. Material 316LN, temperature $T = 77$ K, and volume fraction of martensite $F_{\alpha'} = 45\%$. Comparison of Mori-Tanaka and Self-Consistent homogenization schemes with calculations corresponding to the FCC-symmetric spatial distribution of inclusions with the same size and particles intersecting the boundaries, Fig. 4(b). Evolution of the normalized macroscopic effective stress $\bar{\Sigma}/\sigma_\gamma^{y0}$ with the macroscopic effective strain $\bar{\varepsilon}$. Results corresponding to the bi-phase material, the austenite phase, and the martensite phase for stress triaxiality $X_{\Sigma_{\gamma+\alpha'}} = 0.5$ and Lode parameter $L_{\gamma+\alpha'} = -1$. The colored markers indicate the maximum value of the macroscopic effective strain for the individual phases for a macroscopic effective strain of the bi-phase material of $\bar{\varepsilon}_{\gamma+\alpha'} = 0.4$. (For interpretation of the references to color in this figure legend, the reader is referred to the web version of this article.)

Appendix D. Supplementary data

The UMAT subroutine coded to implement in the finite element code ABAQUS the developed homogenized constitutive model can be found online at https://doi.org/10.21950/H27ZVN.

References

ABAQUS, 2016. Abaqus analysis user's manual. DSC simulia.

Angel, T., 1954. Formation of martensite in austenitic stainless steels. J. Iron Steel Inst. 177, 165–174.

Armstrong, P.J., Frederick, C., et al., 1966. A Mathematical Representation of the Multiaxial Bauschinger Effect. Vol. 731. Berkeley Nuclear Laboratories Berkeley, CA.

Barabash, V., The ITER International Team, Peacock, A., Fabritsiev, S., Kalinin, G., Zinkle, S., Rowcliffe, A., Rensman, J.-W., Tavassoli, A., Marmy, P., et al., 2007. Materials challenges for ITER – Current status and future activities. J. Nucl. Mater. 367, 21–32.

Benveniste, Y., 1987. A new approach to the application of Mori-Tanaka's theory in composite materials. Mech. Mater. 6 (2), 147–157.

Bertinelli, F., Fudanoki, F., Komori, T., Peiro, G., Rossi, L., 2006. Production of austenitic steel for the LHC superconducting dipole magnets. IEEE Trans. Appl. Supercond. 16 (2), 1773–1776.

Böhm, H.J., 1998. A short introduction to basic aspects of continuum micromechanics. (expanded and modified version of the CDL–FMD report 3–1998, version: 2021).

Bordini, B., Bottura, L., Devred, A., Fiscarelli, L., Karppinen, M., de Rijk, G., Rossi, L., Savary, F., Willering, G., 2019. Nb3Sn 11 T dipole for the High Luminosity LHC (CERN). In: Nb3Sn Accelerator Magnets: Designs, Technologies and Performance. Springer, pp. 223–258.

Bornert, M., Bretheau, T., Gilormini, P., 2001a. Homogénéisation En Mécanique Des Matériaux, Tome 1: Matériaux Aléatoires ÉLastiques Et Milieux Périodiques. Hermes Science.

Bornert, M., Bretheau, T., Gilormini, P., 2001b. Homogénéisation En Mécanique Des Matériaux, Tome 2: Comportements Non Linéaires Et Problèmes Ouverts. Hermes Science.

Chaboche, J.-L., Kanouté, P., 2003. Sur les approximations "isotrope" et "anisotrope" de l'opérateur tangent pour les méthodes tangentes incrémentale et affine. C. R. Méc. 331 (12), 857–864.

Chaboche, J., Van, K.D., Cordier, G., 1979. Modelization of the Strain Memory Effect on the Cyclic Hardening of 316 Stainless Steel. IASMiRT.

Chatzigeorgiou, G., Charalambakis, N., Chemisky, Y., Meraghni, F., 2018. Thermomechanical Behavior of Dissipative Composite Materials. Elsevier.

Cherkaoui, M., Berveiller, M., Sabar, H., 1998. Micromechanical modeling of martensitic transformation induced plasticity (TRIP) in austenitic single crystals. Int. J. Plast. 14 (7), 597–626.

Christman, T., Needleman, A., Suresh, S., 1989. An experimental and numerical study of deformation in metal-ceramic composites. Acta Metall. 37 (11), 3029–3050.

Dakshinamurthy, M., Kowalczyk-Gajewska, K., Vadillo, G., 2021. Influence of crystallographic orientation on the void growth at the grain boundaries in bi-crystals. Int. J. Solids Struct. 212, 61–79.

De, A.K., Murdock, D.C., Mataya, M.C., Speer, J.G., Matlock, D.K., 2004. Quantitative measurement of deformation-induced martensite in 304 stainless steel by X-ray diffraction. Scr. Mater. 50 (12), 1445–1449.

Devred, A., Backbier, I., Bessette, D., Bevillard, G., Gardner, M., Jong, C., Lillaz, F., Mitchell, N., Romano, G., Vostner, A., 2014. Challenges and status of ITER conductor production. Supercond. Sci. Technol. 27 (4).

Ding, H., Wu, Y., Lu, Q., Wang, Y., Zheng, J., Xu, P., 2019. A modified stress-strain relation for austenitic stainless steels at cryogenic temperatures. Cryogenics 101, 89–100.

Doghri, I., 2000. Mechanics of Deformable Solids: Linear and Nonlinear, Analytical and Computational Aspects. Springer.

Doghri, I., Ouaar, A., 2003. Homogenization of two-phase elasto-plastic composite materials and structures: Study of tangent operators, cyclic plasticity and numerical algorithms. Int. J. Solids Struct. 40 (7), 1681–1712.

Eshelby, J.D., 1957. The determination of the elastic field of an ellipsoidal inclusion, and related problems. Proc. R. Soc. Lond. Ser. A Math. Phys. Sci. 241 (1226), 376–396.

Fernández-Pisón, P., Rodríguez-Martínez, J.A., García-Tabarés, E., Avilés-Santillana, I., Sgobba, S., 2021. Flow and fracture of austenitic stainless steels at cryogenic temperatures. Eng. Fract. Mech. 258 (108042).

Garion, C., Skoczeń, B., 2002. Modeling of plastic strain-induced martensitic transformation for cryogenic applications. J. Appl. Mech. 69 (6), 755–762.

Garion, C., Skoczeń, B., Sgobba, S., 2006. Constitutive modelling and identification of parameters of the plastic strain-induced martensitic transformation in 316L stainless steel at cryogenic temperatures. Int. J. Plast. 22 (7), 1234–1264.

Giompliakis, A., 2014. Three Dimensional Unit Cell Modeling of Multiphase Steels. University of Thessaly, Greece.

Hill, R., 1965a. Continuum micro-mechanics of elastoplastic polycrystals. J. Mech. Phys. Solids 13 (2), 89–101.
Hill, R., 1965b. A self-consistent mechanics of composite materials. J. Mech. Phys. Solids 13 (4), 213–222.
Homayounfard, M., Ganjiani, M., 2022. A large deformation constitutive model for plastic strain-induced phase transformation of stainless steels at cryogenic temperatures. Int. J. Plast..
Hosseini, E., Holdsworth, S., Kühn, I., Mazza, E., 2015. Temperature dependent representation for chaboche kinematic hardening model. Mater. High Temp. 32 (4), 404–412.
Hosseini, N., Nieto-Fuentes, J.C., Dakshinamurthy, M., Rodríguez-Martínez, J.A., Vadillo, G., 2022. The effect of material orientation on void growth. Int. J. Plast. 148, 103149.
Hosseini, N., Rodríguez-Martínez, J.A., 2021. A simple and computationally efficient stress integration scheme based on numerical approximation of the yield function gradients: Application to advanced yield criteria. Finite Elem. Anal. Des. 192 (103538).
ISO-6892-4, 2015. Metallic Materials-Tensile Testing-Part 4: Method of Test in Liquid Helium. International Organization for Standardization.
Kazemi, S.S., Homayounfard, M., Ganjiani, M., Soltani, N., 2019. Numerical and experimental analysis of damage evolution and martensitic transformation in AISI 304 austenitic stainless steel at cryogenic temperature. Int. J. Appl. Mech. 11 (02).
Kothari, M., Niu, S., Srivastava, V., 2019. A thermo-mechanically coupled finite strain model for phase-transitioning austenitic steels in ambient to cryogenic temperature range. J. Mech. Phys. Solids 133.
Kula, E., Azrin, M., 1978. Thermomechanical processing of ferrous alloys. In: Advances in Deformation Processing. Plenum Press, NY, pp. 245–300.
Lee, K.J., Chun, M.S., Kim, M.H., Lee, J.M., 2009. A new constitutive model of austenitic stainless steel for cryogenic applications. Comput. Mater. Sci. 46 (4), 1152–1162.
Lemaitre, J., Chaboche, J.-L., 1994. Mechanics of Solid Materials. Cambridge University Press.
Luo, H., Hooshmand-Ahoor, Z., Danas, K., Diani, J., 2023. Numerical estimation via remeshing and analytical modeling of nonlinear elastic composites comprising a large volume fraction of randomly distributed spherical particles or voids. Eur. J. Mech. A Solids 101.
Mangonon, P., Thomas, G., 1970. The martensite phases in 304 stainless steel. Metallur. Trans. 1.
Mori, T., Tanaka, K., 1973. Average stress in matrix and average elastic energy of materials with misfitting inclusions. Acta Metall. 21 (5), 571–574.
Msolli, S., Martiny, M., Cardoso, M.C., Moreira, L.P., Mercier, S., Molinari, A., 2016. Numerical modeling of the deformation of AISI 304L using a tangent additive Mori-Tanaka homogenization scheme: Application to sheet metal forming. J. Mater Process. Technol. 235, 187–205.
Needleman, A., 1972. Void growth in an elastic-plastic medium. J. Appl. Mech. 39 (4), 964–970.
Needleman, A., Borders, T., Brinson, L., Flores, V., Schadler, L., 2010. Effect of an interphase region on debonding of a CNT reinforced polymer composite. Compos. Sci. Technol. 70 (15), 2207–2215.
Nguyen, N., Waas, A.M., 2016. Nonlinear, finite deformation, finite element analysis. Z. Angew. Math. Phys. 67 (3), 1–24.
Olson, G., Cohen, M., 1975. Kinetics of strain-induced martensitic nucleation. Metall. Trans. A 6 (791).
Ortwein, R., Skoczeń, B., Tock, J.P., 2014. Micromechanics based constitutive modeling of martensitic transformation in metastable materials subjected to torsion at cryogenic temperatures. Int. J. Plast. 59, 152–179.
Papatriantafillou, I., 2005. TRIP Steels: Constitutive Modeling and Computational Issues (Ph.D. thesis). Thessaly University, Greece.
Papatriantafillou, I., Agoras, M., Aravas, N., G, H., 2006. Constitutive modeling and finite element methods for TRIP steels. Comput. Methods Appl. Mech. Engrg. 195, 5094–5114.
Perdahcıoğlu, E.S., Geijselaers, H.J., 2011a. Constitutive modeling of two phase materials using the mean field method for homogenization. Int. J. Mater. Form. 4 (2), 93–102.
Perdahcıoğlu, E.S., Geijselaers, H.J., 2011b. Prediction of the mechanical behaviour of TRIP steel. In: 10th International Conference on Technology of Plasticity. ICTP 2011, pp. 1–4.
Pierard, O., Doghri, I., 2006. Study of various estimates of the macroscopic tangent operator in the incremental homogenization of elastoplastic composites. Int. J. Multiscale Comput. Eng. 4 (4).
Pierard, O., LLorca, J., Segurado, J., Doghri, I., 2007. Micromechanics of particle-reinforced elasto-viscoplastic composites: finite element simulations versus affine homogenization. Int. J. Plast. 23 (6), 1041–1060.
Ponte-Castañeda, P., 1996. Exact second-order estimates for the effective mechanical properties of nonlinear composite materials. J. Mech. Phys. Solids 44 (6), 827–862.
Rodríguez-Martínez, J.A., Pesci, R., Rusinek, A., 2011. Experimental study on the martensitic transformation in AISI 304 steel sheets subjected to tension under wide ranges of strain rate at room temperature. Mater. Sci. Eng. A 528 (18), 5974–5982.
Safaei, M., 2013. Constitutive Modelling of Anisotropic Sheet Metals Based on a Non-Associated Flow Rule (Ph.D. thesis). Ghent University, Belgium.
Schmidt, R., Skoczeń, B., Bielski, J., Schmidt, E., 2022. New double surface constitutive model of intermittent plastic flow applied to near 0 K adiabatic shear bands. Mech. Mater. 175.
Seetharaman, V., 1984. Deformation and martensitic transformation. Bull. Mater. Sci. 6 (4), 703–716.
Sgobba, S., 2006. Materials for High Vacuum Technology, an Overview. Technical Report, CERN, Switzerland.
Shen, Y.L., Needleman, A., Suresh, S., 1994. Coefficients of thermal expansion of metal-matrix composites for electronic packaging. Metall. Mater. Trans. A 25, 839–850.
Sitko, M., Skoczeń, B., Wróblewski, A., 2010. FCC–BCC phase transformation in rectangular beams subjected to plastic straining at cryogenic temperatures. Int. J. Mech. Sci. 52 (7), 993–1007.
Sørensen, N.J., Suresh, S., Tvergaard, V., Needleman, A., 1995. Effects of reinforcement orientation on the tensile response of metal-matrix composites. Mater. Sci. Eng. A 197 (1), 1–10.
Srivastava, A., Ghassemi-Armaki, H., Sung, H., Chen, P., Kumar, S., Bower, A.F., 2015. Micromechanics of plastic deformation and phase transformation in a three-phase TRIP-assisted advanced high strength steel: Experiments and modeling. J. Mech. Phys. Solids 78, 46–69.
Stringfellow, R.G., Parks, D.M., Olson, G.B., 1992. A constitutive model for transformation plasticity accompanying strain-induced martensitic transformations in metastable austenitic steels. Acta Metall. Mater. 40 (7), 1703–1716.
Tabin, J., Skoczen, B., Bielski, J., 2016. Strain localization during discontinuous plastic flow at extremely low temperatures. Int. J. Solids Struct. 97, 593–612.
Tabin, J., Skoczen, B., Bielski, J., 2019. Discontinuous plastic flow coupled with strain induced FCC–BCC phase transformation at extremely low temperatures. Mech. Mater. 129, 23–40.
Tomita, Y., Iwamoto, T., 1995. Constitutive modeling of TRIP steel and its application to the improvement of mechanical properties. Int. J. Mech. Sci. 37 (12), 1295–1305.
Torquato, S., 2002. Random Heterogeneous Materials: Microstructure and Macroscopic Properties. Springer.
Vadillo, G., Reboul, J., Fernández-Sáez, J., 2016. A modified Gurson model to account for the influence of the Lode parameter at high triaxialities. Eur. J. Mech. A Solids 56, 31–44.
Vishnu, A.R., Vadillo, G., Rodríguez-Martínez, J.A., 2023. Void growth in ductile materials with realistic porous microstructures. Int. J. Plast. 103655.
Zaera, R., Fernández-Sáez, J., 2006. An implicit consistent algorithm for the integration of thermoviscoplastic constitutive equations in adiabatic conditions and finite deformations. Int. J. Solids Struct. 43 (6), 1594–1612.
Zaera, R., Rodríguez-Martínez, J.A., Casado, A., Fernandez-Saez, J., Rusinek, A., Pesci, R., 2012. A constitutive model for analyzing martensite formation in austenitic steels deforming at high strain rates. Int. J. Plast. 29, 77–101.